

**COMPUTATIONAL STUDY OF 3D TURBULENT AIR FLOW
IN A HELICAL ROCKET PUMP INDUCER.**

by
Thierry Le Fur

Thesis submitted to the Faculty of the
Virginia Polytechnic Institute and State University
in partial fulfillment of the requirements for the degree of
Master of Science
in
Mechanical Engineering

APPROVED:

Dr. John Moore, Chairman

Dr. Hal L. Moses

Dr. Adorjan G. Szeless

December, 1989
Blacksburg, Virginia

**COMPUTATIONAL STUDY OF 3D TURBULENT AIR FLOW
IN A HELICAL ROCKET PUMP INDUCER.**

by

Thierry Le Fur

Dr. John Moore, Chairman

Mechanical Engineering

(ABSTRACT)

A computational study of the air flow in a helical rocket pump inducer has been performed using a 3-D elliptic flow procedure including viscous effects. The inlet flow is considered turbulent and fully developed.

The geometric definition of the inducer blade shape and the calculation grid are first presented, followed by a discussion of the flow calculation results displayed in various new graphical representations.

The general characteristics expected from previous experimental and analytical work appear in the simulation and were quantitatively studied. The tip leakage flow observed has velocities of the order of the blade tip speed and is partially convected across the entire passage. The important boundary layer development on the blade pressure side and suction side creates radial outward flows, whereas a radial inward motion develops in the core region, with velocities of same order, and from shroud to hub. Secondary and tip leakage flows combine to give a region of high flow losses and blockage near the shroud wall, and the secondary flow pattern is nearly fully developed by the inducer exit.

Original details were also resolved in the flow calculation. A circumferential vortex develops near the shroud, immediately upstream of the suction side of the swept-back leading edge. A simplified air-LH₂ analogy permitted the prediction of cavitation inception in the liquid hydrogen pump, and the results obtained correspond qualitatively well with water flow visualizations.

The accordance of the model with available air test data at the inlet and exit of the inducer is generally very good, with the total pressure losses in excellent agreement.

Acknowledgements

I wish to express here my gratitude to my family and to all those who assisted me during my stay in Blacksburg and contributed to the achievement of this thesis.

First, to Dr. John Moore and his wife. Their qualification, pedagogical qualities and enthusiasm in work were particularly appreciated. Their son should also not be forgotten here. Thanks to Dr. Hal L. Moses for his always valuable remarks and help, and to Dr. Adorjan Szeless who was also part of my advisory committee.

I am very grateful to the "Société Européenne de Propulsion (SEP)" for its support of this project, and especially to without whom I would not have been able to undertake this education in the United States.

Finally, thousands of thanks to all my friends who contributed to make these past 15 months an unforgettable experience.

"le ciel est bleu...", and "chocolate mousse", and (my Mustang dream), the "Béruriers Noirs", and all the others who shared some time with me. Your eyes and laughs will never be altered by the years...

Table of Contents

1.0 INTRODUCTION	1
2.0 LITERATURE REVIEW.	5
2.1 Cavitation in rocket pump inducers.	5
2.2 Experimental and analytical investigations in noncavitating conditions.	11
2.3 Previous computational studies.	24
2.4 The Moore elliptic flow program (MEFP).	29
3.0 SCOPE AND OBJECTIVES OF THIS RESEARCH.	32
4.0 GENERATION OF A 3-D FINITE DIFFERENCE GRID FOR THE HELICAL INDUCER.	37
4.1 Definition of the blade.	37
4.1.1 Cylindrical coordinate system used and data provided.	37
4.1.2 Generation of a finite difference grid over the reference blade.	40
4.1.2.1 Some complementary choices.	40
4.1.2.2 Definition of the grid in (r, θ, z') coordinate system.	45
4.1.2.3 Final blade grid definition.	46
4.2 Introduction to GEOMI: a tool to manipulate grids.	49
4.3 Completion of the Basic Blade Grid.	51
4.3.1 The tip gap definition.	51
4.3.2 The tangential repeating boundaries definition.	51
4.3.3 The axial boundaries definition.	51
4.3.3.1 Upstream conditions: the spinner definition.	52

4.3.3.2	Downstream conditions: the hub definition.	53
4.3.4	The final BASIC GRID.	56
4.4	Preliminary two-dimensional calculations.	59
4.4.1	The blade-to-blade calculation.	59
4.4.2	The meridional calculation.	65
4.4.3	Choice of the 3-D CALCULATION GRID.	70
5.0	RESULTS OF THE 3-D FLOW CALCULATION.	73
5.1	3-D Flow Calculation Details.	73
5.2	Thermodynamic Analysis of the Flow.	74
5.2.1	Euler work.	74
5.2.2	Losses and efficiency.	75
5.3	Blade-to-Blade and Meridional Analysis.	78
5.3.1	Velocity distribution.	78
5.3.2	Pressure distributions.	85
5.4	Quasi-cross-sectional analysis of the secondary flows.	91
5.4.1	Display of the secondary flows in quasi-cross-sectional planes.	91
5.4.1.1	Definition of the iso- θ sections.	91
5.4.1.2	Definition of the secondary velocities.	92
5.4.2	Static pressure distributions.	94
5.4.3	Secondary velocity and rotary stagnation pressure loss distributions.	98
5.4.3.1	Upstream of the leading edge.	98
5.4.3.2	Tip leakage flow.	98
5.4.3.3	Secondary flow in the boundary layers.	105
5.4.3.4	Other 3-D secondary flow effects.	106
5.4.3.5	Evolution of rotary stagnation pressure losses.	106
5.4.4	Streamwise evolution of the radial secondary velocity at mid-height.	110
5.5	Comparison of the 3-D flow calculation with available air test data.	113
5.5.1	Inlet station.	114
5.5.2	Exit station.	115
5.6	Influence of exit static pressure on work done.	116
5.6.1	Velocities investigated.	116
5.6.2	Loss and work analysis.	117
5.6.3	Summary.	118
5.7	Loss analysis and comparison with other studies.	132

6.0 Conclusions.	135
Bibliography	137
Appendix A. MEFP Format Specifications.	142
Appendix B. 2-D Calculation Conditions.	145
B.1 General conditions of study.	146
B.2 Blade-to-blade calculation (in the tip section).	147
B.2.1 Final grid spacing.	147
B.2.2 Simplified air-LH ₂ analogy for cavitation inception.	148
B.2.3 Inlet and other specific boundary conditions.	150
B.3 The meridional calculation.	151
B.3.1 Grid spacing and exit pressure condition.	151
B.3.2 Inlet velocity profile.	152
B.4 3-D calculation grid.	154
Appendix C. Secondary Velocity Analysis.	156
C.1 Definition of the grid for the iso- θ sections.	157
C.2 Definition of the Secondary Velocities.	159
Vita	161

List of Illustrations

Figure 1. Representation of the bladed elements in the LH ₂ turbopump.	3
Figure 2. The first helical blade row and the second shrouded blade row.	4
Figure 3. Cavitation visualization	8
Figure 4. Stripling and Acosta cavitation model	9
Figure 5. NASA investigations	10
Figure 6. Experimental facility at the Pennsylvania State University	14
Figure 7. Qualitative nature of the flow field inside inducer passages	18
Figure 8. Inducer exit measurements	19
Figure 9. Inducer exit measurements	20
Figure 10. Blade passage measurements	21
Figure 11. Blade passage measurements	22
Figure 12. Approximate viscid analysis	23
Figure 13. Inducer geometry for numerical analysis and notations used	26
Figure 14. Computations in turbomachinery	28
Figure 15. SEP inducer test facility	35
Figure 16. Blade outline and coordinate system definition	39
Figure 17. Leading edge definition	42
Figure 18. Blade intermediate deformation process	43
Figure 19. Level of approximation of the method	44

Figure 20. Grid definition process on the intermediate blade outline	47
Figure 21. Final grid definition on one blade	48
Figure 22. GEOMI format grid indices	50
Figure 23. Definition of the flowfield boundaries	54
Figure 24. Effect of camber at the leading edge for the upstream grid	55
Figure 25. FINAL BASIC GRID	57
Figure 26. FINAL BASIC GRID	58
Figure 27. Blade-to-blade calculation	61
Figure 28. Blade-to-blade calculation	62
Figure 29. Blade-to-blade calculation	63
Figure 30. Blade-to-blade calculation	64
Figure 31. Meridional calculation	66
Figure 32. Meridional calculation	67
Figure 33. Meridional calculation	68
Figure 34. Meridional calculation	69
Figure 35. Master geometry grid	71
Figure 36. Master geometry grid	72
Figure 37. Thermodynamic analysis of the flow	77
Figure 38. Notations used in the 3-D calculation.	81
Figure 39. Meridional views from the 3-D calculation results	82
Figure 40. Blade-to-blade views from the 3-D calculation results	83
Figure 41. Explanation of circumferential vortex.	84
Figure 42. Meridional views from the 3-D calculation results	86
Figure 43. Blade-to-blade views from the 3-D calculation results	87
Figure 44. Meridional views from the 3-D calculation results	88
Figure 45. Blade-to-blade views from the 3-D calculation results	89

Figure 46. Blade loading calculated distribution	90
Figure 47. Iso- θ planes definition process.	93
Figure 48. Static pressure distribution in iso- θ planes (a)	95
Figure 49. Static pressure distribution in iso- θ planes (b)	96
Figure 50. Cavitation occurrence along the leading edge in iso- θ planes	97
Figure 51. Secondary velocity vectors upstream of the leading edge	100
Figure 52. Velocity vectors in iso- θ planes (a).	101
Figure 53. Velocity vectors in iso- θ planes (b).	102
Figure 54. Tip leakage flow analysis in iso- θ planes	103
Figure 55. Tip leakage flow analysis in iso- θ planes	104
Figure 56. Rotary stagnation pressure loss distribution in iso- θ planes (a).	108
Figure 57. Rotary stagnation pressure loss distribution in iso- θ planes (b).	109
Figure 58. Evolution of the radial secondary velocity profile along the blade pas- sage	112
Figure 59. Numerical-experimental comparison	119
Figure 60. Numerical-experimental comparison; inlet station	120
Figure 61. Numerical-experimental comparison; inlet station	121
Figure 62. Numerical-experimental comparison; inlet station	122
Figure 63. Numerical-experimental comparison; inlet station	123
Figure 64. Numerical-experimental comparison; inlet station	124
Figure 65. Numerical-experimental comparison; inlet station	125
Figure 66. Numerical-experimental comparison; exit station	126
Figure 67. Numerical-experimental comparison; exit station	127
Figure 68. Numerical-experimental comparison; exit station	128
Figure 69. Numerical-experimental comparison; exit station	129
Figure 70. Numerical-experimental comparison; exit station	130

Figure 71. Numerical-experimental comparison; exit station	131
Figure 72. Loss analysis	133
Figure 73. Loss analysis	134
Figure 74. Definition of iso- θ planes	158

List of Tables

Table 1. Penn State inducer characteristics.	13
Table 2. SEP prototype inducer characteristics.	36
Table 3. General conditions of study.	36

Nomenclature

- c = chord length (m)
 c_p = specific heat capacity (J/kg.K)
 D = diameter (m)
 d_h = hydraulic diameter (m)
 g = gravitational acceleration (m^2/s)
 H = stagnation head rise (m), or rothalpy (J/kg)
 i = flow incidence angle relative to the blade (deg)
 k = cavitation number = $(p_1 - p_v) / (\frac{1}{2} \rho W_1^2)$
 K = cavitation parameter = $(P_1 - p_v) / (\frac{1}{2} \rho U_1^2)$
 N = rotation speed (RPM)
NPSH = Net Positive Suction Head (m) = $(P - p_v) / (\rho g)$
 p_{crit} = value of p at cavitation inception (Pa)
 p_v, p_{sat} = vapor pressure (Pa)
 p, p_s = static pressure (Pa)
 P, P_t = stagnation pressure (Pa)
 P^* = rotary stagnation pressure (Pa) = $p_s + \frac{1}{2} \rho W^2 - \frac{1}{2} \rho r^2 \omega^2$
 r = radius (m)
 R = gas constant (J/kg.K)
 Re = Reynolds number
 R_{ht} = hub/tip ratio
 s = entropy (J/kg.K)
 T = temperature (K)
 U = blade speed (m/s)

- V = absolute velocity (m/s)
 W = relative velocity (m/s)
 x = position along the blade chord (m)
 z = axial position (m)
- β = flow angle relative to axial direction (deg)
 β' = blade angle relative to axial direction (deg)
 γ = complement of blade angle (deg) = $90 - \beta'$
 η = hydraulic efficiency (Equation 5.4)
 ζ = loss coefficient (Figure 9a)
 θ = angular location (rad)
 λ = friction loss coefficient (Equation 5.5)
 λ_R = modified friction loss coefficient (Equation 2.1)
 μ = kinematic viscosity (kg/m.s)
 ω, Ω = rotation speed, scalar (rad/s) and vector notations.
 ρ = density (kg/m³)
 ϕ = flow coefficient = V_m / U_{tip}
 ψ = pressure or head rise coefficient
 ψ_s = static pressure coefficient = $(p_s - P_0) / (\frac{1}{2} \rho U_{tip}^2)$
 ψ_{loss} = rotary stagnation pressure loss coefficient = $(P_0 - P^*) / (\frac{1}{2} \rho U_{tip}^2)$

subscripts

- 0 = reference station upstream of inducer
 1 = inlet reference station
 2 = exit reference station
 i = primary flow direction (i-direction in calculation grid)
 m = meridional
 N = nominal
 r = radial
 R = stagnation
 sec = secondary
 t = total
 v = vapor

z = axial
 θ = tangential

superscripts

\bar{A} = A area-averaged
 $\underline{\bar{A}}$ = A mass-averaged

1.0 INTRODUCTION

The conquest of space has always required rocket engines with high specific power and with minimal penalties from the weight and size of the feeding and combustion systems. As a consequence, the rotational speed of the turbopumps used in liquid rocket feed systems has been increased, leading to the development of cavitation-resistant inducers. These are essentially axial-flow pumps with high solidity blading, used in front of the main pump. The length of the blades, usually 3 or 4, wrapped around almost 360 degrees, allows the cavitation bubbles to collapse before they exit the first blade row. At this point of the pump, the static pressure has been raised high enough to avoid further cavitation in the following elements of the pump.

The SSME oxidizer turbopump development under NASA contract was one of the first significant steps in cavitating rocket pump inducer research. Among other international efforts, the French "Société Européenne de Propulsion (SEP)" is currently developing a similar LH_2 pump inducer for the VULCAIN main engine of the future version ARIANE 5 of the European launcher. Figures 1 and 2 show its position among the other elements of the pump. It is the flow field in this inducer that we want to investigate in the present work.

Research efforts have been conducted for more than 25 years to provide a better understanding of the flow in this original feature of the modern rocket pumps. Although cavitation remains the principal limiting criterion in its design, great care is now also brought to increase the performance of the inducer and, as a result, of the whole pump. As a consequence, many authors have studied performance evaluation and 3-D flow patterns in noncavitating rocket pump inducers where the long and narrow blade passages make the viscous and secondary flow effects dominate with a large departure from

the design flow. However, most of them have restricted their work to experimental investigations or incomplete 2-D or 3-D flow model studies. This thesis presents the first known attempt to calculate the noncavitating flow in an helical rocket pump inducer, using a 3-D elliptic flow procedure with the capability of modeling real flows, including viscous terms in the Navier-Stokes equations and a turbulence model. The fluid considered throughout this study is air.

A brief literature review of previous work on rocket pump inducers starts this report, including experimental as well as analytical and numerical aspects; an outline of the method used in the flow calculation procedure used here concludes this first section, with references to more detailed descriptions already published. The scope and objectives of the project are then outlined.

A presentation of the generation of the calculation grid follows, with a discussion of preliminary two-dimensional blade-to-blade and meridional flow calculations.

Finally, a large section presents in detail the results of the 3-D, turbulent flow calculation performed for the inducer first blade row. An analysis of the flow inside the blade passages is discussed, with a description of tip leakage flow, viscous phenomena and secondary flows. The flow solution is also compared to available air test data, and a study of the losses at the exit of the blade passages concludes this work.

NOTE: As it appears from Figure 2, a blade-to-blade representation with a flow convention from left to right should show the blade velocity going up. However, in order to keep the usual representation of velocity triangles found in the literature, all the figures concerned here are inverted, with the flow going from left to right and the blade velocity going down.

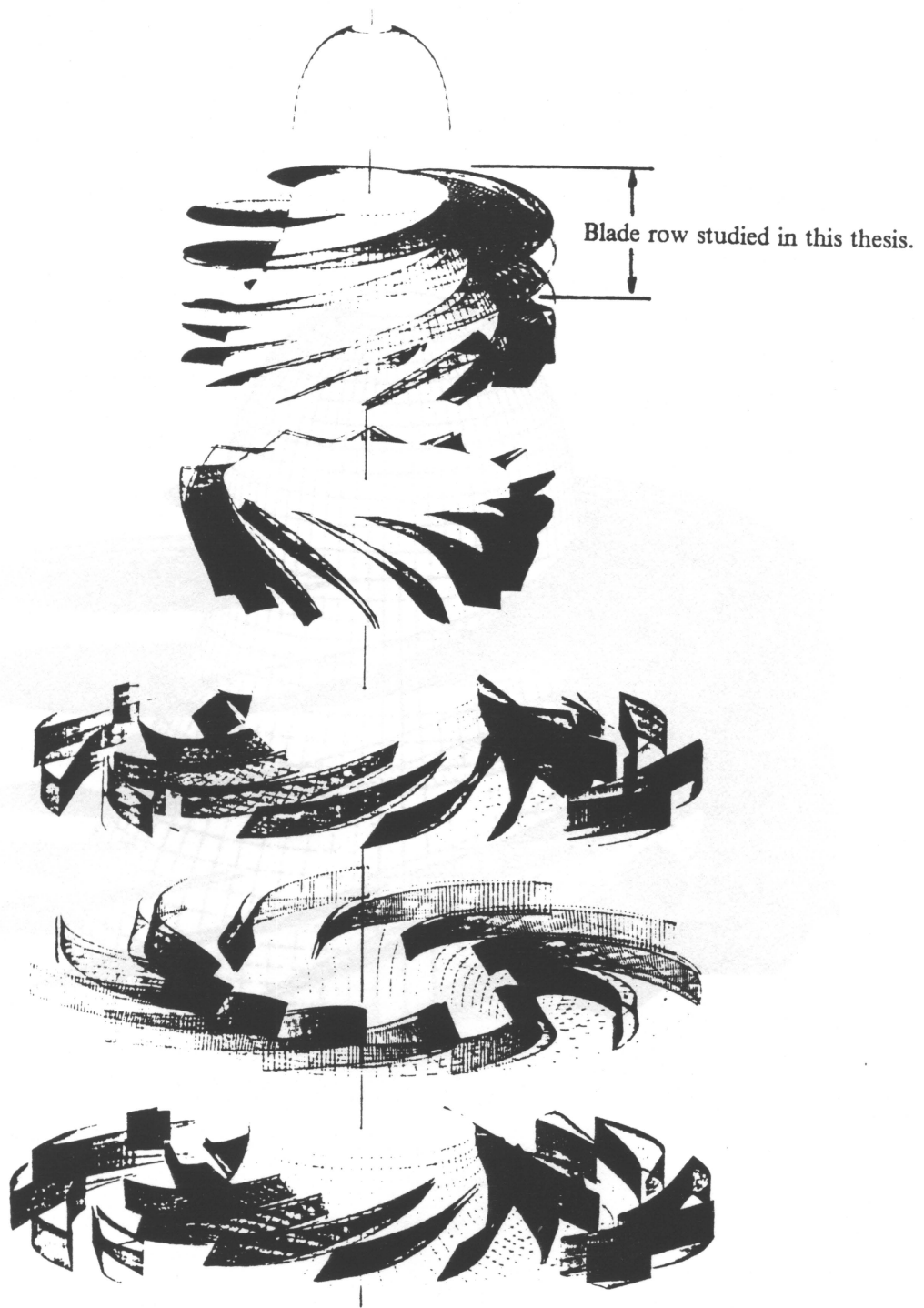


Figure 1. Representation of the bladed elements in the LH₂ turbopump.

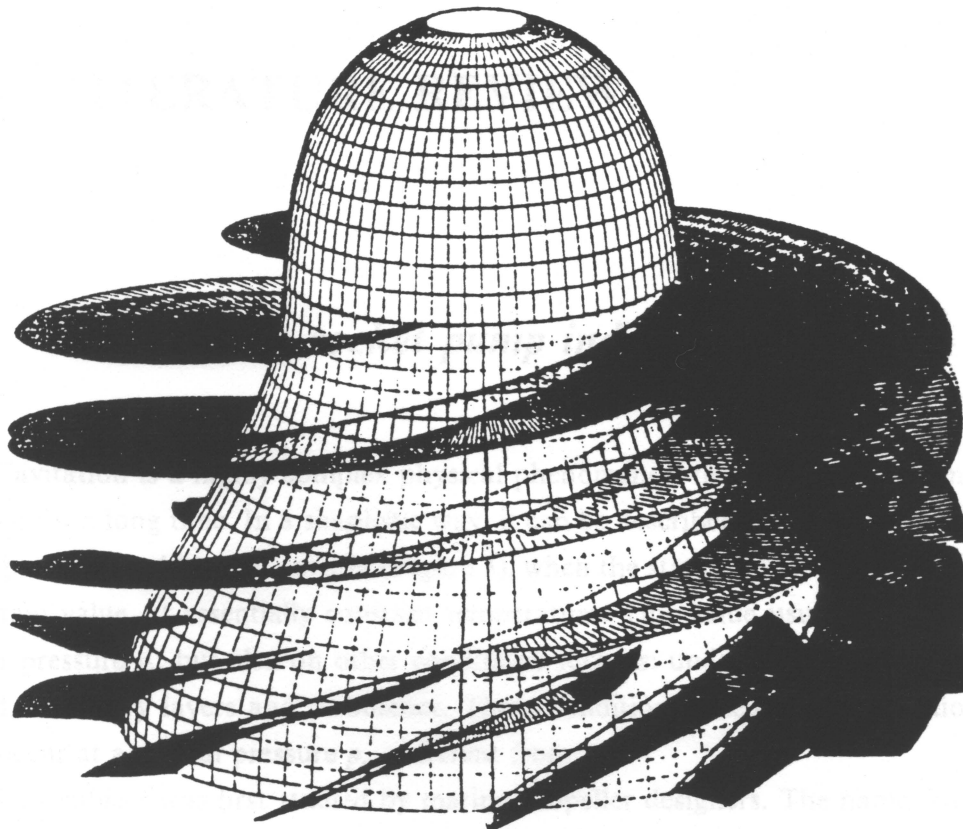


Figure 2. The first helical blade row and the second shrouded blade row.

2.0 LITERATURE REVIEW.

2.1 *Cavitation in rocket pump inducers.*

Cavitation is a highly complex physical phenomenon that has been recognized and studied for a long time. In a simplistic way, it can be described by the appearance of gas- or vapor-filled bubbles, or cavities (Figure 3), when the static pressure p is reduced below a certain value, at essentially constant temperature. This value usually depends on the vapor pressure p_v , but also on other conditions such as: undissolved gas particles in the liquid, boundary layers and turbulence. These conditions often make cavitation inception occur at a critical pressure p_{crit} different from p_v .

This subject was first studied by marine propeller designers. The name "cavitation" appeared in 1898, as a British destroyer could not meet its speed requirements due to the presence of cavities around the propellers (reference 1). Cavitation erosion was another critical effect that initiated research efforts in this new field.

A first important contribution to the understanding of cavity behavior was made by Lord Rayleigh in his 1917 article (reference 2). Dr. Knapp, late Professor at the California Institute of Technology, attempted to synthesize all investigations carried out in the first half of the century in his excellent general discussion of the cavitation phenomenon (reference 3).

"In recent years an increasing amount of attention has been devoted to problems of high-speed pumping systems", and: "it is, in fact, always desirable to operate a liquid pumping system at the highest possible speed, subject only to afore-mentioned limitations of cavitation". These two sentences expressed by Stripling and Acosta in 1962

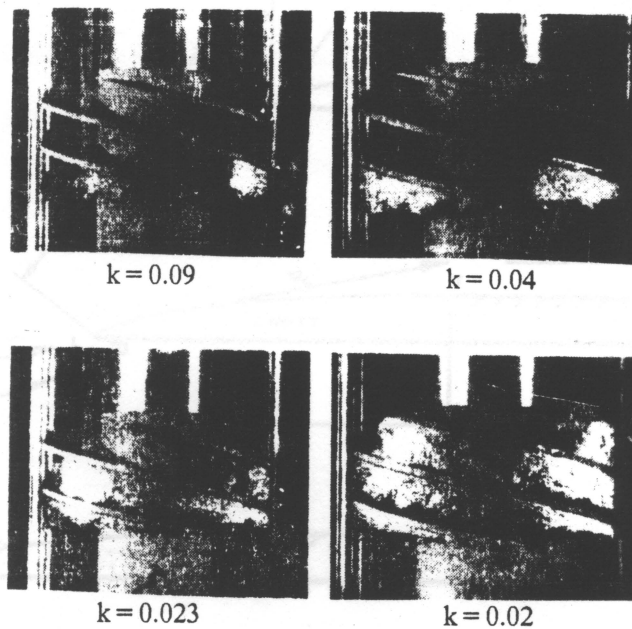
(reference 4) summarize the growing interest in cavitating high speed turbopumps in the early sixties, especially in applications for rocket pumps. In their paper, Stripling and Acosta present one of the first attempts to model numerically cavitation in an helical turbopump inducer. This simple model assumes that: 1- a fairly distinct cavity is attached to the leading edge on all blades; 2- the flow is two-dimensional, irrotational, inviscid and nonoscillatory; 3- the cavity shape is determined by a potential flow solution using the free-streamline originating at the blade leading edge (iso-pressure line) as the limiting boundary of the cavity (Figure 4); a semi-empirical approach defines a length c where the cavity ends sharply; the intensive mixing that takes place in the downstream wake is then evaluated (see reference 4); 4- the cavity pressure is constant and has a value equal to the vapor pressure corresponding to the bulk liquid temperature.

The sudden growth of interest in cavitation problems can be partly attributed to the beginning of the development studies for the Space Shuttle program. The evolution of the number of publications under NASA contracts on cavitation and cryogenic rocket pump inducers shows two large peaks in 1965-1966 and 1969-1971. Meng and Moore were among the principal investigators at NASA for cavitation studies on cryogenic pump inducers. In a series of papers (references 5, 6, 7), they investigated cavitation performance of an 80.6 deg. helical inducer operated in Liquid Hydrogen. The various configurations studied included the influence of the annulus wall as well as that of a stationary centerbody. The Net Positive Suction Head ($NPSH = (P_{total} - p_v) / (\rho g)$) requirements to avoid cavitation inception appeared to be lower for lower flow coefficients ($\phi = (\text{average axial velocity upstream}) / (\text{blade tip speed})$) and higher temperatures (thermodynamic effect, described in reference 3). Figure 5 represents these tendencies. In a specific study on thermodynamic effects (reference 8), measured values of NPSH showed a good agreement with those obtained using a semi-empirical prediction method based on results from venturi-investigations and reported in reference 9. A later report published in 1971 summarizes all previous work at NASA in a "Comparison of Noncavitation and Cavitation Performance for 78, 80.6, and 84 deg. Helical Inducers Operated in Hydrogen", with extensive data and graphs (reference 10). The 80.6 deg. inducer appears to be the best compromise for pressure requirements and thermodynamic effects (greatest for 84 deg. inducer), and noncavitating flow range (greatest for 78 deg. inducer).

Numerous other publications have been made in the past twenty years, providing a better - but still incomplete - understanding of the physics involved in cavitation. They

include extensive experimental efforts (references 11 and 12), as well as always more sophisticated numerical simulations. Reference 13 presents a literature review of the models of cavitation thermodynamic effect developed until 1986; reference 14 analyses some of the characteristic problems raised in cavitation modelling and reviews models available in the literature. Very few attempts can be found that include these models of cavitation in computer simulations of flow in inducers, probably because of the already high level of sophistication demanded by codes that calculate even noncavitating three-dimensional flows. However, we can cite the simplified attempts of Cooper (reference 15) and Brophy and al. (reference 16) that both use inviscid three-dimensional flow codes for a rocket pump inducer developed by Cooper and Bosch in 1966 (reference 28). A more recent study can be found in Schultz's work (reference 17).

Only few comments are made here on the studies mentioned above because this would go beyond the scope of the present thesis. The author intended only to underline the main problems encountered in cavitation study in rocket pumps, keeping in mind that this undesirable physical phenomenon is the only reason why inducers require such an original design.



Development of cavitation in a helical inducer with a 12-deg tip angle at a flow coefficient of $\phi = 0.12$ for various cavitation numbers, k .

Figure 3. Cavitation visualization: from Stripling and Acosta (reference 4).

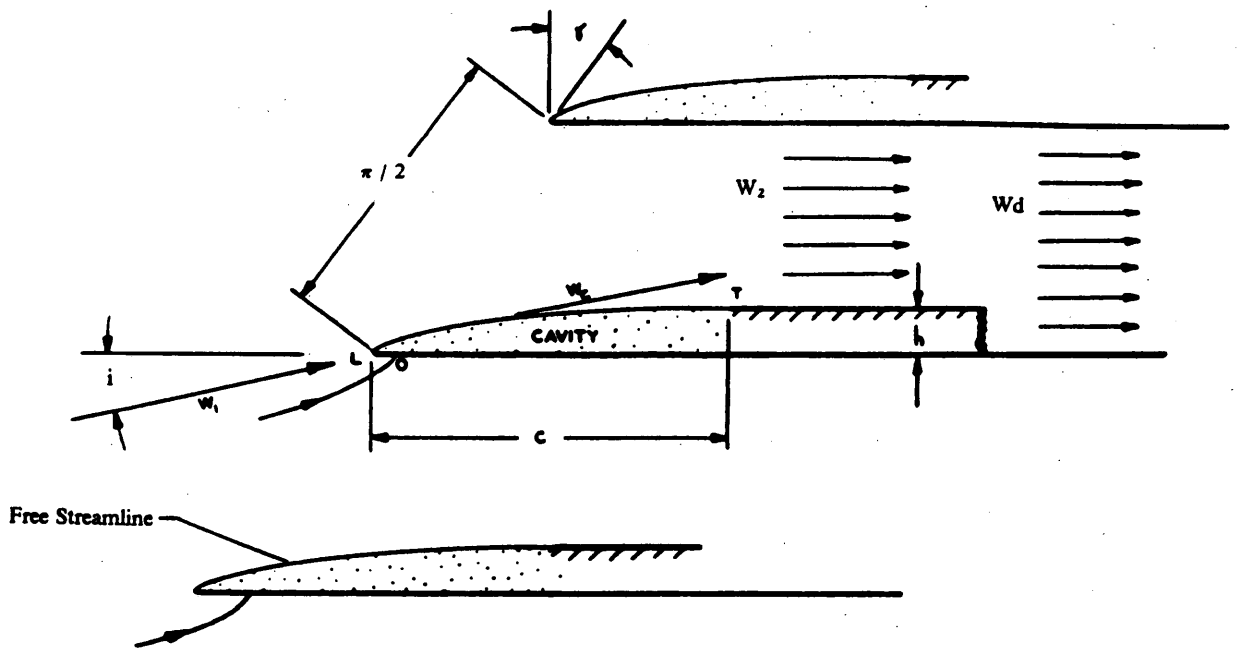
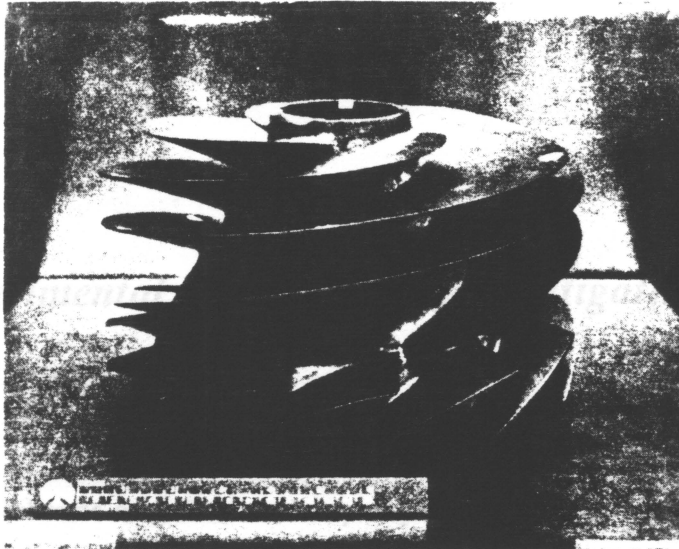
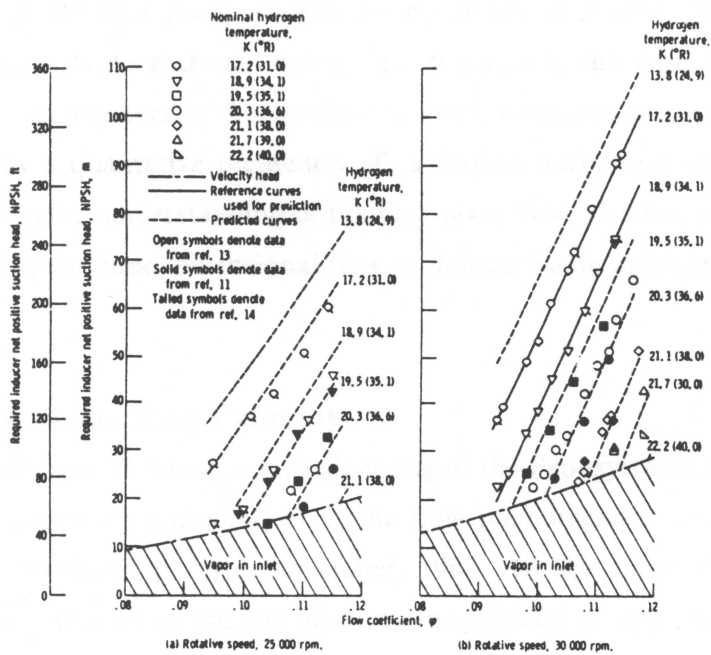


Figure 4. Stripling and Acosta cavitation model: cavity shape and free-streamline model.



5a. Photograph of the low pressure oxidizer turbopump inducer impeller used in the Space Shuttle Main Engine, $\phi = 0.07$, $SS = 70,000$ (reference 25).



5b. Effect of temperature and flow coefficient on required inducer NPSH (reference 10).

Figure 5. NASA investigations: cavitation occurrence in rocket inducer.

2.2 Experimental and analytical investigations in noncavitating conditions.

Experimental tests on helical rocket pump inducers were first made with cryogenic fluids to reproduce the operating conditions and show cavitation zones. Acosta started his investigations in 1958 (reference 18); Soltis and al., at NASA, published their first results in 1962 (reference 19). However, testing pumps in these real conditions is very expensive and causes many inconveniences. Therefore, studies have been successfully conducted to prove that pump overall performances and flow characteristics can be predicted in air tests, to a certain extent (no cavitation), and with reasonably good accuracy. King, an engineer at Rocketdyne in 1964, discusses this topic in reference 20. Of course, only a qualitative prediction of cavitation occurrence can be deduced from air tests, but a better understanding of the secondary flow, viscous, and mostly turbulent effects of the highly three-dimensional flow in inducer blade passages can be gained.

Studies at Pennsylvania State University.

The Department of Aerospace Engineering of the Pennsylvania State University has conducted investigation and analysis of the flow phenomena in rocket pump inducers under NASA sponsorship since November, 1963. All the experimental investigations were carried out with air as the test medium, the subjects of this study being the effects of viscosity and tip leakage, not that of cavitation. The main results obtained throughout this work are reported by the principal investigator, B. Lakshminarayana, in four papers cited in references 21 to 25. They summarize numerous other publications that were made by the research group at Penn State.

Experimental facilities and measurement techniques

The investigations carried out at Penn State included single-, two-, three-, and four-bladed inducers. In order to be consistent with the geometry studied in this report, only the results obtained for the four-bladed configuration are summarized here. The main geometrical and design parameters are listed in Table 1 (from reference 24) and the experimental facility is shown schematically in Figure 6.

The flow was visualized by means of very thin nylon tufts, smoke, ammonia streak, and lampblack techniques. Conventional as well as specialized pressure probes were employed for the measurements of the flow field at the exit and inside the passages of the inducer. Two stationary and rotating hot-wire anemometry techniques were developed at Penn State University for the measurements of three-dimensional flow in inducers. They are based on voltage signals picked up from the hot wires and converted into the three components of velocity and turbulence. More details on these measurement techniques can be found in the papers cited in reference 24, p.15.

Table 1. Penn State inducer characteristics.

Tip diameter		0.915 m
Hub/tip ratio at outlet		0.5
Hub/tip ratio at inlet		0.25
Radial clearance		1.5 mm
Suction specific speed SS (design)		50,000
Flow coefficient ($\phi = V_z/U_t$) (design)		0.065
Blade chord	Tip (R = 1.0)	2.1 m
	Mid-span (R = 0.75)	1.6 m
	Hub (R = 0.5)	1.26 m
Solidity (four-bladed inducer)	Tip (R = 1.0)	2.86
	Mid-span (R = 0.75)	2.91
	Hub (R = 0.5)	3.50
Number of vanes		4, 3, 2
Angular wrap (average)		290°
Lift coefficient of the blade based on mean velocity (four-bladed inducer)	Tip	0.0966
	Mid-span	0.163
	Hub	0.307
Reynolds number based on tip radius		6.60×10^5
Reynolds number based on relative velocity and chord at mid-radius		1.75×10^6
Maximum deviation of camber line from mean streamline $(\Delta n/L)_{\max}$	(R = 0.5)	0.02
	(R = 0.75)	0.01075
	(R = 1.0)	0.00637
Blade angles at inlet	(R = 0.25)	75°30'
	(R = 0.625)	83°30'
	(R = 1.0)	86°15'

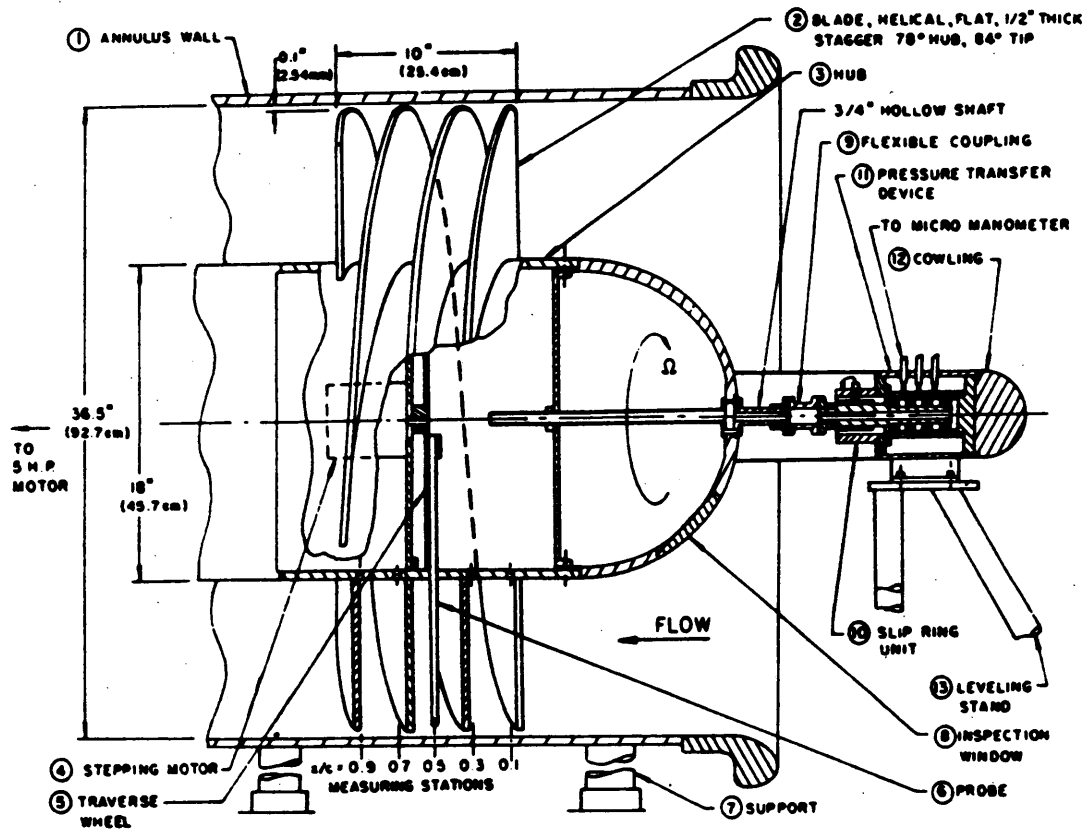


Figure 6. Experimental facility at the Pennsylvania State University: Flat-Plate inducer and rotating probe description (from reference 24).

Experimental results on the inducer flow field

In 1972, a flow visualization study in the passages of the four-bladed inducer showed the qualitative nature of velocity profiles and secondary flow inside the rotating passages (reference 21). Figure 7 shows the three-dimensional character of the flow and the important radial motions found throughout the passage.

Among the major conclusions made from this qualitative study, one can underline here the following:

- The radial motions within the blade passage are quite strong at all radii and increase continuously from leading to trailing edge of the blade. These radial flows are also generally higher near the suction surface than on the pressure surface.
- The radial flows inside the boundary layers are large from mid-radius to tip and, when encountered by the annulus wall, tend to deflect towards the mid-passage, and then radially inward.
- Secondary vortices are observed and found to be much larger near the hub than at the tip.
- A separated region exists near the hub at the inducer exit.

Thus, as expected from the highly skewed inducer geometry and the long and narrow passages encountered by the flow, the whole flow field is found to be dominated by secondary flow phenomena, turbulence, and viscous effects. The boundary layers are of a three-dimensional nature: they include both radial outward and inward flow, and extend over the whole passage.

Quantitative measurements confirmed the observations related above and produced an extensive data base for analysis and comparisons with other eventual investigations. Flow measurements were first carried out at several stations downstream of the inducer.

- As shown in Figure 8a, the stagnation pressure rise distribution is non-uniform and much higher at outer radii than near the hub. As the flow proceeds downstream, wake mixing and flow redistribution reduce the values of the stagnation pressure.
- The radial motions are confirmed by the exit measurements and radial velocities are found to be of the same order of magnitude as axial velocities, with increasing values towards the tip.

- The measured absolute tangential velocity is substantially higher than the design, especially from the mid-radius to the tip (see Figure 8b), due to radial flows and viscous effects.
- The flow losses, plotted in Figure 9, are much higher near the tip than at other radii. This is probably caused by a combination of mixing between pressure surface and suction surface boundary layers, that occurs in the tip gap, and higher skin friction near the blade at outer radii where the shear pumping effect becomes very important. The intense turbulence in this annulus wall region can also be cited as another explanation for these stagnation pressure losses.

Blade-to-blade distributions of flow properties at the exit of the inducer are also reported. The relative stagnation pressure coefficient measurements indicate considerable boundary layer thickening near the tip, confirming the presence of severe radial flow and blade boundary layer transport towards the tip.

From complementary measurements carried out with single helical blade configuration for boundary layer investigation and comparisons with rotating channel investigations, it was shown that viscous effects (as opposed to inviscid turning effects) play a major role in the pressure rise characteristics of the inducer, especially at the outer radii of the blade, permitting the figurative comparison with a shear pump advanced by Lakshminarayana in reference 22.

Original rotating hot-wire measurement techniques permitted investigation of the flow behavior inside the blade passages as well. The main features of the flow have already been mentioned above, and Figure 10 reproduces the main results obtained about radial velocities within the blade boundary layers.

Figure 11 shows the blade loading variation along the chord length.

Analytical prediction of the inducer flow field

From the insight gained through the extensive experimental work made, Lakshminarayana and his research group attempted different types of analysis to predict the inducer flow field. The most sophisticated one is a numerical three-dimensional viscous analysis based on empirical wall shear stress; it is described in the next section. Among

others, because of its simplicity and applicability to other inducers, only the approximate viscous analysis based on an empirical loss coefficient is presented here.

A new friction-loss coefficient applicable to inducers operating in the range of flow coefficients $\phi = 0.065$ to 0.2 is defined and derived from data collected from various sources (NASA, M.I.T., ...). The loss coefficient, λ_R , is given by:

$$\psi_{loss} = \frac{2gH_{loss}}{U_t^2} = \lambda_R \frac{R_{hr}}{\phi} \frac{1}{Re^{1/4}} \frac{c}{d_h} \left(\frac{\bar{W}}{U_t} \right)^2 \quad (2.1)$$

where λ_R is a function of radius, as shown in Figure 12a (cf. Nomenclature for the significance of the different terms used in this expression). The losses and efficiencies predicted from this empirical loss correlation are shown in Figures 9a and 9b.

With suitable assumptions and more empirical correlations discussed in reference 23, the radial distribution of the circumferentially averaged relative tangential velocity can be deduced from a circumferentially averaged radial equilibrium equation (see Figure 12b). Axial velocities can also be predicted, using continuity and axial momentum equations with assumed radial velocity profiles and the derived tangential velocity distribution.

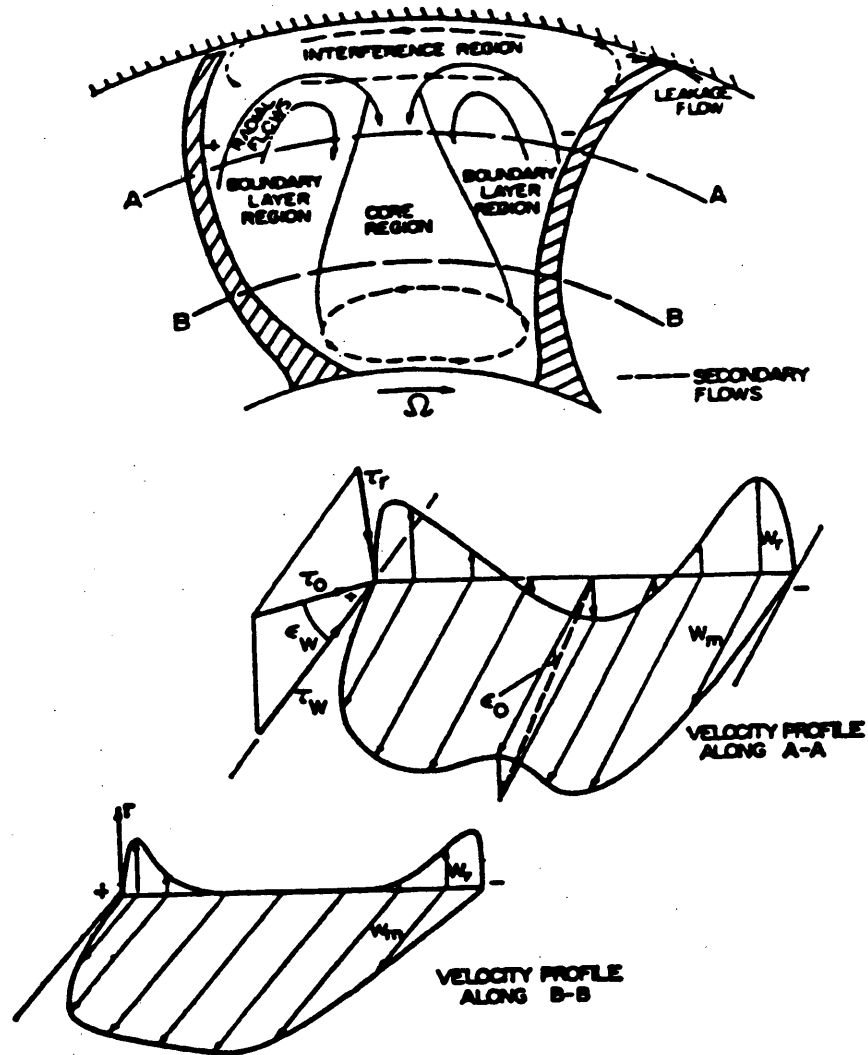
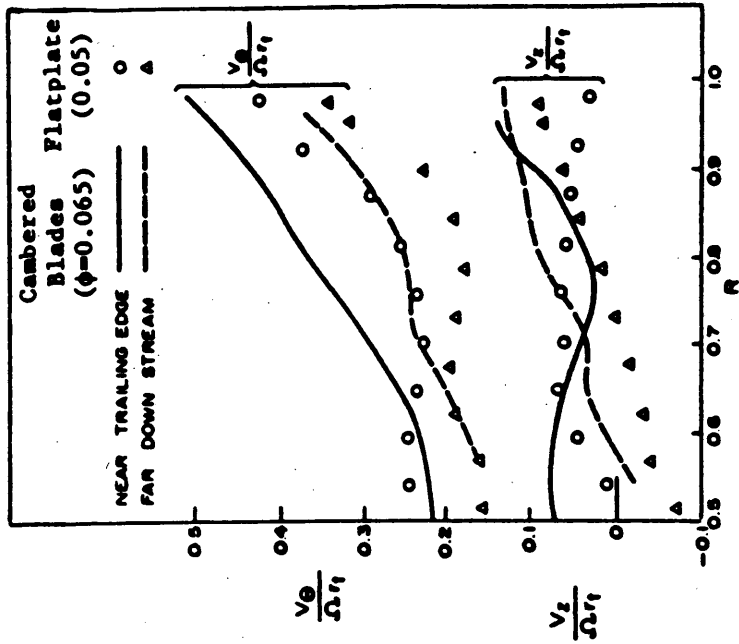
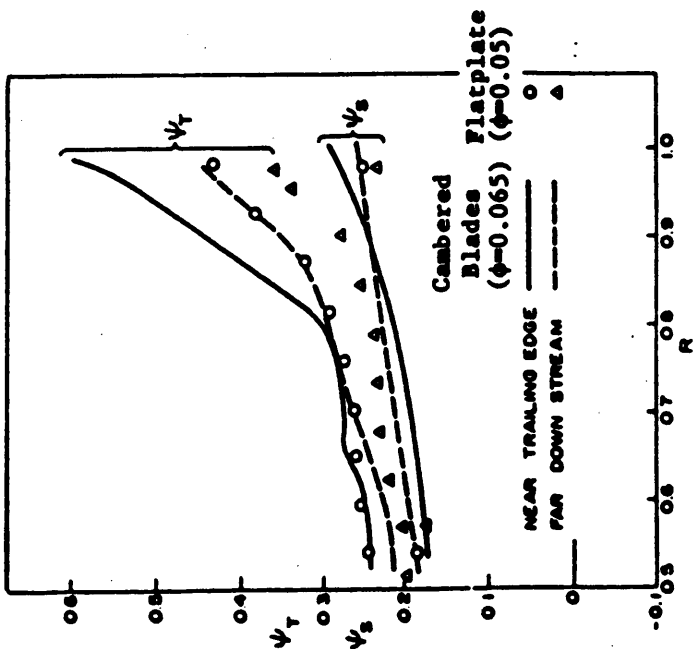


Figure 7. Qualitative nature of the flow field inside inducer passages: results from flow visualization (reference 21).

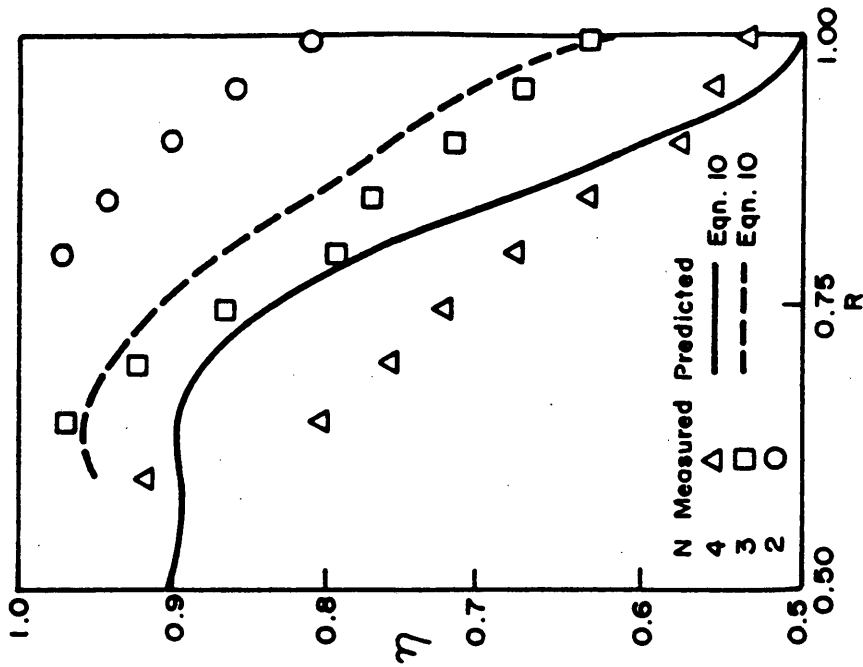


8a. Stagnation pressure coefficient (ψ_s) and static pressure coefficient (ψ_t).



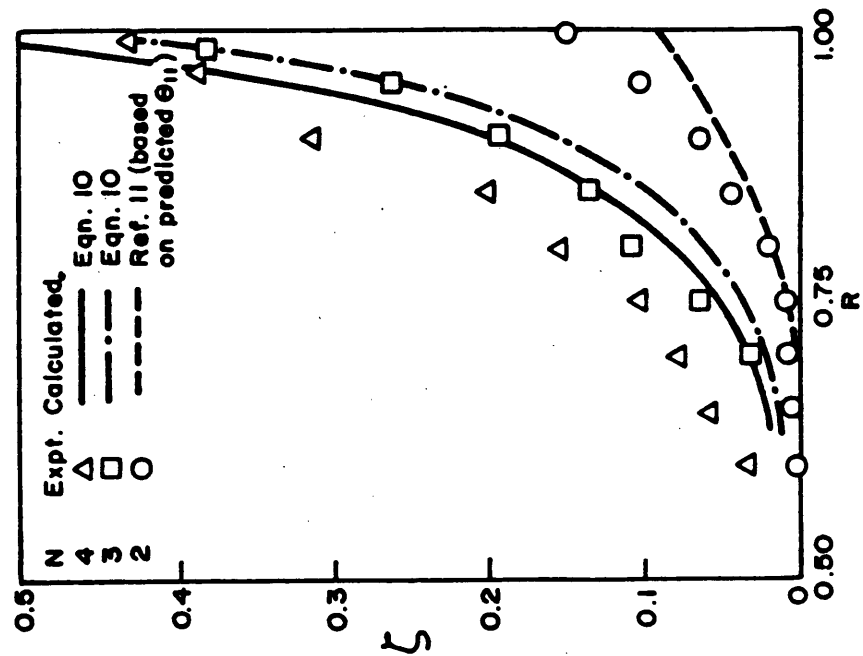
8b. Axial and tangential velocity profiles.

Figure 8. Inducer exit measurements: comparison of radial distribution of pressure rise and velocity profile for flatplate inducer and cambered bladed inducer (reference 24).



9a. Calculated and measured loss coefficient,

$$\zeta = \frac{\text{Euler pressure rise} - \text{Total pressure rise}}{\frac{1}{2} \rho U_{tip}^2}$$



9b. Radial distribution of local efficiency, η

Figure 9. Inducer exit measurements: flow losses and efficiency distribution (reference 24).

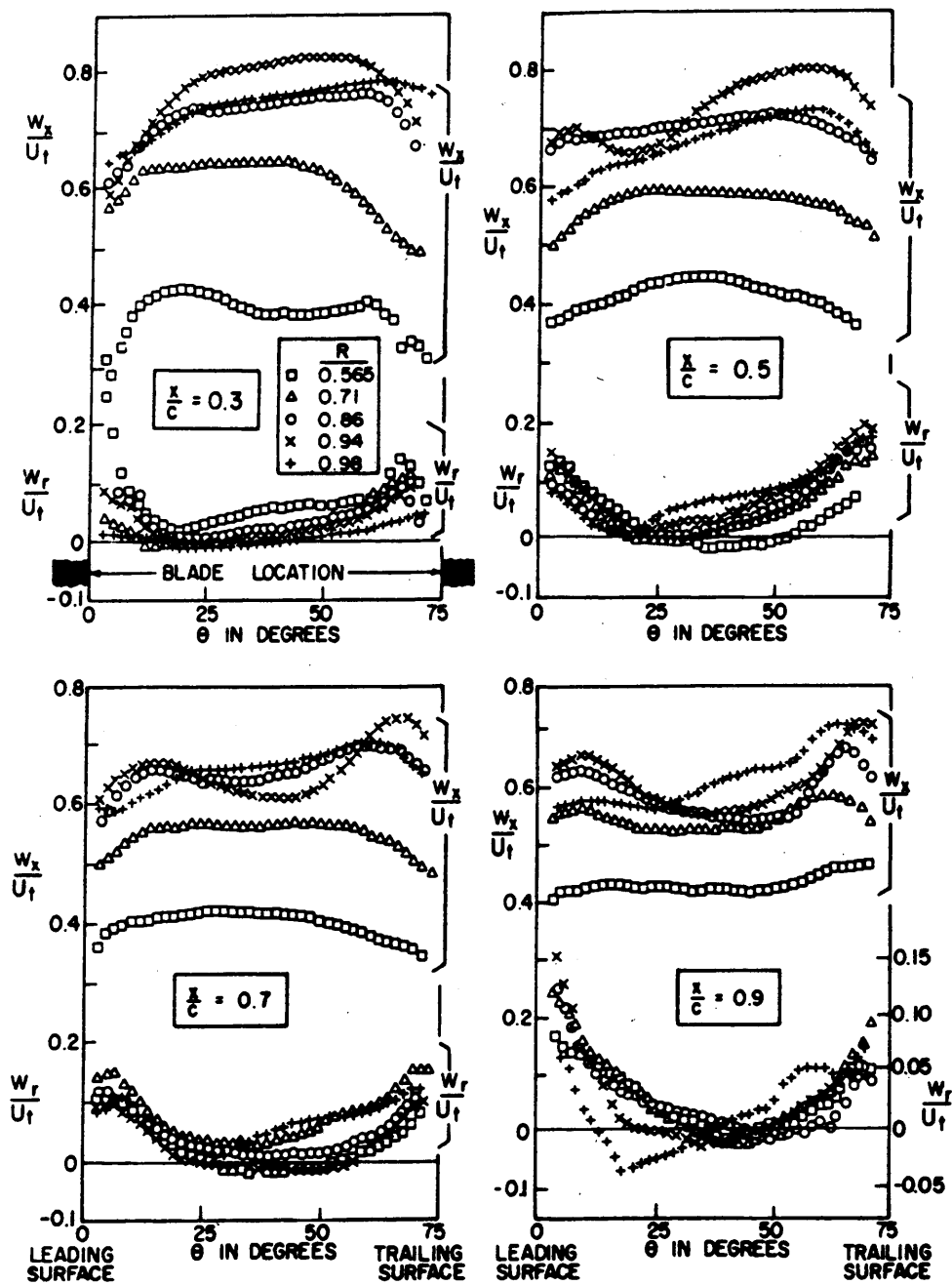
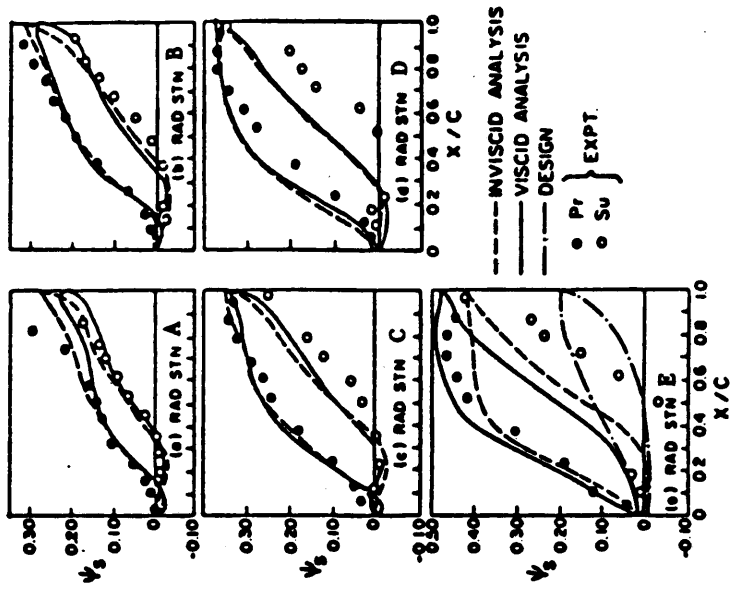
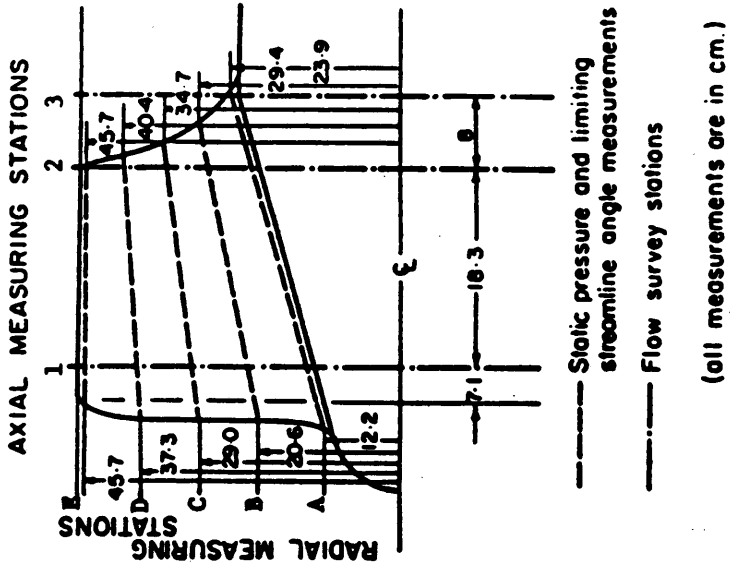


Figure 10. Blade passage measurements: blade-to-blade variation of streamwise and radial velocity profile for the Penn State flat-plate inducer (reference 24).

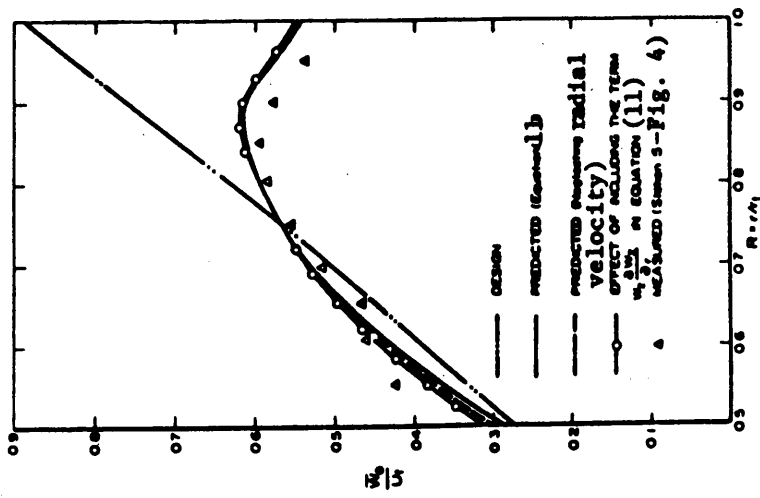


11b. Blade static pressure distribution.

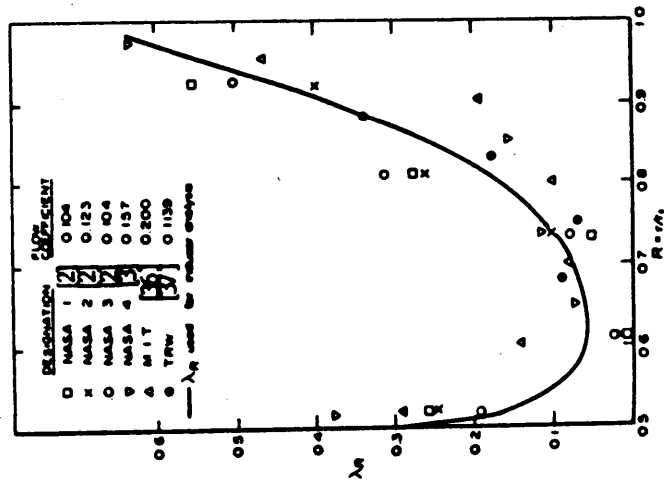


11a. Location of flow measuring stations.
(all measurements are in cm.)

Figure 11. Blade passage measurements: location of flow measuring stations and blade static pressure distribution (reference 24).



12b. Predicted and measured relative tangential velocity for Penn State's Four Bladed Inducer (reference 23).



12a. Radial variation of the Modified Friction Loss Coefficient λ_R , Equation 2.1

Figure 12. Approximate viscid analysis: comparisons (reference 24).

2.3 Previous computational studies.

Computational methods for flow in turbomachinery have been developed for more than 25 years. Following the increasing computer capability and improving physical understanding of flow phenomena, calculations have been made possible for 3-D flows and, in the recent years, viscous effects have started to be taken into account.

One of the first authors to present a method of analysing flow through a turbomachine that was suitable for computer programming was T. Katsanis in 1964 (references 27, 28). His code calculates the flow in two steps, using separately meridional and blade-to-blade surfaces before combining the results in a quasi three-dimensional solution. The development of the rocket pump inducer urged the need for improved numerical solutions capable of handling the largely three-dimensional flows and eventually including simple models of cavitation. P. Cooper and H. Bosch, at NASA, published a most important "Three-Dimensional Analysis of Inducer Fluid Flow" in 1966 (reference 29). This original version of the code calculates the exact inviscid solution for the incompressible, noncavitating flow field in the inducer. Cooper, in 1967 (reference 15), and then Brophy and al., in 1983 (reference 16), implemented a suitable cavitation model. In 1977, C. A. Gorton and B. Lakshminarayana developed and tested an improved version of the calculation procedure that included viscous effects (reference 30).

Exact inviscid analysis

The Cooper and Bosch three-dimensional analysis employs an iterative numerical procedure to solve the equations of motion expressed in finite-difference form. Poncet and Lakshminarayana (reference 31) first improved the method by automatically forcing the Kutta-Joukowski condition for the blade pressure distribution to be satisfied (trailing edge closure).

Approximate viscid analysis

In order to incorporate viscid effects into the governing equations of motion, Gorton and Lakshminarayana (reference 30) then approximated the viscous terms in the mo-

momentum equations by retaining the dominant shear stress terms only and neglecting the normal stresses. Molecular viscosity terms were also neglected.

The distribution of shear stress was derived from measured wall shear stresses, assuming linear variation across the passage from pressure surface to suction surface (a fully developed flow approximation). The component along each coordinate direction was assumed to vary according to the ratio of the corresponding local velocity component to the total relative velocity. Figure 11 compares the results obtained for the blade static pressure distribution by this viscid analysis with design, experimental data, and the inviscid solution.

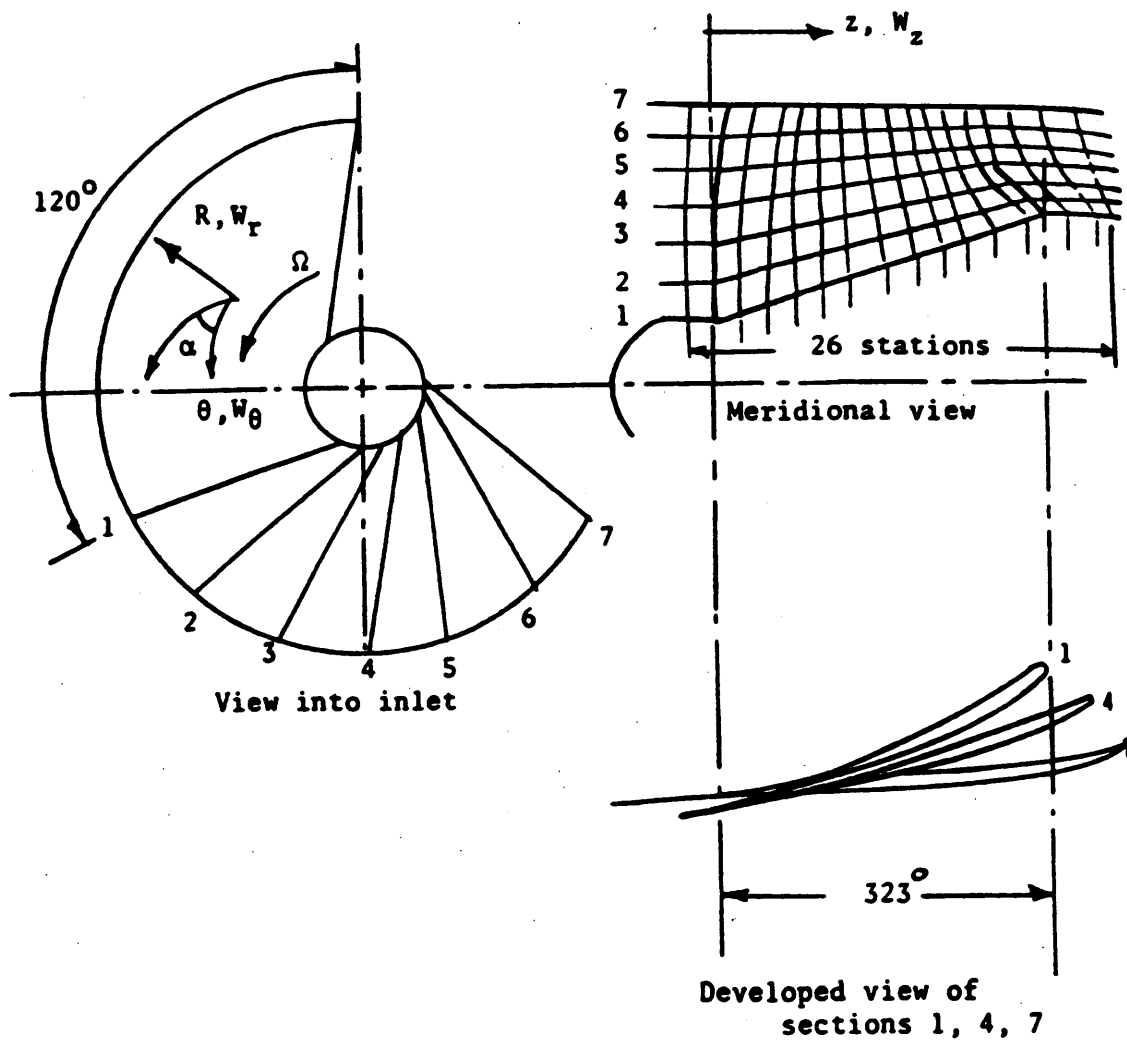


Figure 13. Inducer geometry for numerical analysis and notations used: (reference 30).

Recent developments

Among the recent developments in numerical solutions for turbomachinery, very few applications can be found that are suitable for rocket pump inducers. In reference 32, a review of various pressure correction computer techniques is presented. Most of these codes use parabolic marching techniques that cannot handle backflows, and thus, cannot be used for inducer geometries with large stagger angles. Moore and Moore proposed a viscous 3-D elliptic flow calculation procedure that has been successfully tested on turbines and centrifugal compressors (references 32, 33, 34, 35). Figure 14 shows the advantages of such an elliptic method compared to other classic approaches. It is this method that has been used in this project, and a description of it is presented in the next section.

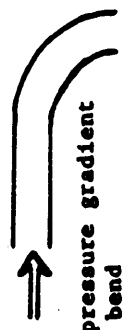
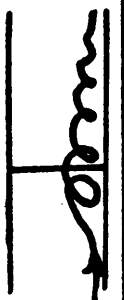
	Parabolic	Partially-Parabolic	Elliptic
<u>Effects transmitted upstream</u> <u>Pressure</u>  e.g. transverse pressure gradient upstream of bend	NO	YES	YES
<u>Mass (reverse flow)</u>  e.g. horseshoe vortex	NO	NO	YES
<u>Viscous transport</u>  e.g. viscous transport of momentum $\mu \frac{\partial u}{\partial x}$ flow, u	NO	NO	YES
<u>Example of solution procedure</u>	Space marching	Space marching with estimated pressure	Time marching
<u>Solution domain</u>	Successive 2-d planes	Successive 2-d planes, repeated a few times with a method of improving the estimated pressure	3-d grid

Figure 14. Computations in turbomachinery: comparison between various numerical approaches (reference 32).

2.4 The Moore elliptic flow program (MEFP).

The physics of most steady flow phenomena of interest in turbomachinery is described by the following Steady Flow Conservation Equations (written in the rotating reference frame):

Mass:

$$\nabla \cdot \rho \mathbf{W} = 0$$

Momentum:

$$\rho \mathbf{W} \cdot \nabla \mathbf{W} - (\nabla \cdot \mu \nabla) \mathbf{W} = \nabla \cdot \mu \nabla \mathbf{W} - \nabla p - 2\rho \boldsymbol{\Omega} \times \mathbf{W} - \rho \boldsymbol{\Omega} \times (\boldsymbol{\Omega} \times \mathbf{r})$$

Equation of state:

$$p = \rho RT$$

Rothalpy (energy):

$$\rho \mathbf{W} \cdot \nabla H - (\nabla \cdot \mu \nabla) H = 0$$

$$H = c_p T + \frac{1}{2} (\mathbf{W} \cdot \mathbf{W}) - \frac{1}{2} (\boldsymbol{\Omega} \times \mathbf{r} \cdot \boldsymbol{\Omega} \times \mathbf{r})$$

Second law of thermodynamics:

$$s - s_0 = c_p \ln\left(\frac{T}{T_0}\right) - R \ln\left(\frac{p}{p_0}\right)$$

The momentum equation is used to solve for the three components of the relative velocity vector \mathbf{W} , the energy equation is used for the rothalpy H , the definition of the rothalpy for the temperature T , and the second law equation for the entropy s . The Moore 3-D viscous flow program is a pressure-correction calculation procedure, and thus, the continuity equation is used to solve for the pressure p while the equation of state gives the density ρ . In time-marching methods, the unsteady continuity equation gives the density and the equation of state the pressure.

In our incompressible flow case, only the mass and momentum equations are used, the state equation being replaced by: $\rho = \text{constant}$.

For the turbulent flow calculation performed, the flow equations are coupled with a Prandtl mixing length model of the turbulent viscosity, with a Van Driest correction, as described below.

$$\mu = \mu_{\text{laminar}} + \mu_{\text{turbulent}}$$

$$\mu_{\text{turbulent}} = \rho L^2 \frac{du'}{dy}$$

where L is the smaller of:

- 0.08 times width of shear or boundary layer,
- 0.41 times distance to nearest wall.

Van Driest Correction:

$$L = 0.41y \left(1 - \exp\left[-y' \frac{\sqrt{\rho\tau}}{26\mu_{\text{laminar}}} \right] \right)$$

Near-Wall Correction:

$$\mu = \sqrt{\mu_{\text{laminar}} \cdot \sqrt{\mu_{\text{laminar}} + \mu_{\text{turbulent}}}}$$

The discretization of the equations and the details of the application of the pressure-correction method for an elliptic calculation are given in reference 33. An outline of the procedure is also reproduced in the following flow diagram.

- 1- Initial 3-D estimate of flow W , p , ρ , T , H
(only W and p for incompressible flow).
- 2- Calculate viscosity.
- 3- Finite difference coefficients for momentum and energy equations.
- 4- Calculate density $\rho = p/RT$
(omit for incompressible flow).
- 5- Evaluate W from momentum scalar equations.
- 6- Continuity equations:
Finite difference momentum correction equations

- + Finite difference continuity equation
- = Finite difference pressure correction equations.
- 7- Solve for p_c .
- 8- Update W from momentum correction equations.
- 9- Update p .
- 10- Solve finite difference energy equation for H
(omit for incompressible flow).
- 11- Calculate T, s etc
(omit for incompressible flow).

Repeat from Step 2.

3.0 SCOPE AND OBJECTIVES OF THIS RESEARCH.

The need for improved numerical method for flow field investigations.

Within the framework of the development of the VULCAIN cryogenic engine for the European launcher ARIANE 5, SEP has conducted studies to design a new cavitating helical inducer for the LH₂ turbopump. A prototype has been studied by two means of investigation. First, a calculation of the flow field inside the blade passage was attempted, using the method developed by Katsanis and discussed in the literature review. The code showed numerous limitations, especially because of the large stagger angle, and was finally abandoned. Recently, intensive test campaigns have been undertaken. Water tests have shown cavitation inception through flow visualizations; air tests have also been conducted to study the viscous effects for noncavitating conditions. In both cases, correlation methods are then applied to predict the cryogenic flow behavior. A summary of the air tests is presented in reference 26.

Figure 15 gives a general representation of the test configuration for the inducer's first blade row. This test facility presents several major limitations: 1- Only two planes are investigated, providing circumferentially averaged values of the physical properties at the inlet and at the exit. There is no information available about the flow behavior inside the inducer passages. 2- No test has been conducted with only the first helical blade row, and the proximity of the second blade row has probably a major influence on the measurements of the exit plane. Moreover, because of the small interspace between the two rows and the diameter of the probe stem, less than half of the exit passage

height could be investigated. 3- The physical presence of the probe tips provokes also an undesirable flow disturbance.

These problems and limitations show the need for "non intrusive" flow measurements and accurate improved numerical flow investigations. It is this thesis' concern to present the main steps of the flow calculation performed and the analysis of the results obtained.

The calculation conditions

The main characteristics of the inducer configuration studied in this thesis are summarized in Table 2. The actual geometry used in the calculation differs slightly from the prototype tested by SEP. The grid over the inducer blade had to be completely re-defined, with only the blade outline definition as correct available data to start with. This task constitutes the first step of the research project presented here.

The medium considered in the simulation is air, since we are only interested in the study of viscous phenomena, tip leakage and flow distribution inside the blade passages, not with cavitation. The general conditions of study are presented in Table 3.

The flow calculation carried out used a 3-D elliptic procedure including real flow effects and developed by J.G. Moore and J. Moore (*) at the Virginia Polytechnic Institute and State University. The large stagger angle at the inlet of the inducer produces backflows and vortices that no time-marching technique can represent with reasonable present computer storage capability and computation time. The code used has been successfully tested on turbine and centrifugal compressor geometries. It was the first time that such a critical geometry was submitted to the program, and no previous similar viscous 3-D elliptic calculation has been reported in the literature. Therefore, special care had to be devoted to the flow field grid definition in order to represent accurately the flow phenomena with reasonable CPU time on the IBM 3084 available at VPI&SU. Preliminary 2-D blade-to-blade and meridional flow calculations were performed in order to optimize the final calculation grid and define the boundary conditions.

(*) Faculty members at VPI&SU.

Analysis of the results

The general objective of this research was to produce numerical data for the flow properties at the inducer inlet, in the blade passages, and downstream of the first blade row. A large number of plots of the flow property distributions was produced in suitable forms to help us to recognize and interpret some of the main features in the flow pattern. The level of resolution of the flow calculation also revealed original details poorly described in the literature, if not completely ignored.

From the study of the static pressures, we were able to predict the regions where cavitation inception is likely to occur, based on a simplified air-LH₂ analogy.

An essential step in the analysis of the numerical solution being the justification of the validity of the flow model, a comparison between the results and available air test data provided by SEP is also presented.

Finally, a succinct analysis of the losses uses Lakshminarayana's work and data from other inducer configurations.

Some general comments and propositions to improve the design of the helical inducer conclude this work.

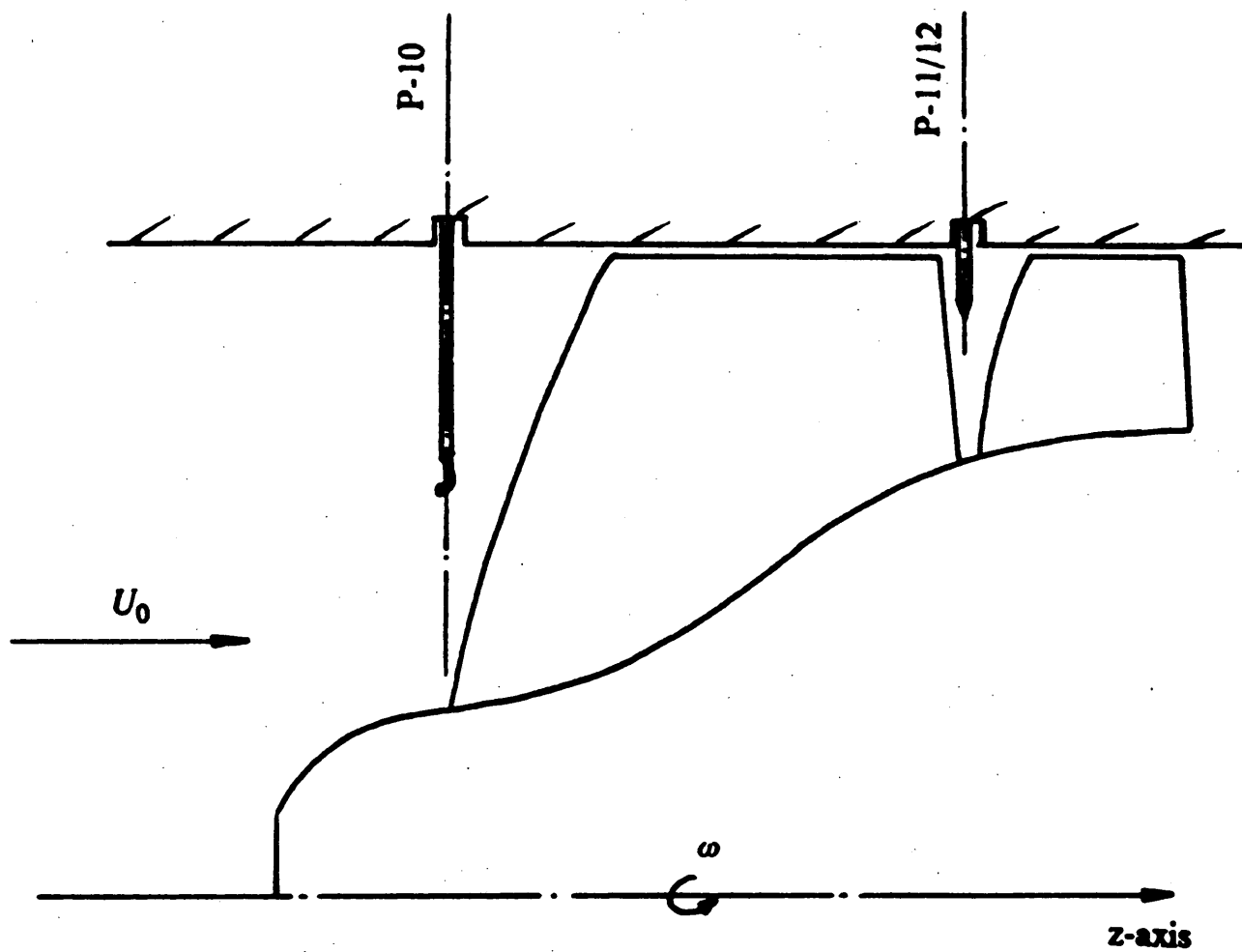


Figure 15. SEP inducer test facility: location of the measurements planes.

Table 2. SEP prototype inducer characteristics.

tip diameter (mm)	90.90
outlet hub/tip ratio	0.69
inlet hub/tip ratio	0.425
radial clearance (mm)	0.5
suction specific speed	64,000
inlet flow coefficient, ϕ	0.07
number of vanes	4
average angular wrap	280°
Reynolds number (based on tip diameter) $Re = (\rho U_{tip} D) / \mu$	1,100,000
blade angles at inlet	
hub	71.2°
tip	82°

Table 3. General conditions of study.

ρ_0 (kg/m ³)	1.225
P_0 (Pa)	101,325
T_0 (K)	288.15
Q_{air} (kg/s)	0.2109
N (RPM)	10,000
inlet flow coefficient, ϕ	0.07
Reynolds number (based on tip diameter) $Re = (\rho U_{tip} D) / \mu$	1,100,000

4.0 GENERATION OF A 3-D FINITE DIFFERENCE GRID FOR THE HELICAL INDUCER.

4.1 *Definition of the blade.*

4.1.1 Cylindrical coordinate system used and data provided.

Considering the nature of the helical inducer, the geometry definition is made in cylindrical coordinates. This coordinate system is classically defined with the following notations: radial component r , tangential component θ , axial component z . The z -axis is the rotation axis oriented downstream. The tangential orientation chosen defines a right-hand coordinate system. Relative to the reference blade defined below, the origin of the coordinate system is at:

$r=0$ on the rotation axis;

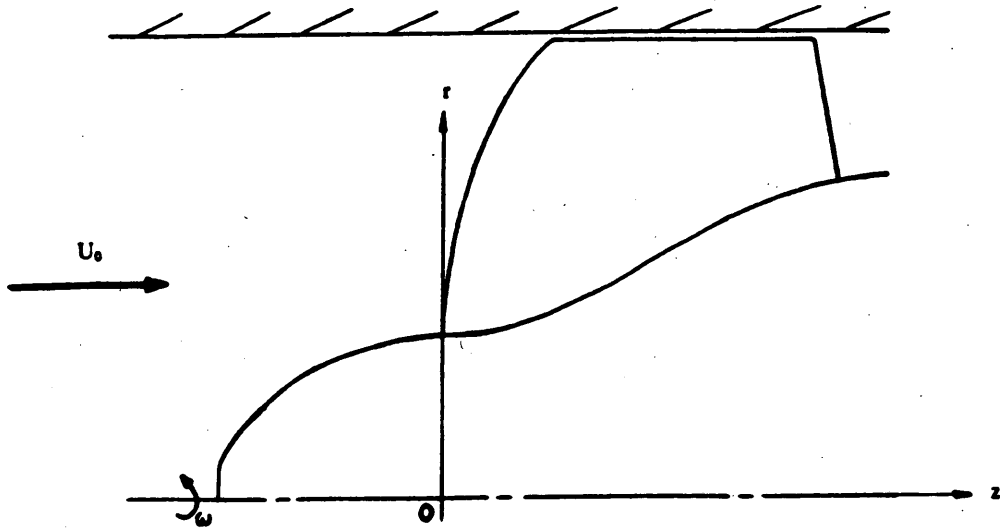
$\theta=0$ at the trailing edge, on the pressure side;

$z=0$ at the intersection of the leading edge with the hub, on the pressure side.

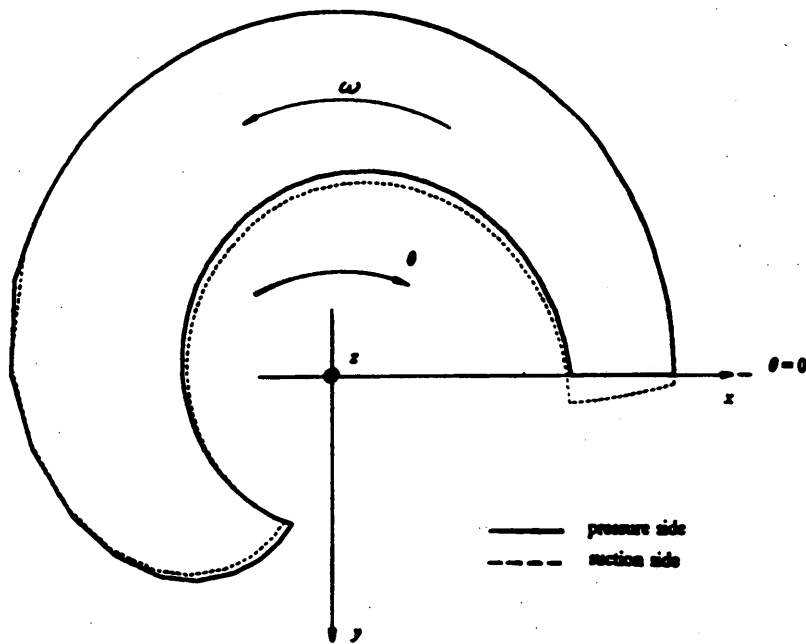
Using the axisymmetry of the four-bladed inducer, only one "reference blade" has to be defined. The data file provided by S.E.P. contains the Hub-,Tip-,Leading edge- and Trailing edge-outline of the blade for both pressure and suction sides. This information is given in an r, z, θ -pressure side, θ -suction side format. There are 40 sections

in the axial direction (hub and tip definition) and 11 sections in the radial direction (leading and trailing edges).

Figure 16 shows the blade outline in a meridional view and in an axial view, with a representation of the conventions adopted.



16a. Meridional view: definition of r and z coordinates.



16b. Axial view: definition of r and θ coordinates.

Figure 16. Blade outline and coordinate system definition: meridional and axial views.

4.1.2 Generation of a finite difference grid over the reference blade.

4.1.2.1 *Some complementary choices.*

In order to complete the basic input data for the geometry specification, the shape of the leading and trailing edges as well as the complete surface thickness distribution have to be defined. The approximations used for this purpose are now presented.

Leading edge and trailing edge shapes.

The two main manufacturing requirements at the leading edge are: maximum sharpness and presence of a sharp angle on the suction side in order to promote cavitation (and thus, control it). These are satisfied by determining a straight leading edge profile as shown in Figure 17. For each one of the 11 blade-to-blade sections of the basic data file, at the leading edge, one has generated straight segments between corresponding points on the pressure side and the suction side. The result is then a flat chamfer.

The same procedure has been applied to the trailing edge. This simple arbitrary shape is not expected to have a significant effect on the calculation of the overall three-dimensional flow field.

Surface thickness distribution.

The data file provides the blade profile at the hub and at the tip as well as the thickness distributions at the leading edge and at the trailing edge. In order to interpolate between these distributions and define the pressure and suction surfaces, a procedure involving straight iso- θ lines and linear interpolation between the "inner" hub section and the "outer" leading edge-tip section is proposed. This procedure has been inspired by the CAD definition used by SEP and reproduced in Figure 2.

Figure 18a represents a meridional view of the reference blade outline showing lines of constant θ . In the basic input file, the trailing edge is defined with a constant $\theta=0$ distribution on the pressure side. By stretching the blade contour with a transformation F of the z -coordinate that makes the trailing edge a radial line on the pressure side, one obtains the new outline shown in Figure 18b. The iso- θ lines in this new (r, θ, z') coordinate system are now very close to being radial lines, as shown in Figure 18c. Figure

19 represents the angular distribution θ versus z for the hub and the tip in the old (r, θ, z) and the new (r, θ, z') coordinate systems. The pressure side lines, as well as the suction side ones, match with a good agreement in the new coordinate system. This confirms that the transformation F gives a geometry in which the iso- θ lines of the blade closely correspond to radial lines. We use this fundamental geometric property to obtain a more accurate definition of any point of the blade surface by defining its θ -component by linear interpolation between the "inner" and "outer" contour lines, for its given z' -component.

The geometric transformation F between the (r, θ, z) and the (r, θ, z') coordinate systems is defined by:

$$z' = z + a + b r(z);$$

$$F(A) = A;$$

$$F(B) = B';$$

where a, b are numerical constants and A, B, B' are the geometric points defined in Figure 18b.

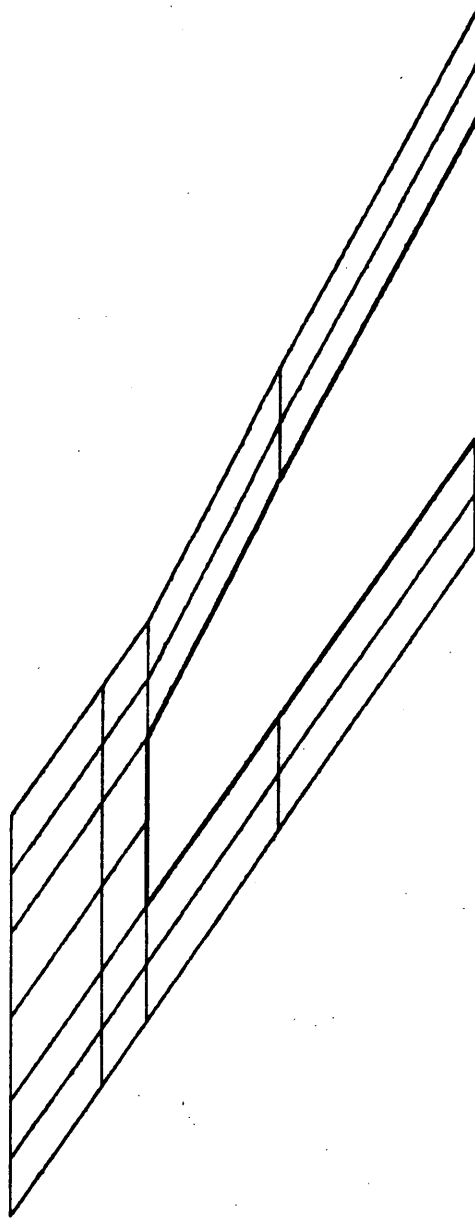
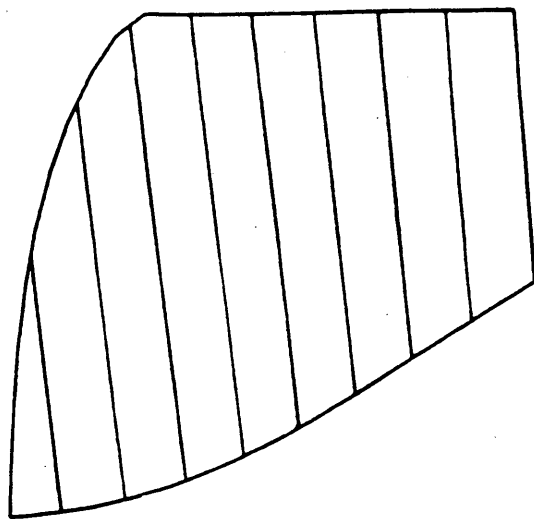
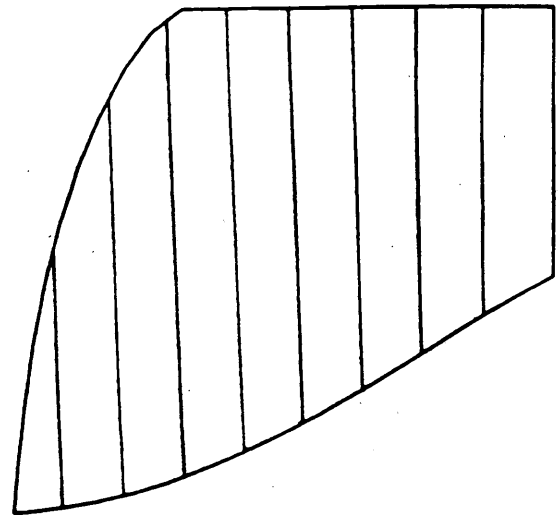


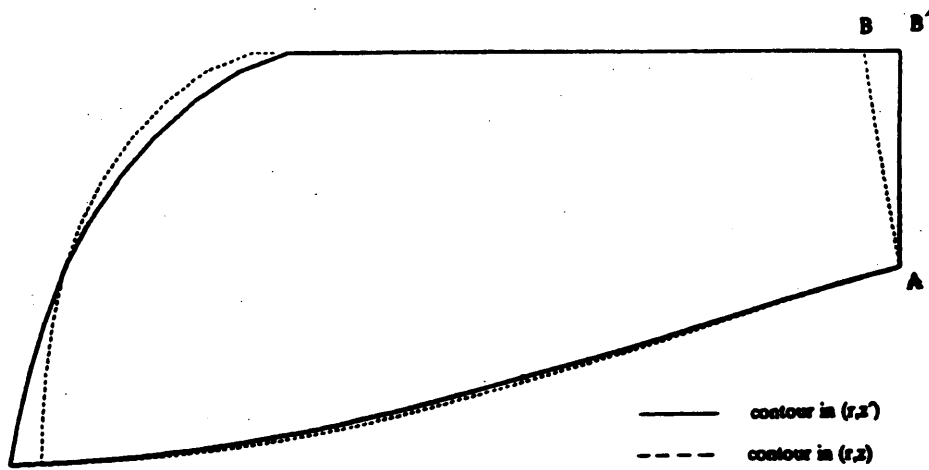
Figure 17. Leading edge definition: Grid viewed in blade-to-blade plane.



18a. Iso- θ lines on blade outline in (r, z)

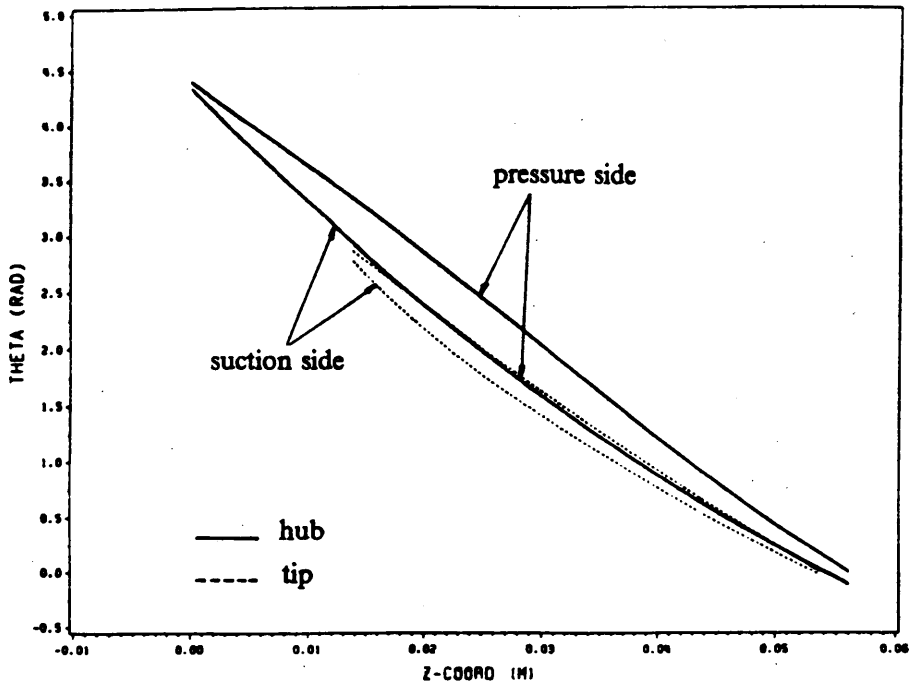


18c. Iso- θ lines on blade outline in (r, z')

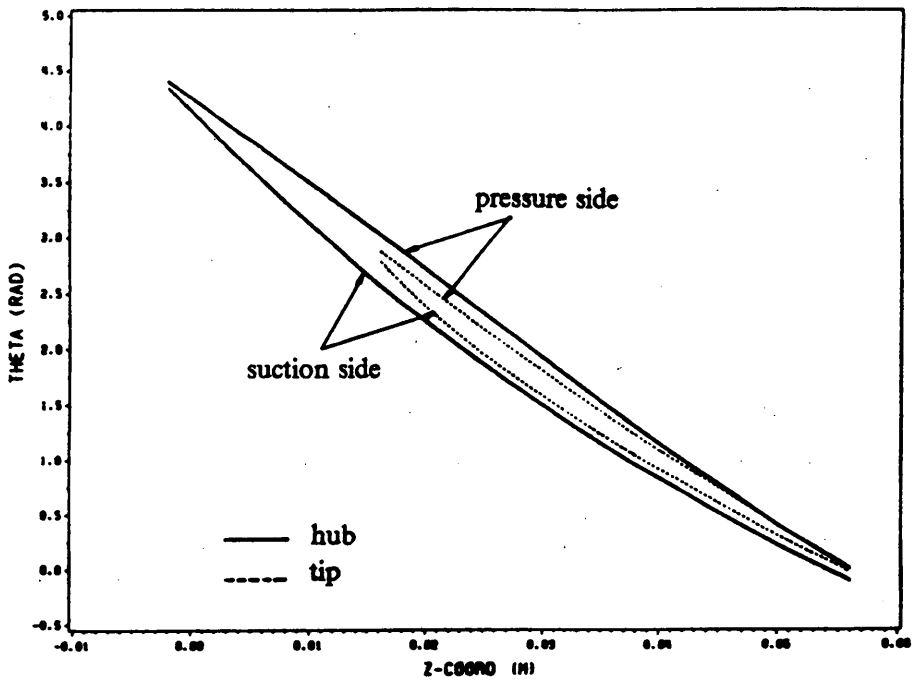


18b. Blade outline in meridional view.

Figure 18. Blade intermediate deformation process: Step-by-step description in meridional views of pressure side.



19a. Repartition of θ versus z .



19b. Repartition of θ versus z' .

Figure 19. Level of approximation of the method: θ versus z and z' distributions.

4.1.2.2 Definition of the grid in (r, θ, z') coordinate system.

The iterative procedure involved uses linear interpolation techniques to generate a 3-D surface grid with $40 \times 2 \times 11$ points in the (r, θ, z') coordinate system. A 2-D "meridional" grid is first determined in the (r, z') plane. Then, an angle θ is calculated for each one of the grid points. The main steps of the algorithm are described below:

- Specification of the blade outline in (r, θ, z') coordinates.
- Initialization of the surface grid points on both sides of the blade:
 - consider straight lines defined between corresponding (with same index number, as shown in Figure 20a) hub and tip points;
 - consider now 10 segments on each straight line. The relative length of each segment is obtained by linear interpolation between the two corresponding segments at the leading edge and at the trailing edge. l, m and n are the relative lengths for each segment shown in Figure 20b, with $m = l + (n - l) \times (i - 1) / 39$.

This procedure determines 9 points on each straight line. We have now 40×11 points defined over the blade in meridional plane.

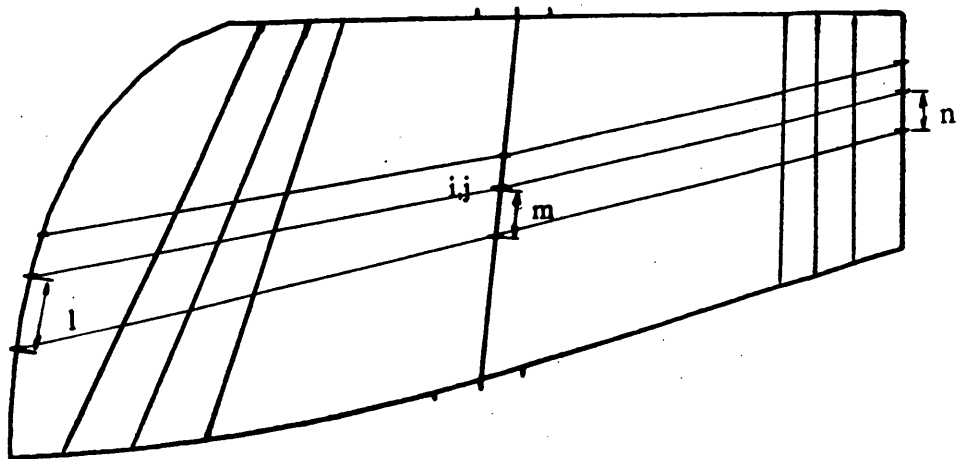
- Iterative procedure to refine the initial 2-D grid:
 - consider one current point and its four immediate neighbors, as shown in Figure 20b;
 - consider the j -direction ($i = \text{constant}$). In this direction, the total length of the current line from hub to tip is evaluated. Then, the relative lengths a' and b' are also calculated. The quantity a' is compared with the value found by linear interpolation between the corresponding leading edge and trailing edge segments. If a' is smaller than the expected relative length of the current segment, the current point is moved along b' ; if it is larger, the point is moved along a' .
 - The same procedure is then applied in the i -direction ($j = \text{constant}$).
 - This procedure is applied for each grid point.

The procedure was iterated 10 times over the whole grid.

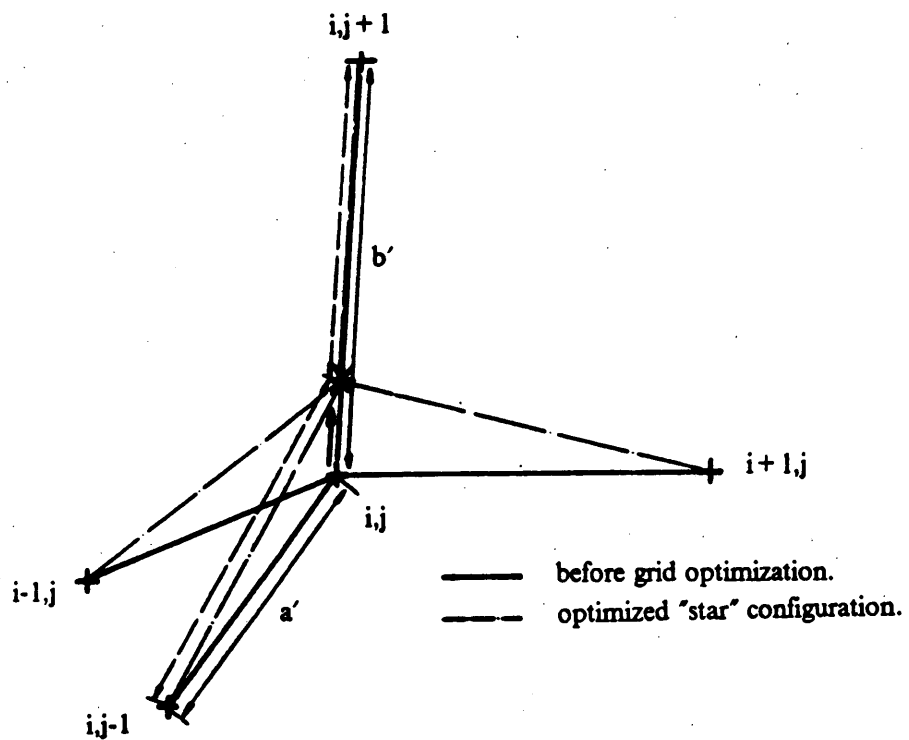
- Determination of a θ coordinate for each one of the 2-D mesh points.
 - Knowing r and z' , linear interpolation between hub and tip, along a line of constant z' , is used on both sides of the blade.

4.1.2.3 *Final blade grid definition.*

The final definition of the 3-D grid of the blade is derived from the previous results by applying the inverse transformation F^{-1} from the (r, θ, z') coordinate system to the (r, θ, z) coordinate system. The final result is illustrated in Figure 21.



20a. Procedure to initialize the inner points in (r, z') plane.



20b. Unit procedure to optimize the grid in (r, z') plane.

Figure 20. Grid definition process on the intermediate blade outline: Notations and elementary scheme.

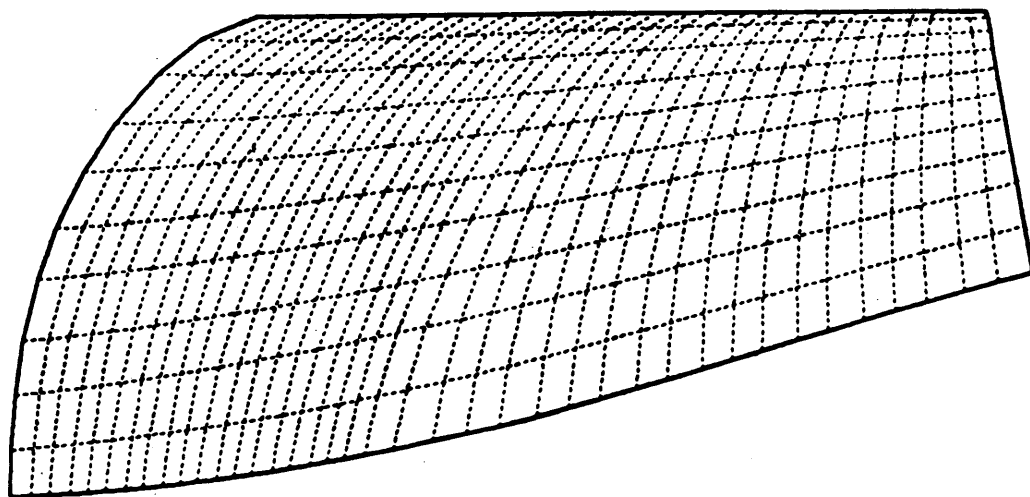
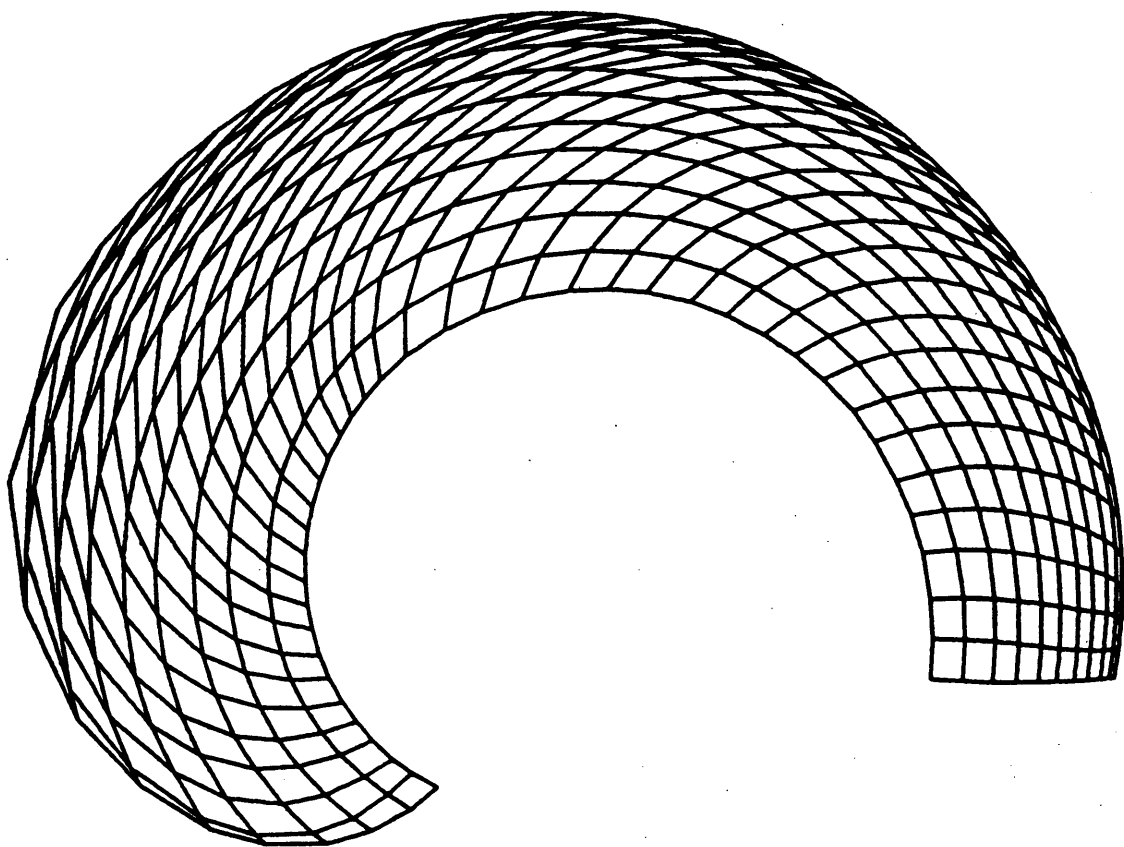


Figure 21. Final grid definition on one blade: Meridional and axial views.

4.2 Introduction to GEOMI: a tool to manipulate grids.

Prior to the first calculations, the basic 3-D grid defined previously has to be converted into a specific format compatible with the MEFP code. Some more points must also be added. It is the purpose of the following sections to underline the main steps of the manipulations that have been done, starting with the BASIC BLADE GRID and producing the MASTER GEOMETRY GRID.

This grid definition process used a software package called GEOMI which is associated with the flow calculation program MEFP. The main features of GEOMI are presented in Appendix A. We have essentially used the linear and circular arc interpolation, the line deletion and the graphical viewing functions.

GEOMI requires the input or "source" grid to be in the same format as used by MEFP (see Appendix A). In summary, a new double indexation is added to each grid point in either rectangular or cylindrical coordinate system representation. The first one accounts for the physical nature of the point: stationary wall point, rotating wall point, flow point or inner solid point. The second indexation is related to the application of GEOMI functions and defines a new 3-D representation of the grid with $A(i)$, $B(j)$, $C(k)$ as relative reference locations as sketched in Figure 22.

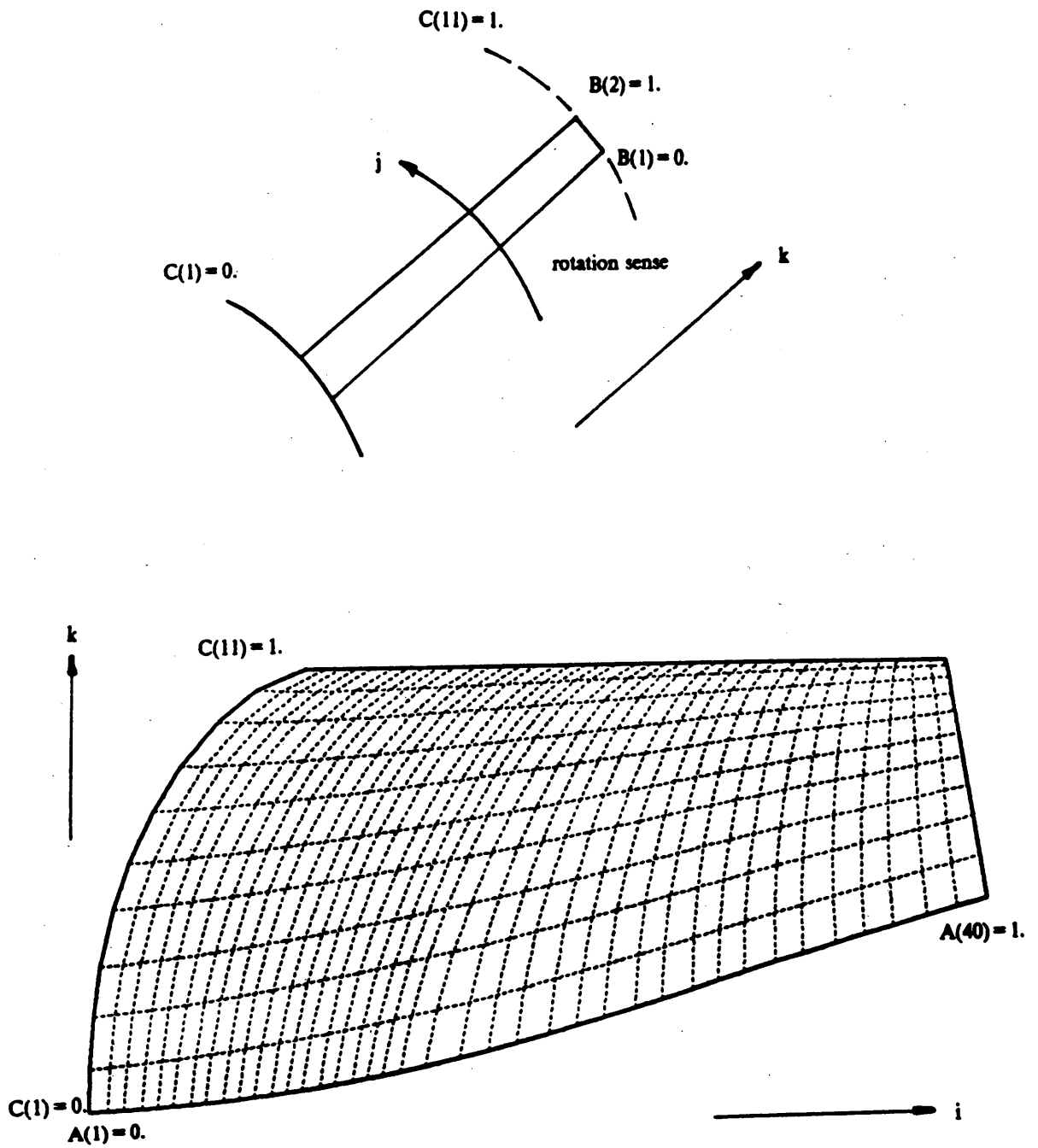


Figure 22. GEOMI format grid indices: Meridional and axial views.

4.3 Completion of the Basic Blade Grid.

Until now, the BASIC BLADE GRID represents only the reference blade surface. We must complete this grid with the definition of the flow-field around the blade.

4.3.1 The tip gap definition.

Two cylindrical surfaces have been defined: one represents the shroud and the other one corresponds to the mid-height of the tip gap, midway between the blade tip and the shroud. As specified by S.E.P., the tip gap width is 0.5 mm. This is about 1% of the passage section height at the inlet of the first blade row. A meridional view of the basic geometrical definition of the tip gap is shown in Figure 23a.

4.3.2 The tangential repeating boundaries definition.

Only one among the four blades of the inducer first row has been considered yet. The other blades are deduced from the reference blade by their simple symmetric arrangement.

In order to perform any computational work, we need to close the flow-field studied. The hub and the shroud already define two natural radial boundary surfaces. The axial boundaries are specified later. Due to the geometrical symmetry, two boundaries are defined as the middle surfaces in the blade-to-blade passages on each side of the reference blade. In an axial view, they make an angle of 90 degrees. These surfaces are called "repeating boundaries". Figure 23b sketches their location relative to the blade in an axial view.

4.3.3 The axial boundaries definition.

The elliptic nature of the flow requires that special care be accorded to the upstream and downstream conditions relative to the blade. The calculation grid will be extended far enough in front of and behind the blade, including the upstream nose and the

downstream cross section decrease, but without the second blade row, to assure parabolic flow.

4.3.3.1 Upstream conditions: the spinner definition.

As sketched on the general representation of the inducer in Figure 2, the LH₂ helical inducer begins with a surface of revolution, the spinner, designed to deflect the flow into the blade passages.

The rotation and the shape of this element influences the flow configuration at the inlet of the blade row. In order to take this element into account in our calculations as well as to define acceptable upstream conditions, the basic grid is first extended by approximately two spinner lengths upstream of the blade leading edge location where $z=0$.

The geometric definition of the spinner has been made with 5 surface points in a meridional representation of the inducer. Further refinements of the spinner definition are introduced later with GEOMI circular arc interpolation. The corresponding points in the flow-field and at the shroud, with same axial index, have been chosen arbitrarily to define a fairly smooth grid.

In order to make this upstream grid match with the blade definition, several manipulations were necessary:

- linear interpolation in meridional plane with GEOMI to obtain 13 lines from hub to shroud, consistent with those defining the BASIC BLADE GRID;
- definition of 5 radial surfaces matching with: the two repeating boundaries, the two sides of the blade and the inner mean blade surface.

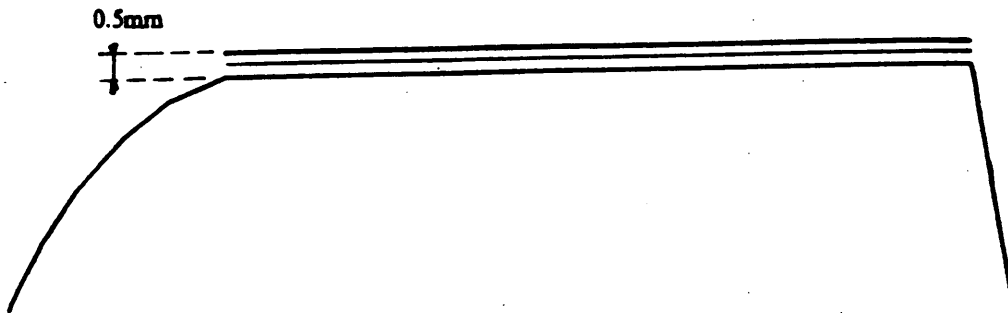
Moreover, this upstream grid has to be "bent" to account for the blade camber at the leading edge and avoid any sharp angle in the calculation grid at the interface with the blade grid. A mean value of $\delta\theta/\delta z$ is calculated along the leading edge and this slope is kept constant over the whole upstream grid (cf. Figure 24).

4.3.3.2 Downstream conditions: the hub definition.

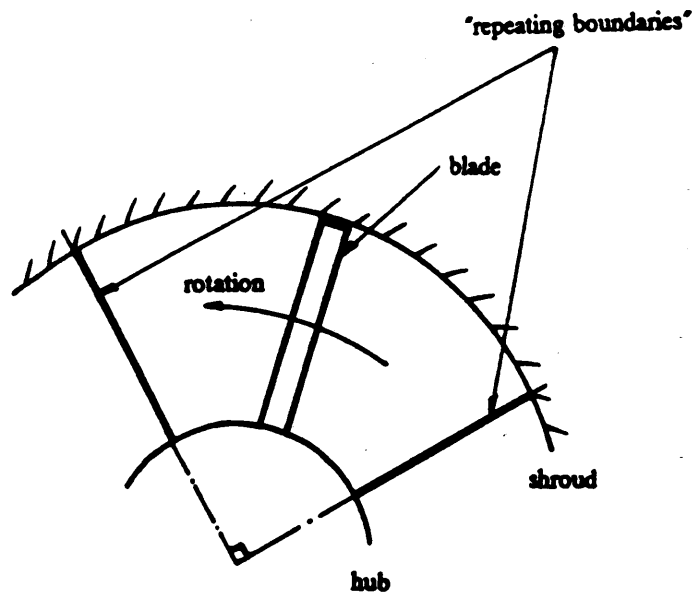
The air tests show that the angular position of the second inducer blade row relative to the first one has no significant influence on the flow pattern between the two rows. However, one cannot deduce from this observation that accurate calculations can be performed for the first row only without accounting for the downstream conditions.

Since we do not want to include the second blade row in our study, we will only consider the decrease of the throughflow passage downstream the first blade row due to the hub enlargement shown in Figure 2 for example. So far, the calculation grid has been extended by approximately one half of the blade chord downstream, with no blade in the passage.

The numerical definition of the downstream grid is exactly similar to the one performed for the upstream grid. Noticing that the extension chosen leads to the end of the second blade row, we have taken 10 points regularly spaced out of S.E.P.'s definition of the hub downstream of the blade trailing edge. Linear interpolation and grid manipulation with GEOMI as well as some additional computer processing (to account for the blade camber at the trailing edge like for the upstream grid, for example) produce a final basic downstream grid matching with the blade grid.



22a. Tip gap definition in meridional representation



22b. Circumferential repeating boundaries in symbolic axial section.

Figure 23. Definition of the flowfield boundaries: r -, θ - and z -direction.

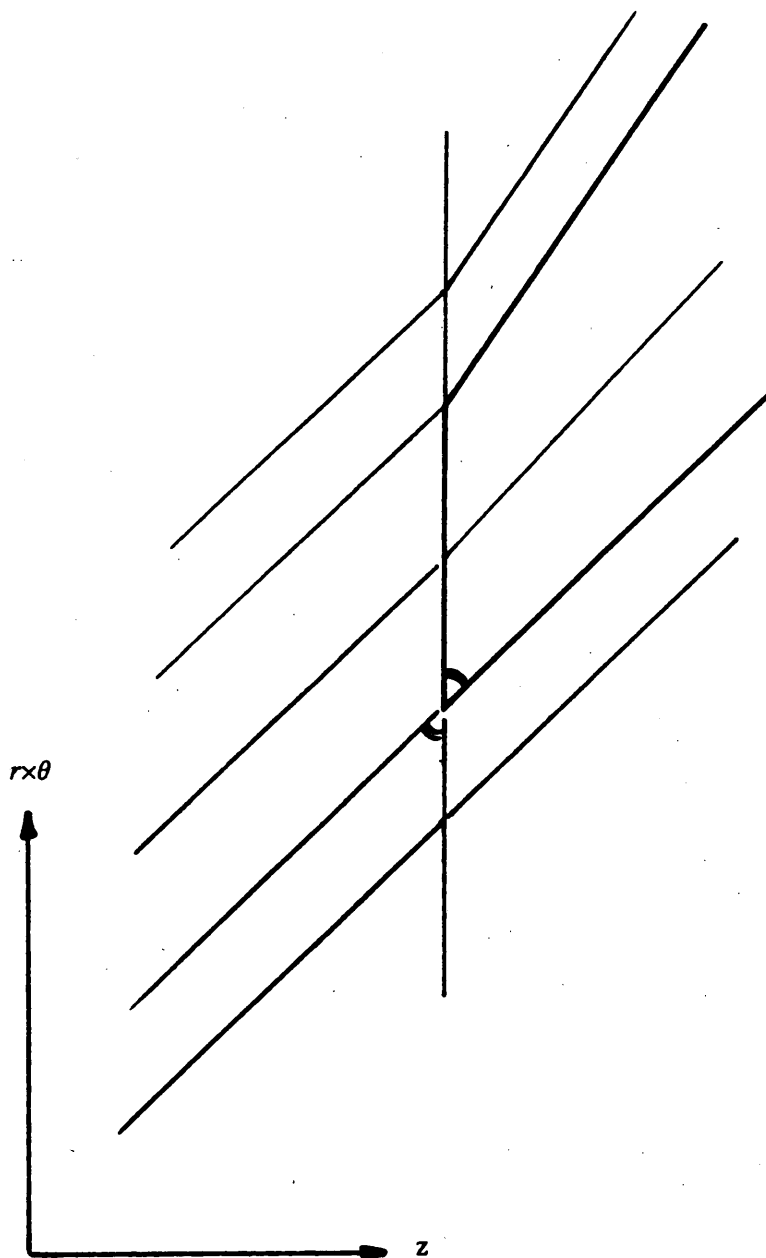


Figure 24. Effect of camber at the leading edge for the upstream grid: blade-to-blade view.

4.3.4 The final BASIC GRID.

Assembling the three discretized domains described above: upstream zone, blade region and downstream zone, we have a first BASIC 3-D GRID in the calculation format (cf. Figures 25 and 26)

However, the present grid shows several poorly defined zones -e.g. near the walls- as well as "overdefined" zones, defined with too many points -e.g. the blade definition far from the ends. For these reasons, we will rationalize and homogenize the BASIC GRID, that is: to correlate it with the physical behavior of the flow, refining the critical zones where complicated phenomena occur or relaxing the grid where the flow is more uniform. The 3-D grid resulting from this process will be called: MASTER GEOMETRY GRID, and will be in a final input form for the MEFP code.

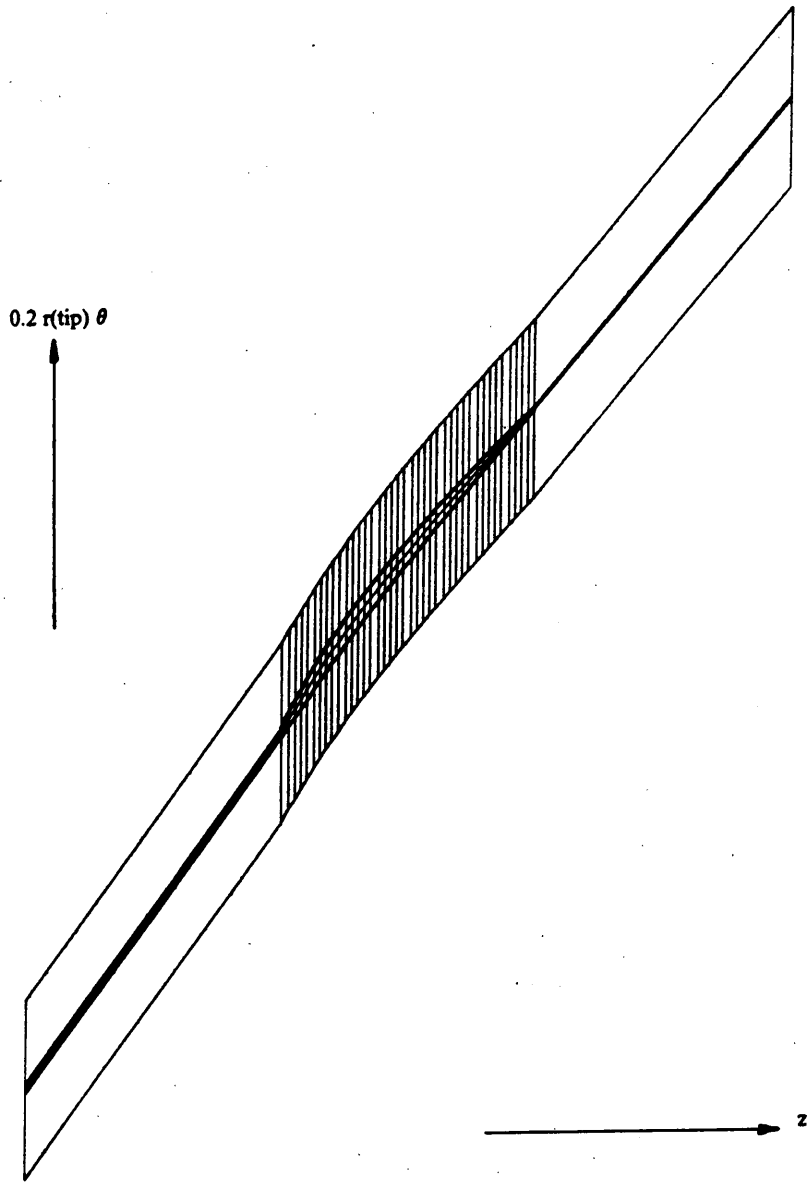


Figure 25. FINAL BASIC GRID: blade-to-blade view.

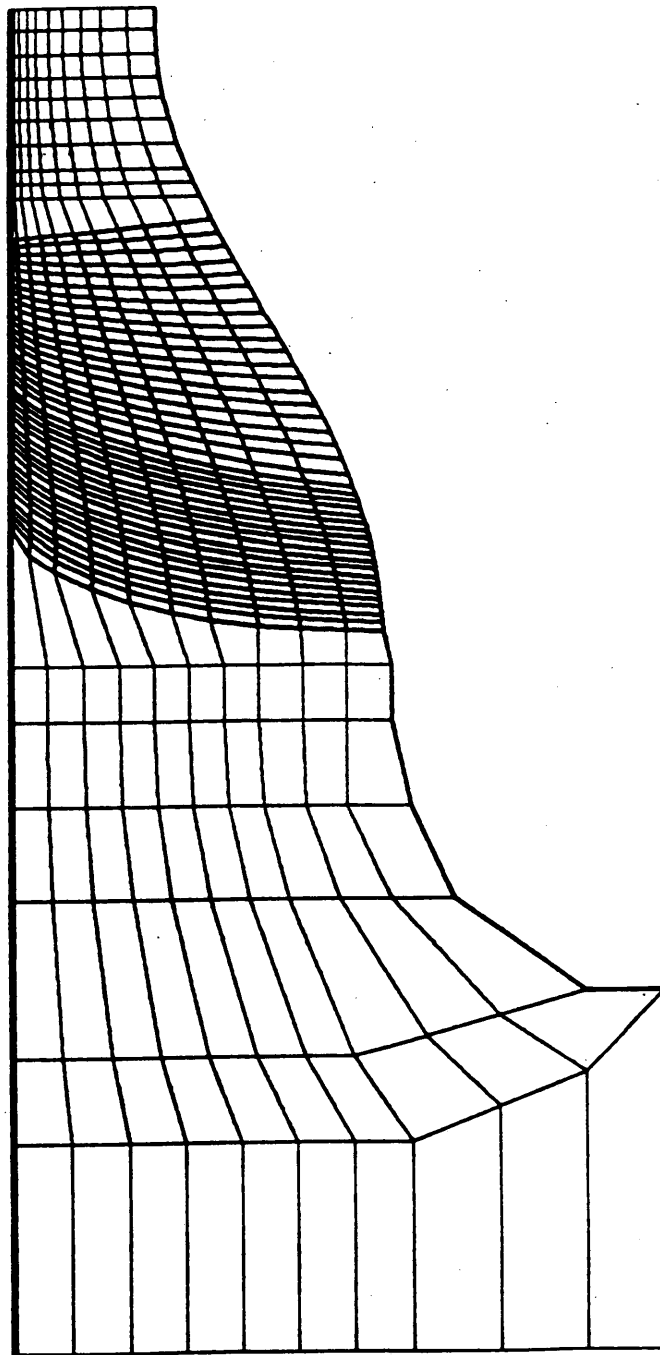


Figure 26. FINAL BASIC GRID: meridional view.

4.4 Preliminary two-dimensional calculations.

The 2-D calculations performed were driven by three main objectives. The first one was to provide a physical insight of the flow pattern around the blade and to locate the regions where the BASIC GRID had to be improved. The second one concerned the definition of the boundary conditions and the optimization of the calculation grid size in order to obtain a satisfactory compromise between computation time and level of resolution in the 3-D calculation. Finally, a critical point was to show that the MEFP code could handle the high stagger angle and reproduce the expected physical phenomena, such as cavitation in the leading edge region (blade-to-blade calculation).

Three main target criteria were set for the grid spacing selection in the cases described below: 1- approximately equal distances around grid corners; 2- fairly uniform spacing in free stream; 3- grid spacing reduction factor of 2 or 3 near the walls for better resolution of the physical phenomena (boundary layer, cavitation, ...). For each flow calculation series, the details of the grid spacing are reported in Appendix B.

Technically, in this section, all grid point generation or deletion has been performed with GEOMI.

4.4.1 The blade-to-blade calculation.

The projection of the 3-D basic grid is made in the blade-to-blade plane corresponding to the tip section, that is: in an $(r(\text{tip}) \times \theta, z)$ representation, as shown in Figure 25.

The upstream and downstream boundaries have been arbitrarily chosen to be approximately one blade axial chord away from the leading edge and the trailing edge respectively. The upstream conditions correspond to the operating conditions of the prototype of the inducer tested in air (reference 26) and are specified in Appendix B.

From the results obtained in the series of tests performed and correlated with our intuitive expectations, we noticed that:

- The leading edge region is the most critical one of the flow-field because of the large pressure gradients and velocity deflections produced. Several tests were necessary to finally establish a grid definition around the leading edge with enough accuracy to re-

produce the velocity and pressure behaviors expected from experimental data. For example, we had to refine the basic grid far enough upstream of the leading edge to avoid numerical flow deflection at the inlet due to poor gridding, and close enough to the blade surface around the leading edge to show the low pressures on the suction side that would provoke cavitation with LH₂ (cf. Figure 30).

- The main part of the blade sides, sufficiently far from the ends, experiences less rapid flow changes. This allowed us a significant grid relaxation far from the ends, keeping finally only 14 of the former 40 sections on the blade in the axial direction.

- At the trailing edge, no specific problem was expected. By symmetry, the same grid pattern as for the leading edge was reproduced.

The final blade-to-blade 2-D calculation grid size is specified in Appendix B, along with the general calculation conditions. Figure 27 shows the repeated grid with three blades. The definition of the I-lines "along the blades" produces a very distorted gridding of the flow field but allows the code to handle the high stagger angle without any major difficulty during the runs. The boundary layer growth is visible in the total pressure loss contours plot (Figure 28b), whereas Figure 28a shows the static pressure gradient in the blade passages. The general velocity distribution is represented in Figure 29.

Cavitation inception at the leading edge

In cavitating rocket pump inducers operating in liquid hydrogen, cavitation inception occurs in the leading edge zone, where geometric angles provoke a sharp decrease in static pressure which, added to multiple other complicated and interactive phenomena (see Section 2), can start the growth of vapor bubbles or cavities. This two-phase flow phenomenon cannot happen in air conditions. However, it is interesting to investigate the regions where we can calculate low static pressures in the air simulation that correspond to values below the vapor pressure in liquid hydrogen.

A very simplified criterion for "eventual cavitation inception" is defined. It is based on the assumption that cavitation will occur in liquid hydrogen in the regions where the static pressure is inferior to the vapor pressure. An air-LH₂ analogy presented in Appendix B defines a critical value of the static pressure coefficient, $\psi_s = (p_s - P_0) / (.5 \rho_{air} U_{tip}^2)$. In the air pump, a value of $\psi_s = -0.048$ is equivalent to $p_s = p_{sat}$ in the LH₂ pump. Figure 30 represents the velocity vectors deflection at the leading edge, and the contour $\psi_s = -0.05$ visible on the suction side, showing a zone where cavitation inception is likely to occur.



Figure 27. Blade-to-blade calculation: repeated grid with three blades and actual angles.

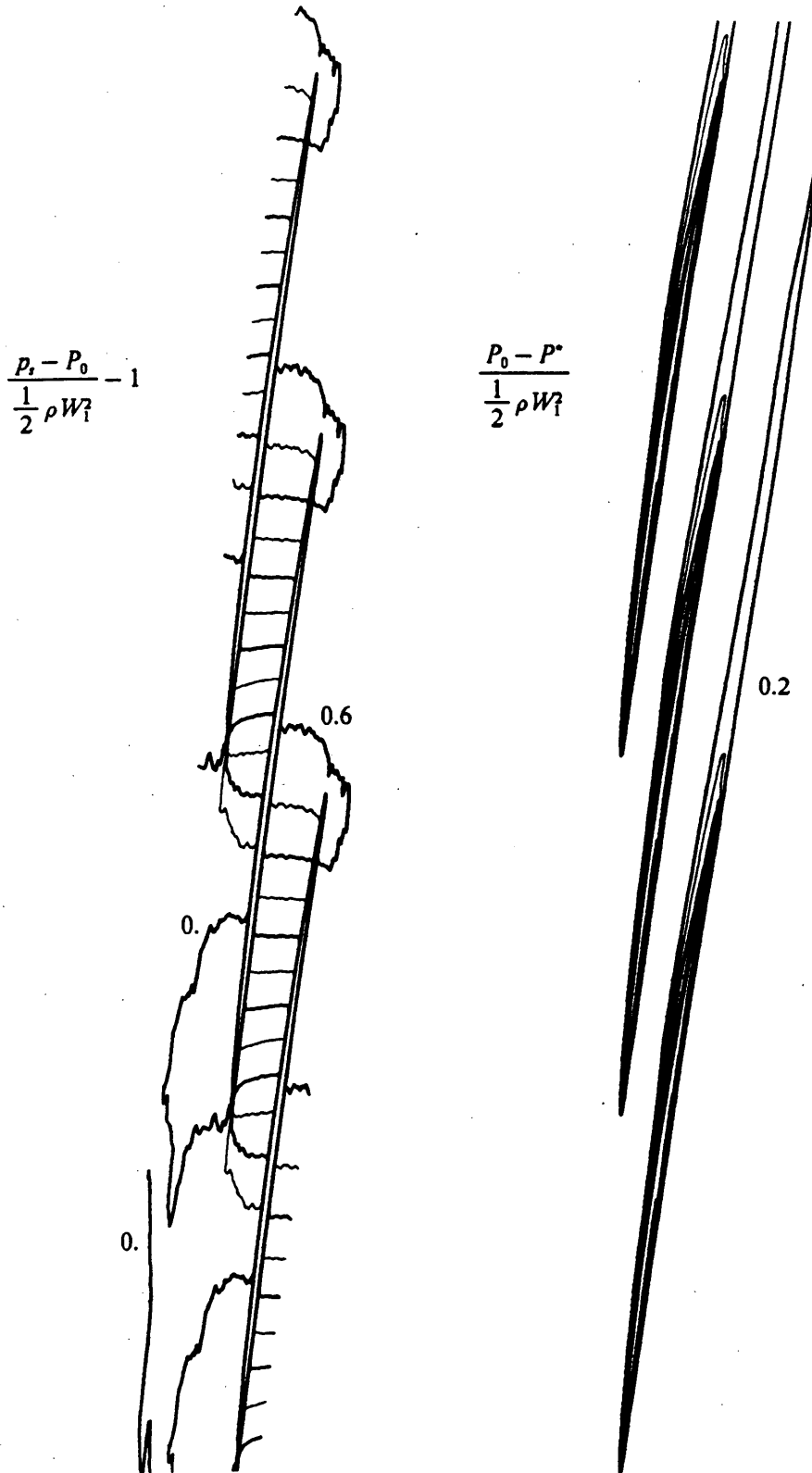


Figure 28. Blade-to-blade calculation: static pressure contours (from 0., by 0.05) and rotary stagnation pressure contours (from 0.2, by 0.1).

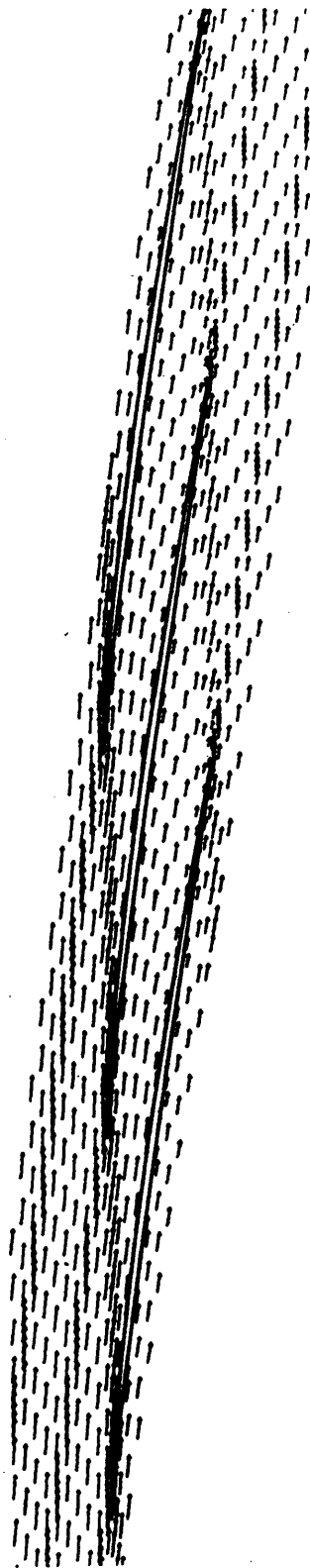


Figure 29. Blade-to-blade calculation: velocity vectors.

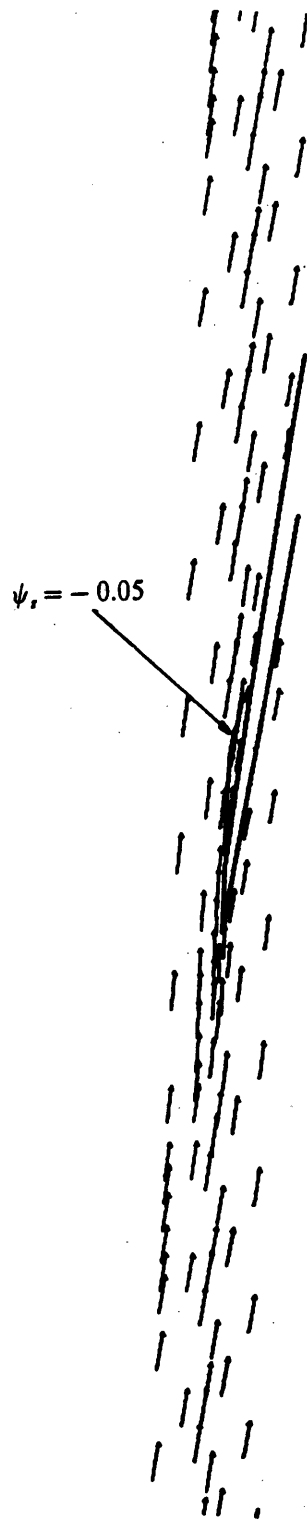


Figure 30. Blade-to-blade calculation: zoom of the leading edge; cavitation inception zone.

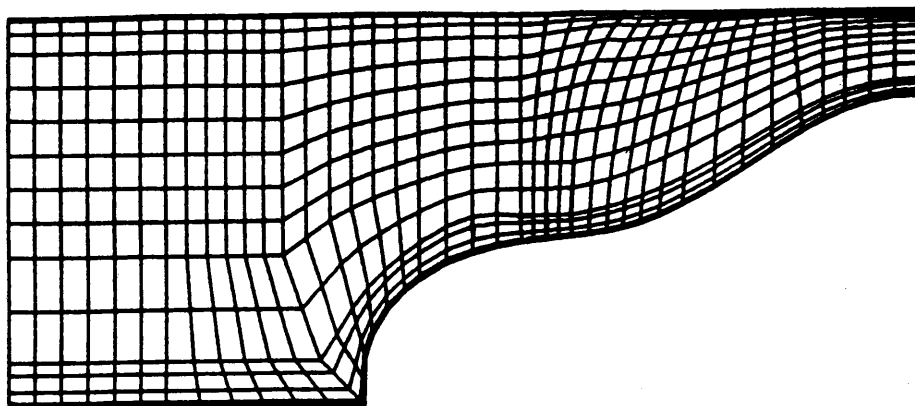
4.4.2 The meridional calculation.

Whereas the objective of the previous section was to specify the flow behavior around the blade, we now want to look at the influence of the upstream and downstream conditions including the hub and shroud wall effects. A 2-D meridional grid has been defined from the basic grid and a series of calculations has been performed to refine and validate a final 2-D meridional calculation grid.

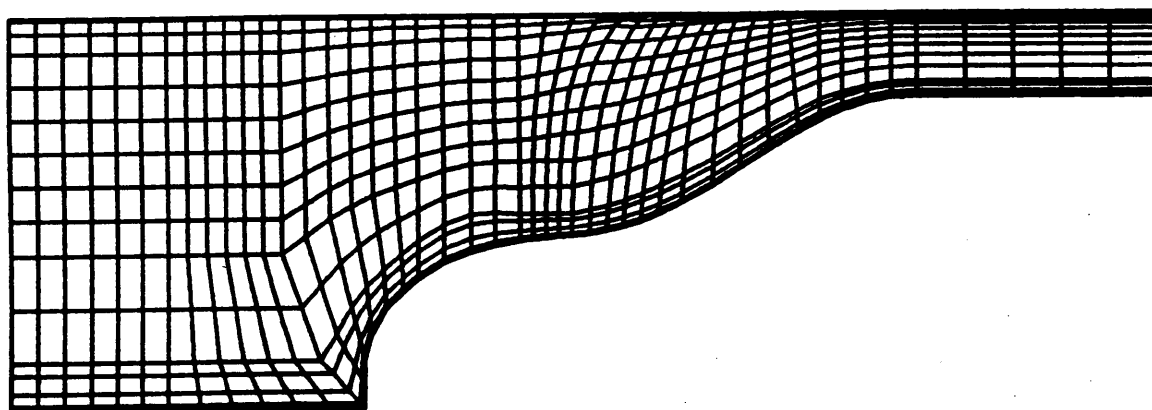
The boundary layer growth along the walls has been accounted for. The inlet velocity profile has been deduced from a $1/7$ th power law, assuming a turbulent, fully developed duct flow at the inlet plane of the grid, upstream the spinner (see Appendix B).

A relaxation of the grid in the blade region has been permitted since the blade is not present in these calculations and since we are only interested in the boundary conditions definition.

Two series of runs were needed in order to locate an I-plane downstream the blade trailing edge where the static pressure is almost uniform over the passage height. The two grid configurations are shown in Figure 31 and the calculation results are presented in Figures 32 to 34. A comparison of the static pressure coefficients in Figure 32 shows the influence of the grid extension downstream the blade trailing edge. The region of influence of the downstream annulus geometry is confined to the outer radii about one blade height downstream of the location of the blade trailing edge. There is no noticeable influence in the region of the trailing edge. However, we can already notice that the region where this influence is visible corresponds to the location of the actual inducer second blade row. The presence of this second blade row has not been taken into account in our inducer flow calculations. The velocity vectors and total pressure losses plots (Figures 33 and 34) show well the boundary layer growth at the shroud and at the rotating hub.



31a. First series of meridional calculations: $I \times J \times K = 42 \times 2 \times 19$

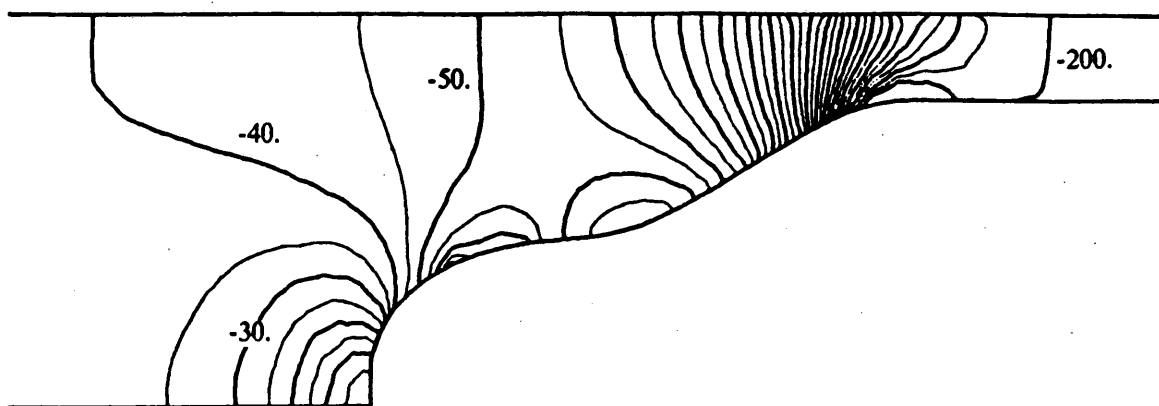


31b. Second series of meridional calculations: $I \times J \times K = 47 \times 2 \times 19$

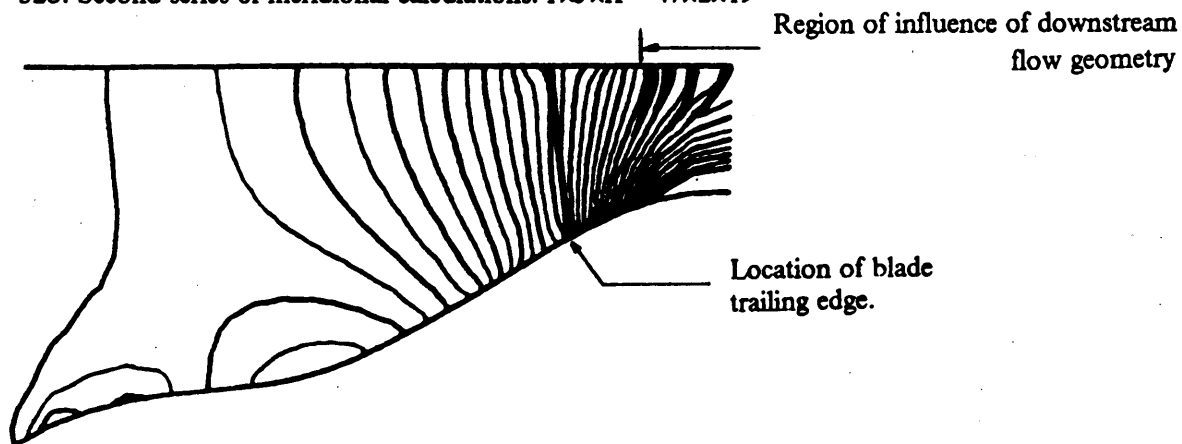
Figure 31. Meridional calculation: comparison between the two grids tested.



32a. First series of meridional calculations: $I \times J \times K = 42 \times 2 \times 19$



32b. Second series of meridional calculations: $I \times J \times K = 47 \times 2 \times 19$



32c. Comparison (dark lines at exit correspond to contours shown in 32b).

Figure 32. Meridional calculation: static pressure distribution, $p_r - P_0(Pa)$; comparative study.

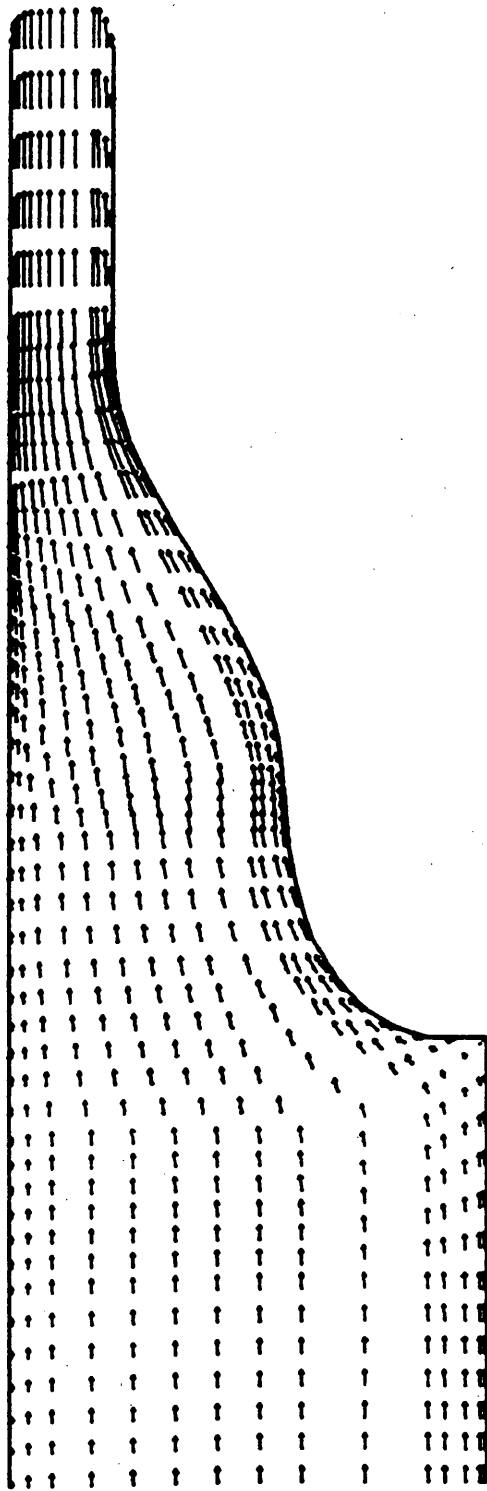


Figure 33. Meridional calculation: velocity vectors.



Figure 34. Meridional calculation: total pressure loss distribution, $P_0 - P^*(Pa)$.

4.4.3 Choice of the 3-D CALCULATION GRID.

The 2-D calculations have permitted to create two "2-D master geometry grids". The first one has specified the definition of the grid around the blade surface, whereas the second was useful to establish proper boundary conditions and the upstream and downstream extents of the grid. Combining these preliminary results (see Appendix B), we can now define the final MASTER GEOMETRY GRID that will be used for the 3-D computations.

The grid spacing retained is finally: $I \times J \times K = 38 \times 17 \times 19$.

The inlet velocity conditions account for the turbulent, fully developed duct flow assumption as well as for the flow incidence angle of 3 degrees specified by SEP.

Figure 35 shows a quasi-axial ($i = \text{constant}$) view of the 3-D grid immediately after the leading edge, and Figure 36 gives a meridional representation.

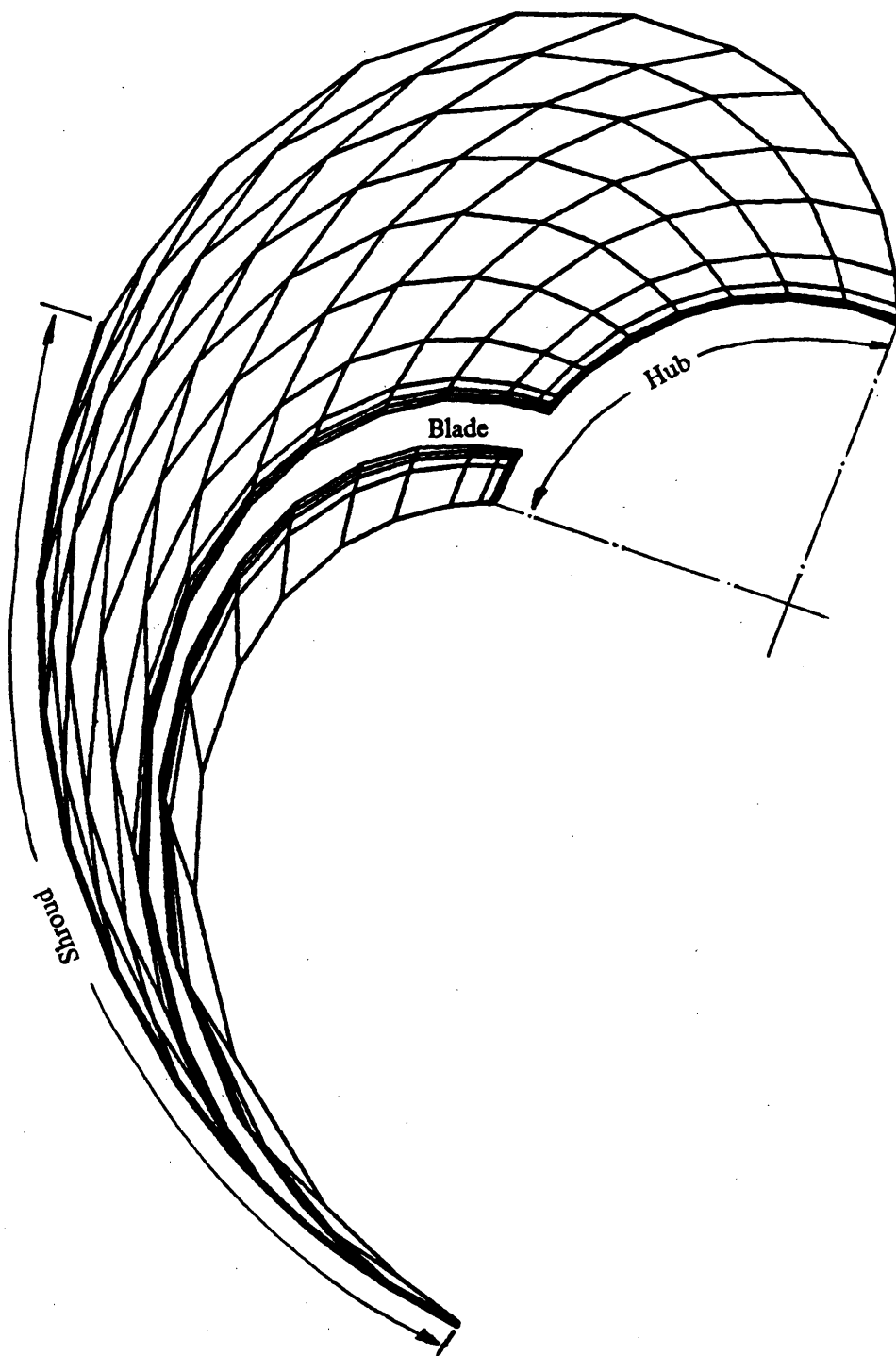


Figure 35. Master geometry grid: iso-I plane view immediately after the leading edge.

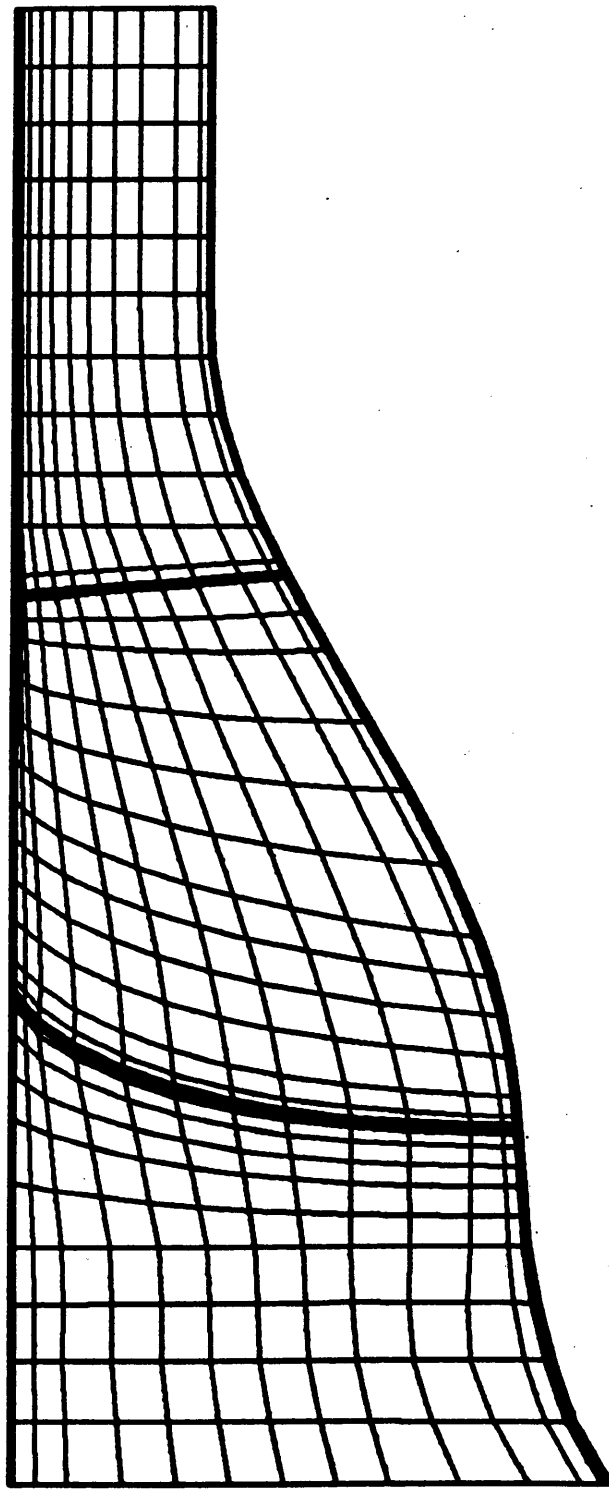


Figure 36. Master geometry grid: meridional view.

5.0 RESULTS OF THE 3-D FLOW CALCULATION.

5.1 *3-D Flow Calculation Details.*

The 3-D flow calculation was run for 70 iterations. The first 24 passes were run over a coarse grid ($I \times J \times K = 26 \times 11 \times 14$, that is: 4004 points) in order to accelerate the convergence of the elliptic flow procedure prior to finer computations. The following 46 iterations were conducted over the complete Master Geometry Grid ($I \times J \times K = 38 \times 17 \times 19$, that is: 12,274 points).

It required about 5 1/2 hours of CPU time on the IBM 3084 available at VPI&SU, and used about 4 Megabytes of memory space.

In order to obtain a reasonable compromise between the cost in CPU time and the level of accuracy expected from the flow calculation, it was decided to stop the computations when the negative mass flow rate calculated had reached a stabilized value. Then, all backflow phenomena, such as recirculation or vortices, were considered fully developed in the numerical simulation.

5.2 Thermodynamic Analysis of the Flow.

In this Section, it is intended to define two important parameters that are used in the following discussion. The first one is the Rotary Stagnation Pressure, P^* , and the second one is the Hydraulic Efficiency, η .

5.2.1 Euler work.

The Euler turbine equation (1) relates the fluid flow to the work done, or energy transfer, in a turbomachine and can be derived as follows (from reference 37). Consider the control volume as shown in Figure 37a, enclosing an axial-flow compressor for example. The torque of the rotor acting on the fluid can be found from the moment of momentum equation:

$$T = \iint (\mathbf{r} \times \mathbf{V})(\rho \mathbf{V} \cdot d\mathbf{A})$$

but $\rho \mathbf{V} \cdot d\mathbf{A} = dm$ and with the assumption of uniform flow at the inlet and exit stations, we can write:

$$T = \dot{m}(r_2 V_{\theta 2} - r_1 V_{\theta 1}) z$$

Since the control volume is symmetrical, the pressure forces do not create any torque and, for the ideal flow case, there are no shear forces. Thus, the torque exerted is that on the flow by the shaft of the rotor. If the shaft and rotor have a rotational speed ω , the energy transfer from the rotor to the fluid is given by:

$$P = \dot{m}w = \omega T$$

The Euler work per unit mass flow is given by:

$$w = \omega(r_2 V_{\theta 2} - r_1 V_{\theta 1})$$

But the blade speed at radius r is:

$$U = r\omega$$

Therefore,

$$w = U_2 V_{\theta 2} - U_1 V_{\theta 1} \quad (5.1)$$

V_{θ} is taken positive in the direction of the blade velocity U . Work is positive when there is a transfer from the rotor to the fluid.

5.2.2 Losses and efficiency.

For an incompressible ideal flow -that is: the fluid leaves at the blade exit angle and the work is done reversibly-, the total pressure change is related to the work done by the relation:

$$w = \frac{\Delta P_{te}}{\rho}$$

For a fluid with no prewhirl, $V_{\theta 1} = 0$, we find:

$$\Delta P_{te} = (P_{t2} - P_{t1})_{te} = \rho U_2 V_{\theta 2}$$

Consider now the velocity triangle sketched in Figure 37b:

$$\begin{aligned} &= V^2 - V_{\theta}^2 \\ V_m^2 &= W^2 - (U - V_{\theta})^2 \\ &= W^2 - U^2 + 2UV_{\theta} - V_{\theta}^2 \end{aligned}$$

Thus:

$$UV_{\theta} = \frac{1}{2}(V^2 + U^2 - W^2)$$

And:

$$\Delta P_{te} = \frac{\rho}{2}(V_2^2 + U_2^2 - W_2^2)$$

But we have also:

$$(P_{r2} - P_{r1})_{ie} = P_{s2} + \frac{1}{2} V_2^2 - P_{r1}$$

Combining these two relations, we find in the ideal case:

$$P^* = P_{s2} + \frac{1}{2} \rho W_2^2 - \frac{1}{2} \rho \omega^2 r_2^2 = P_{r1} \quad (5.2)$$

In actual cases, however, one must account for total pressure losses in the compressor. These can be caused by viscosity, compressibility (small), 3D, secondary flow, non-uniformity or other off-design effects that will be discussed later (more generally, the entropy variation in this case is caused by friction and mixing of streams with different properties). We can express them as follows:

$$(\Delta P_t)_{actual} < (\Delta P_t)_{ie}$$

$$P_{r2} < (P_{r2})_{ie}$$

$$P^* < P_{r1}$$

And finally, the total pressure loss in the compressor stage can be represented by the difference :

$$(P_{r1} - P^*) = \text{total pressure loss} \quad (5.3)$$

The definition of the efficiency for a turbomachine can be thought of as:

$$\eta = 1 - \frac{\text{losses}}{\text{work done}}$$

The losses are represented by $\frac{(P_{r1} - P^*)}{\rho}$, and the usual hydraulic efficiency would be defined in this case by:

$$\eta_{hydraulic} = 1 - \frac{P_{r1} - P^*}{\rho \omega r V_\theta} \quad (5.4)$$

This formulation involves the value $\omega r V_\theta$ of the local work (averaged value) done by the fluid enclosed in the "thin" streamsheet at radius r at the exit station.

NOTE: in our study, P_{r1} corresponds actually to $P_0 = 101,325$ Pa.

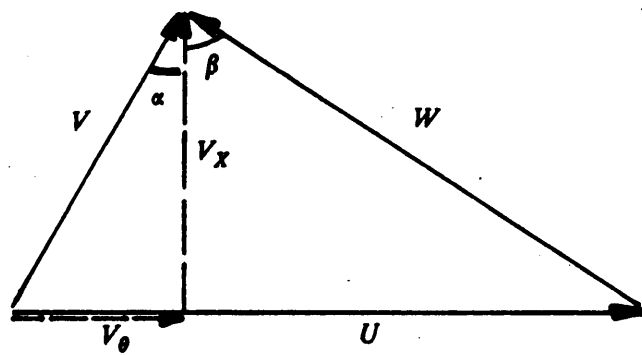
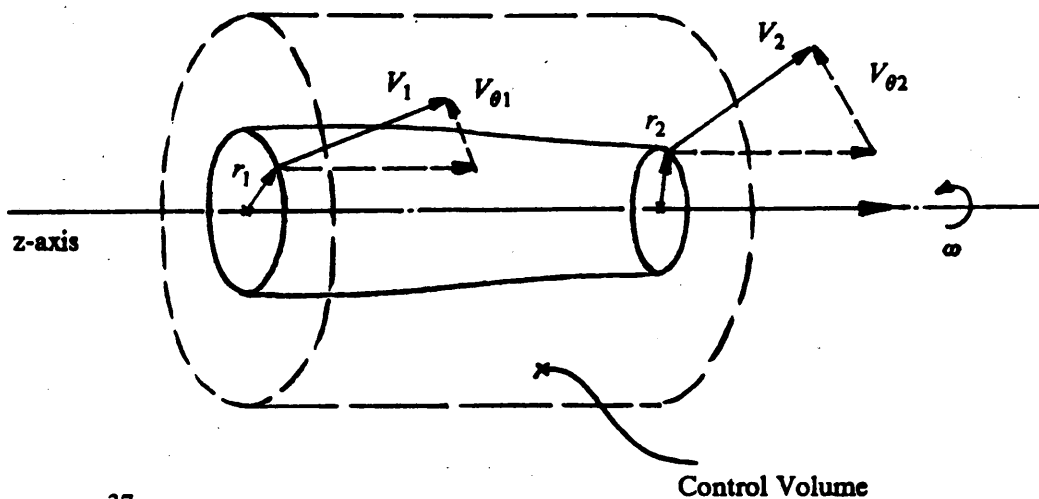


Figure 37. Thermodynamic analysis of the flow: control volume definition and velocity triangles.

5.3 *Blade-to-Blade and Meridional Analysis.*

Prior to any discussion of the results, the general notations adopted in the calculation are shown in the three dimensional sketch of an inducer blade in Figure 38 (see also Appendix A).

5.3.1 Velocity distribution.

Figure 39 represents the velocity vectors in three meridional views at mid-passage, near the suction side, and near the pressure side, showing the general trends of the primary flow and some secondary flows.

The velocity profiles at the inlet and exit stations show the boundary layer growth at the stationary shroud, where the absolute velocity goes to zero, and at the rotating hub where it equals the rotation speed of the wall.

Near the suction and pressure sides, relatively strong radial flows develop. These secondary flows will be discussed in more detail in the next section, but we can already notice that: 1- they grow continuously along the blade passage, being rapidly dominated by the primary flow downstream of the trailing edge; 2- they appear to exist over the entire passage height, with increasing amplitudes towards outer radii.

The expected tip leakage flow caused by the pressure drop from pressure to suction side is also visible on these plots through the large vectors shown in the tip gap on the near-pressure side meridional view. Figure 40 also illustrates this phenomenon in blade-to-blade views, for various passage heights within and below the tip gap. In this Figure, the velocity components normal to the blade in the tip gap are shown to be large all along the blade tip. However, they are significantly more important at the leading edge and extend relatively far upstream, revealing also some backflows.

Another important phenomenon can be observed in the meridional views in Figure 39: the presence of a distinct vortex immediately upstream of the leading edge, near the shroud. This vortex is confirmed in the meridional representations of the total pressure loss contours ($\psi_t = (P_0 - P^*) / (0.5\rho U_{tip}^2)$) in Figure 42. A concentration of contours appears in the vortex region as the blade pressure side is approached. In complementary views not shown here, starting 4% of pitch from the pressure side, a distinct closed

contour of $\psi_t = 0.4$ begins to form, with relative stabilization of its size until 2% of pitch from the suction side, that is, across the blade tip. After the suction side, this contour spreads across the blade passage, because of mixing and other convective 3-D flow effects. This circumferential vortex seems then to experience "intensity jumps" every time it is crossed by a blade, decaying continuously afterwards in the passage from the suction side.

The origin of this phenomenon can be found in the high flow stagger angle, $\beta = 85^\circ$ at the tip, and low flow coefficient, $\phi = 0.07$. As shown in Figure 41, the fluid flows over the swept leading edge towards lower pressures, from pressure side to suction side. This leakage is increased towards outer radii because of the blockage effect created by the shroud and the small size of the tip gap. (This blockage may also partially explain the backflows observed).

The direction of this secondary flow is between the normal to the blade surface and the primary flow direction. The fluid is then convected in the primary flow, with some mixing. Since the flow stagger angle is very high, and the flow coefficient very low, a part of this flow encounters the next blade before the beginning of its tip gap (the primary flow convection is not large enough compared to the rotation speed of the blades); the same leakage process is then re-experienced by the flow particles. After the tip gap, a vortex develops because the flow is first driven radially inwards, towards lower static pressures (from radial equilibrium in the momentum equation). It is convected in the primary flow and pulled outwards again by repeated tip leakage as the next blade arrives. The resulting path of the flow particles from blade to blade resembles the spiral sketched in Figure 41.

This circumferential vortex explains the backflows pointed out earlier in Figure 40. A more detailed discussion of the tip leakage flow is required to justify the larger tangential velocities observed in the leading edge region. This is considered in the next section.

The boundary layer growth at the shroud along the inducer passage is another very interesting characteristic of the flow that can be studied in Figures 38 and 42. By joining the beginning of each velocity vector plotted with the next with the same number in the radial k -direction, we obtain an acceptable approximation of the primary flow streamlines. But a comparison with the velocity vectors themselves shows then a distinct development of inward flow, from shroud to mid-height at mid-passage; after the trailing edge, the flow mixes and tends to rejoin the primary flow pattern. These radial velocity

components are coupled with an increase of the extent of the losses near the shroud (Figure 42) and characterize a shroud boundary layer growth with significant blockage starting near mid-chord. This boundary layer thickening was expected from Figure 7 and will be discussed in the next section, but the blockage effect and the radial deflection appeared to be surprisingly important. A study of the displacement thickness would characterize quantitatively this phenomenon of primary importance in the design of the inducer.

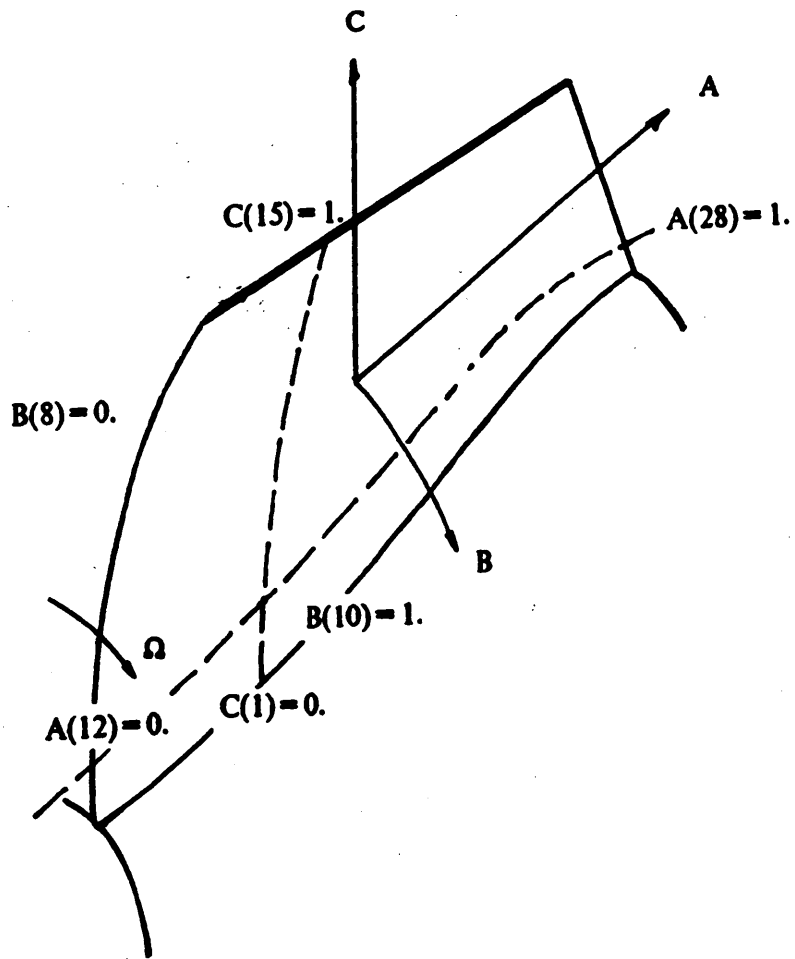


Figure 38. Notations used in the 3-D calculation.

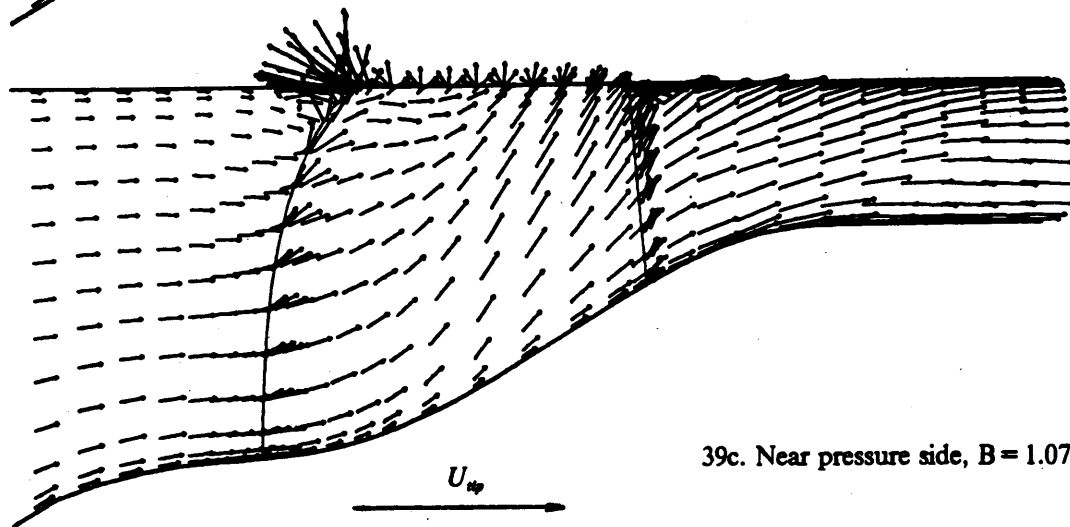
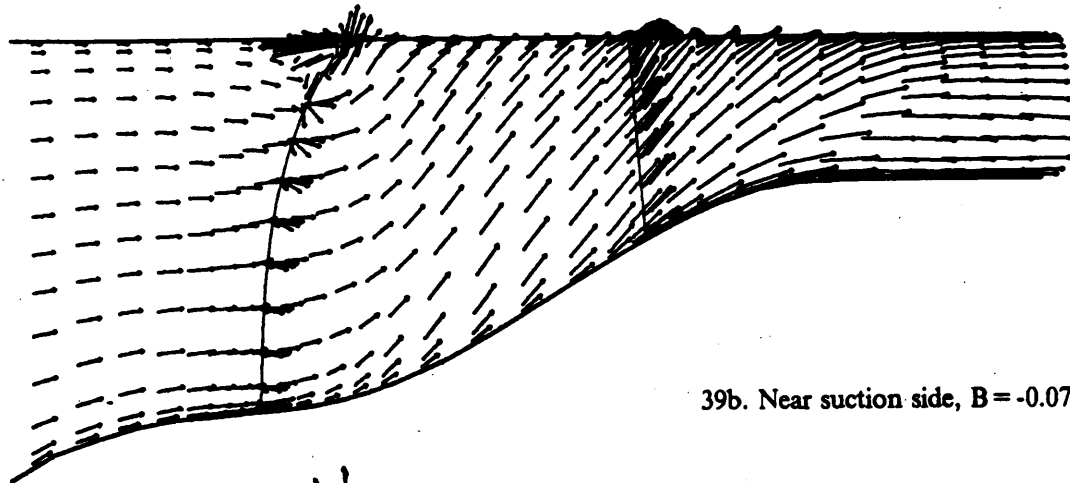
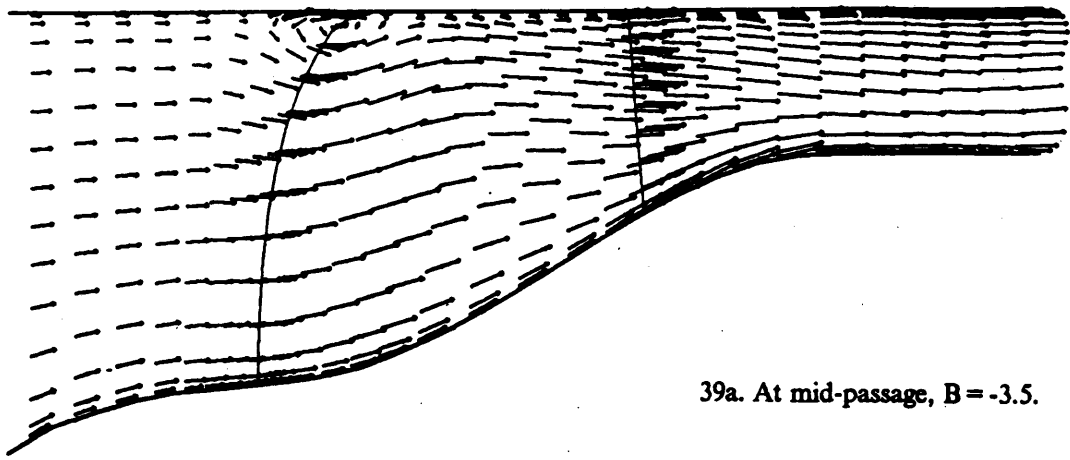


Figure 39. Meridional views from the 3-D calculation results: velocity vectors.

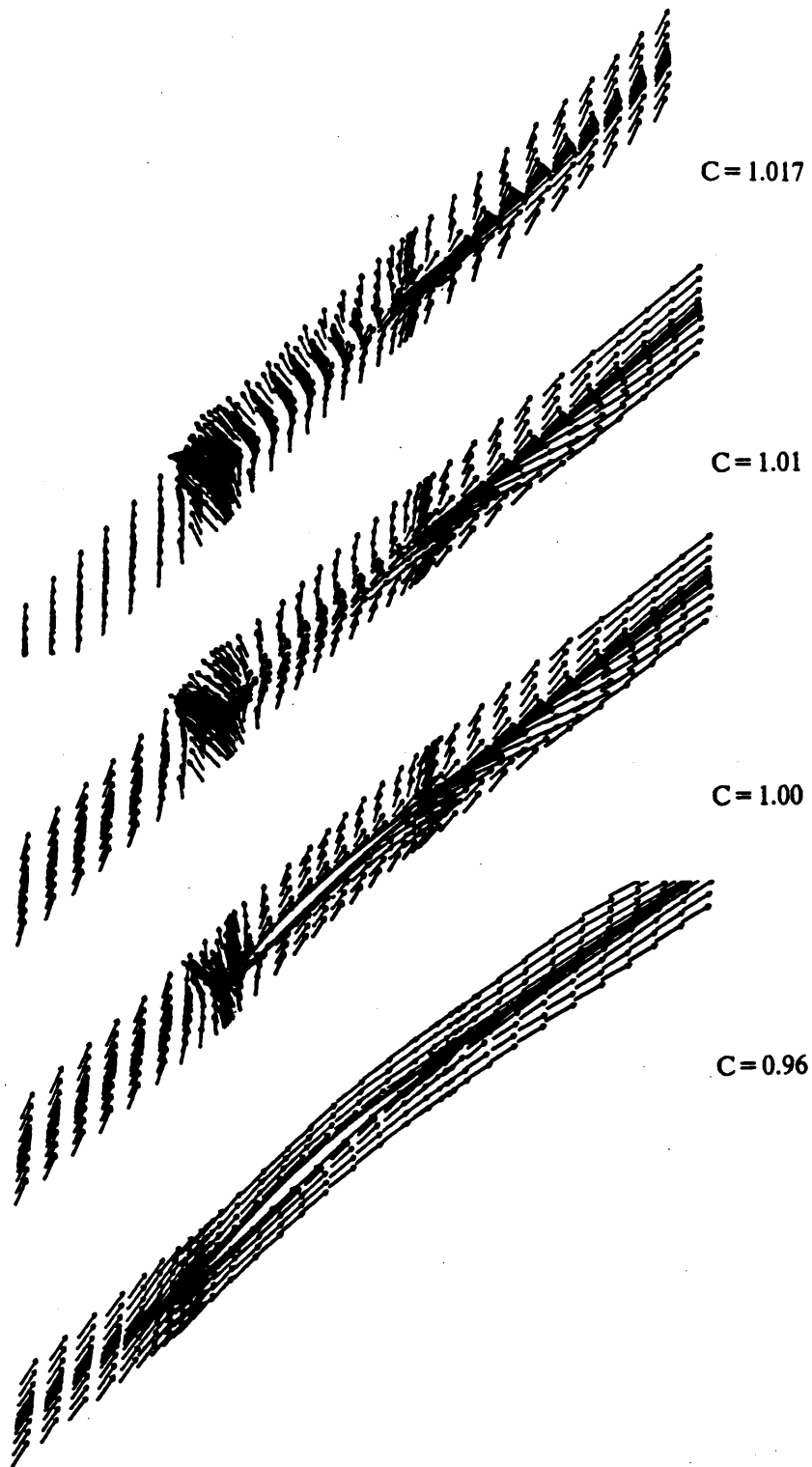


Figure 40. Blade-to-blade views from the 3-D calculation results: velocity vectors within and below the tip gap (hub: $C=0.$, tip: $C=1.$, shroud: $C=1.02$). NOTE: circumferential velocities and distances shrunk by a factor of 5.

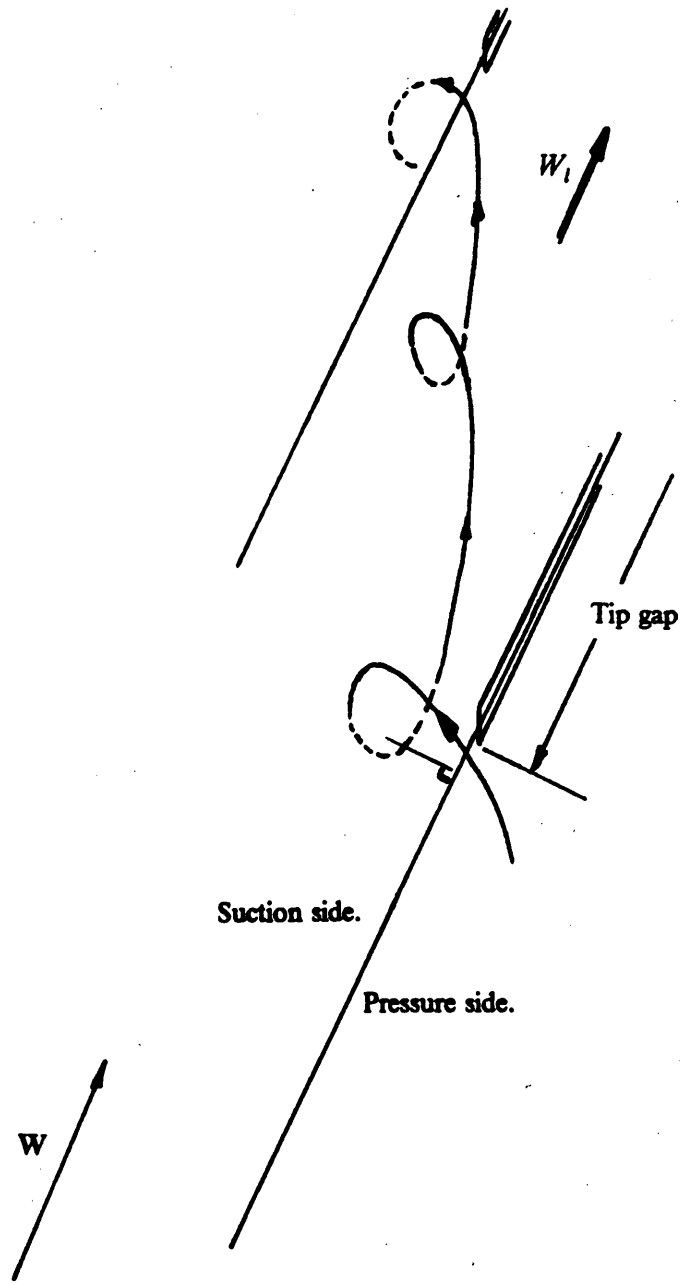


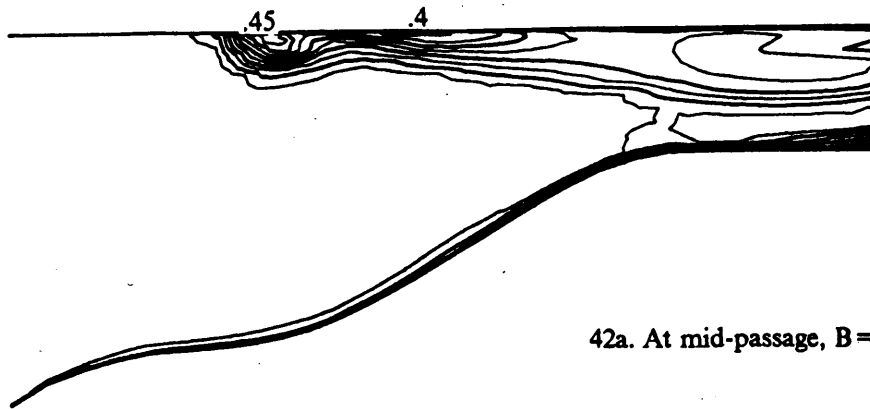
Figure 41. Explanation of circumferential vortex.

5.3.2 Pressure distributions.

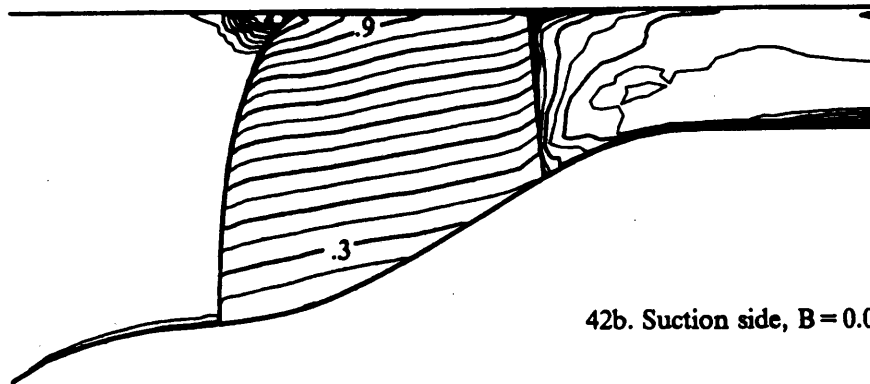
The rotary stagnation pressure loss coefficient contours in meridional and blade-to-blade views reproduce the circumferential vortex upstream the leading edge, near the shroud (Figures 42a, b, and c, and Figure 43a). Figure 42a shows the boundary layer growth at the rotating hub wall, with thickening downstream of the blade passage reinforced by the hub curvature; it also reproduces the convection of the losses from the shroud towards the inner radii along the passage. The boundary layer development at the blade sides appears in Figure 43, at various relative heights. As expected, the contours show a slightly thicker boundary layer on the suction side.

The air-LH₂ analogy developed in Section 4.4 to predict cavitation inception in the liquid hydrogen pump from the 2-D air calculations can similarly be applied to the 3-D calculation results. Figures 44 and 45 show the low static pressure coefficient contours, below the critical value $\psi_s = -0.05$, in meridional and blade-to-blade representations. In both figures we can see two distinct regions of cavitation inception: 1- along the swept leading edge, near the blade suction side, from approximately mid-radius to tip; 2- in the circumferential vortex. It is interesting to notice that the results of this simplified numerical analysis correspond qualitatively well with results of cavitation visualizations made by SEP (reference 40).

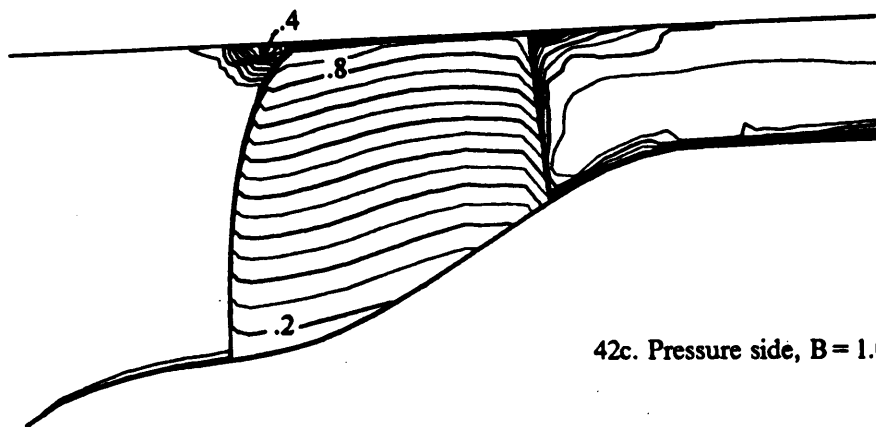
The blade loading, in Figure 46, is simply obtained by the static pressure coefficient difference between the pressure side and the suction side. The high blade loading found at the leading edge near the tip could be the driving force for the strong leakage flow observed in the same region in Figure 40. This is possibly a better explanation than only a blockage effect for the velocities driving the circumferential vortex.



42a. At mid-passage, $B = -3.5$.



42b. Suction side, $B = 0.0$.



42c. Pressure side, $B = 1.0$.

Figure 42. Meridional views from the 3-D calculation results: rotary stagnation pressure loss coefficient contours (from 0.05, by 0.05).

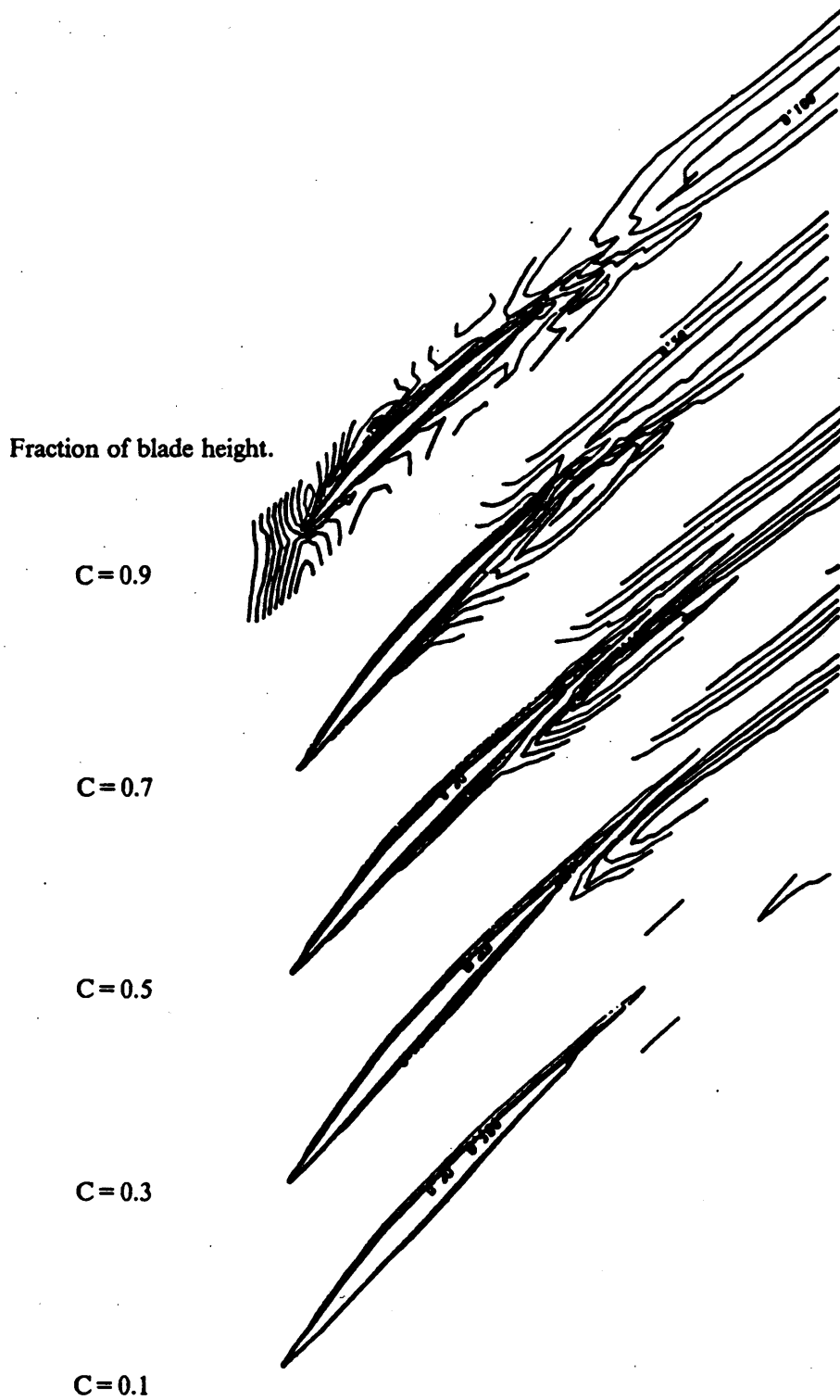


Figure 43. Blade-to-blade views from the 3-D calculation results: rotary stagnation pressure loss coefficient contours (from 0.05, by 0.05).

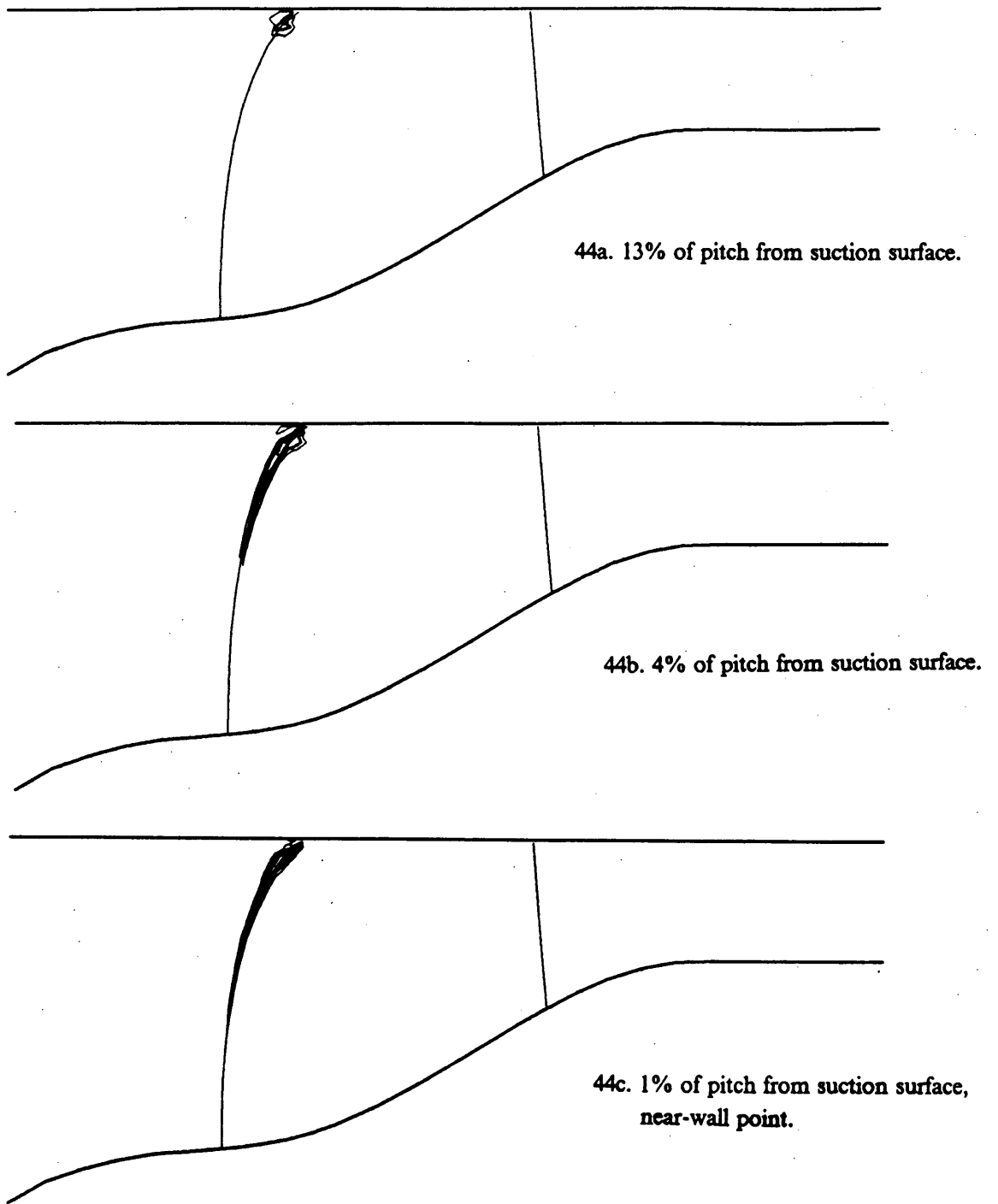


Figure 44. Meridional views from the 3-D calculation results: cavitation static pressure coefficient contours (ψ , from -0.09 to -0.05 by 0.01).

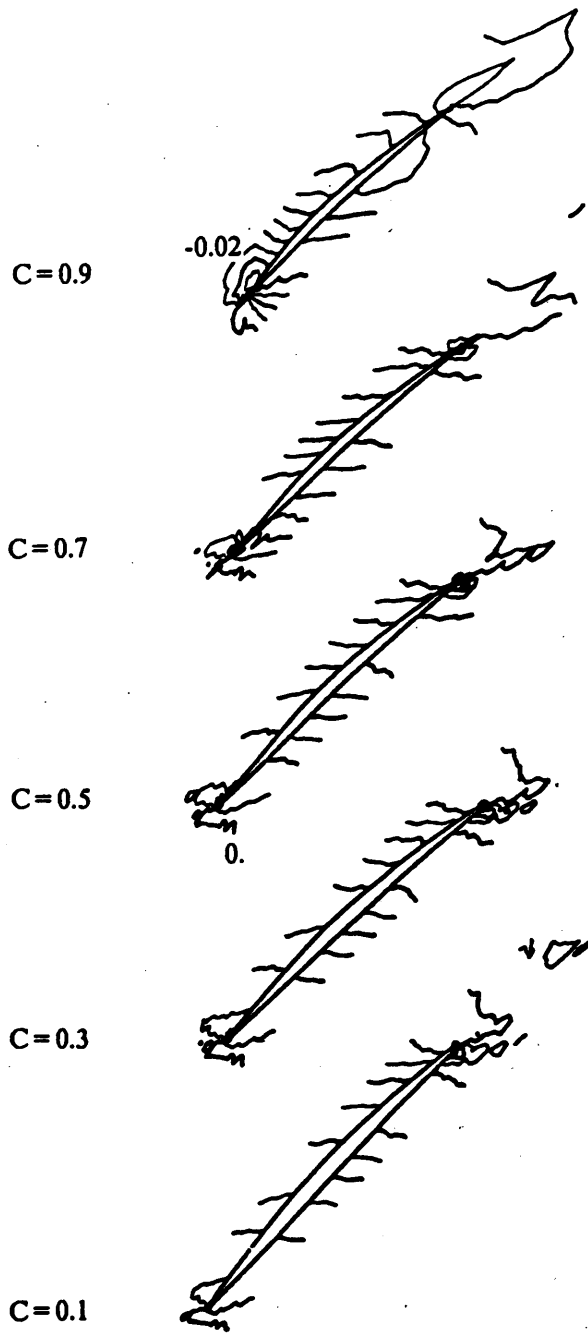
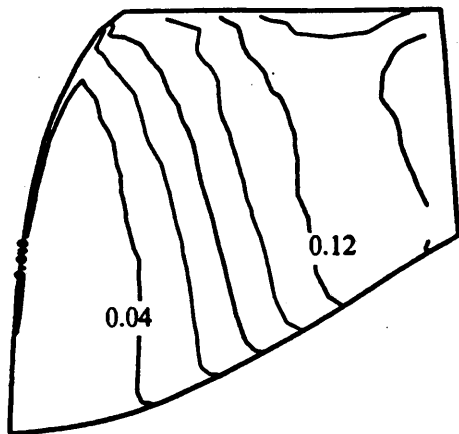
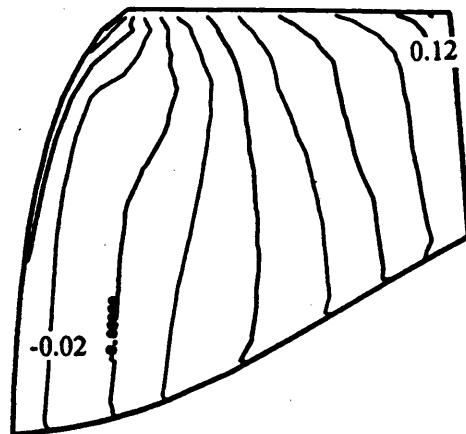


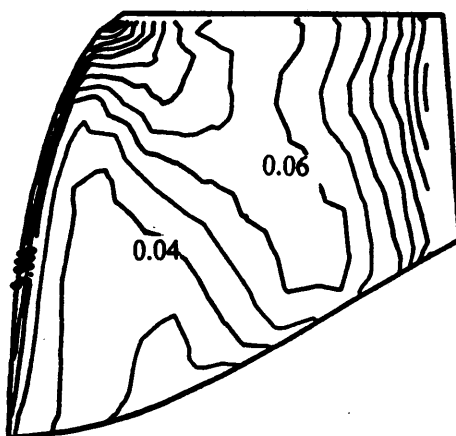
Figure 45. Blade-to-blade views from the 3-D calculation results: static pressure coefficient contours (ψ , from -0.1, by 0.02).



46a. Pressure side.



46b. Suction side.



46c. Pressure difference.

Figure 46. Blade loading calculated distribution: contours of static pressure coefficient, ψ_r .

5.4 *Quasi-cross-sectional analysis of the secondary flows.*

In this Section, a new series of plots is defined, and a more detailed study of the secondary flows is presented.

5.4.1 **Display of the secondary flows in quasi-cross-sectional planes.**

5.4.1.1 *Definition of the iso- θ sections.*

Because of the high stagger angle β' , a blade-to-blade representation of the inducer blades shows that iso- θ planes can be considered as quasi-cross-sectional planes in the blade passages (Figure 47a). The angular error in this approximation is of order 10° over the blade height, and is negligible since the normal projection in cross-section would differ only by a distance factor: $\cos 10^\circ = 0.985$. Thus, in our following discussion, the results observed in iso- θ planes will be considered as cross-sectional distributions.

Using the axisymmetric disposition of the four inducer blades, the flow domain is completely defined by an angular window of $\pi/2$ radians (Figure 47b), the other locations being deduced by simple rotation. However, only one fourth of the total inducer has been defined with a calculation grid around one reference blade and extensions upstream and downstream. Thus, the grid must first be reproduced identically for the three other blades by a "cloning" process. A new grid of the flow field including all four blades is then defined over $\pi/2$ radians (0 and $\pi/2$ being repeating boundaries). In the radial k -direction, the same indexation as for the Master Geometry Grid was conserved. The blade-to-blade j -indexation was transformed into a new axial j' -indexation, keeping 17 points between the blade sides across each passage, totalling $4 \times 17 = 68$ points for the four blades. In order to maintain a reasonable number of grid points, it was finally decided to discretize the angular window in six iso- θ sections, corresponding to the i' -indexation, that is at angles going from 0° to 75° by increments of 15° . The size of the new grid is: $I' \times J' \times K = 6 \times 68 \times 19$ (7752 points). The details of this grid generation starting from the Master Geometry Grid are presented in Appendix C. The method is based on

simple interpolation techniques to define the new grid point locations and their associated flow property values. It should be noted here that no 3-D calculation was performed on the new grid. We only "transferred" the flow calculation results into a more convenient geometric representation where only data processing was applied later later on, and which allowed better pictorial display of the results.

5.4.1.2 Definition of the secondary velocities.

The fundamental reasoning behind the definition of quasi-cross-sections was to study the secondary flows in the inducer passages. From the method described in reference 35, p.4, the relative velocity vector \mathbf{W} is decomposed into a primary component, along the i -lines of the Master Geometry Grid (primary flow direction), and a secondary residual in the cross-sectional planes (or $\text{iso-}\theta$ planes here). The secondary residual of \mathbf{W} includes only radial (hub to tip) and axial (pressure side to suction side in the blade passages) components:

$$\mathbf{W} = W_i \mathbf{i} + W_{r, \text{sec}} \mathbf{u}_r + W_{z, \text{sec}} \mathbf{u}_z$$

where:

\mathbf{i} = unit vector in the i -line primary direction

\mathbf{u}_r = unit vector in radial direction

\mathbf{u}_z = unit vector in axial direction

The details of this decomposition are reported in Appendix C.

In conclusion, we should remember that the secondary velocity vectors evaluated in the quasi-cross-sectional $\text{iso-}\theta$ planes represent the axial and radial departure of the flow from a primary direction along the blades.

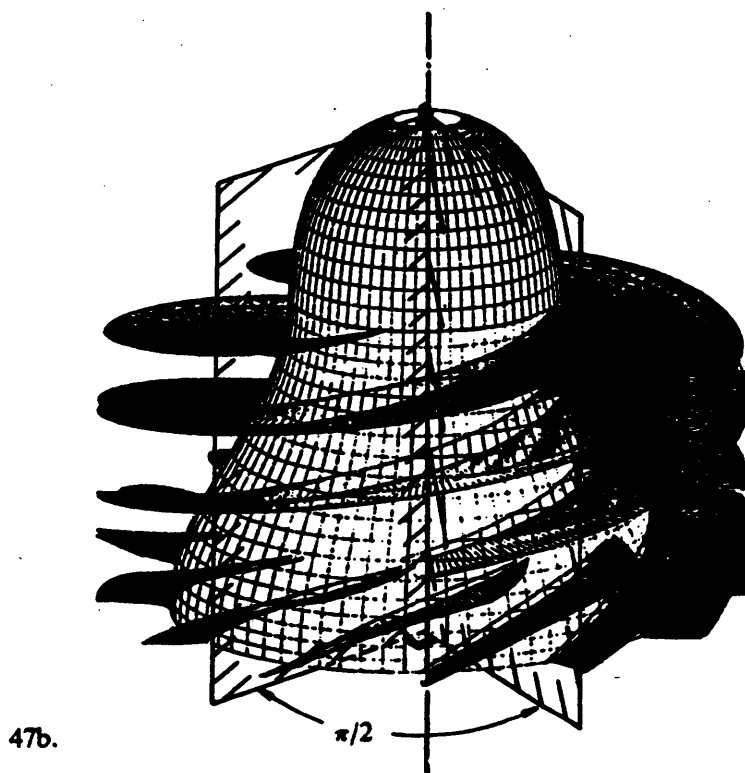
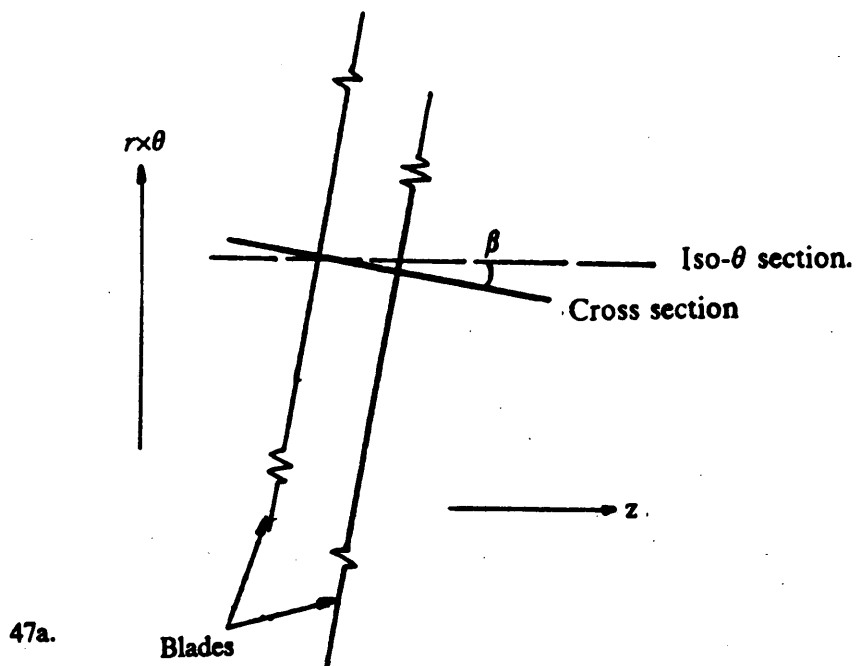


Figure 47. Iso- θ planes definition process.

5.4.2 Static pressure distributions.

Figures 48 and 49 represent the static pressure coefficient distributions in the various iso- θ planes shown in Figure 74, Appendix C. They show notably the evolution of the radial gradient inside the blade passage. They also show the creation of a characteristic low pressure zone along the swept back leading edge, on the suction side. This phenomenon is represented by a concentration of closed contours that appears distinctly on the blade at $\theta = 45$ deg and grows until $\theta = 75$ deg. Then, we must look at the plots $\theta = 0$ deg and $\theta = 15$ deg to follow its evolution towards the end of the leading edge. The picture at $\theta = 30$ deg shows clearly the fully developed low pressure "sink"; however, it is detached from the blade suction side and decays progressively at the same radius for higher values of θ , until it encounters the next blade. This phenomenon corresponds to the development of the suction peak along the leading edge (already visible in Figure 44). Figure 50 shows possible locations of cavitation occurrence along the leading edge and in the tip corner region, as already noticed in the previous section.

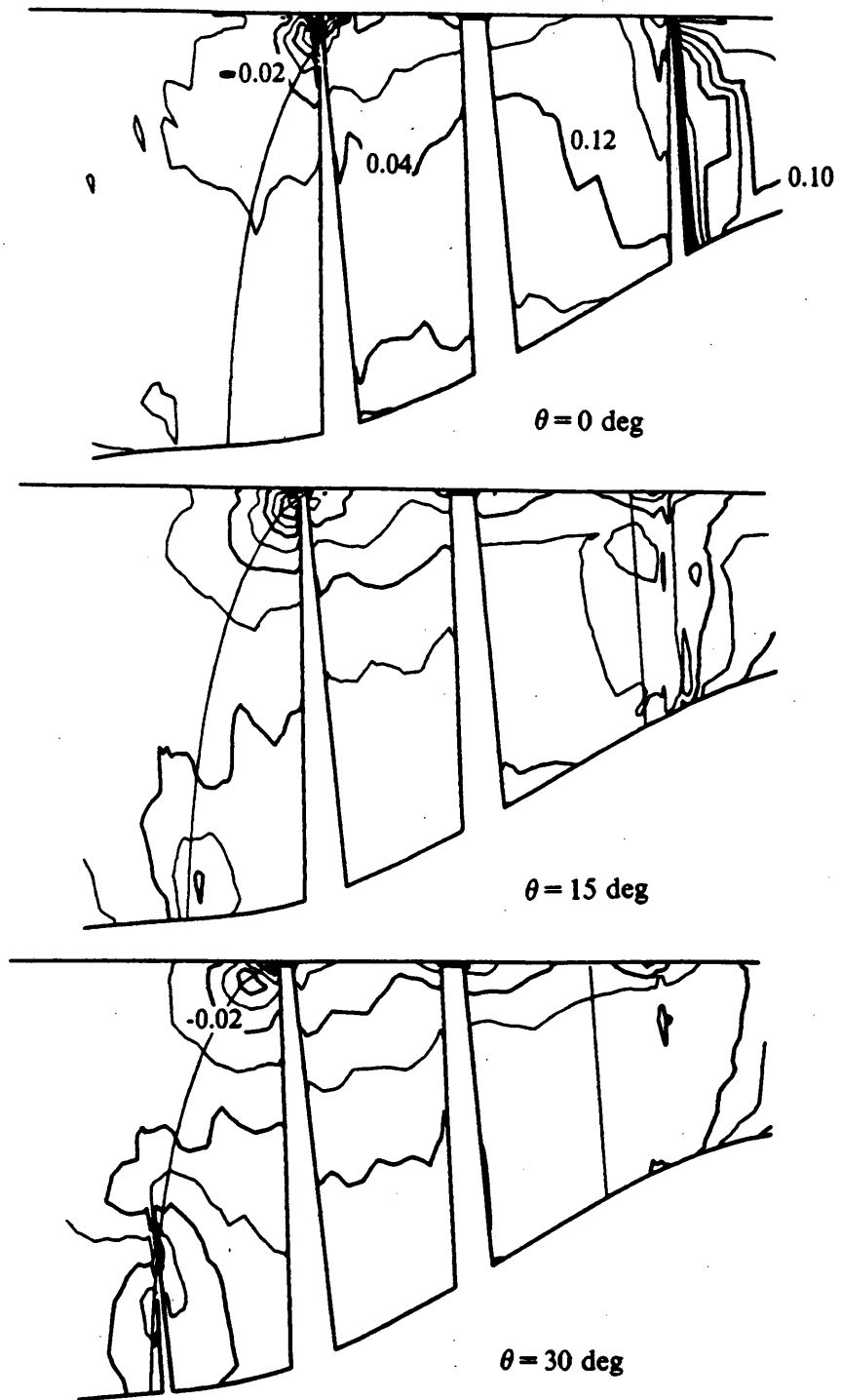


Figure 48. Static pressure distribution in iso- θ planes (a): ψ , from -0.1, by 0.01.

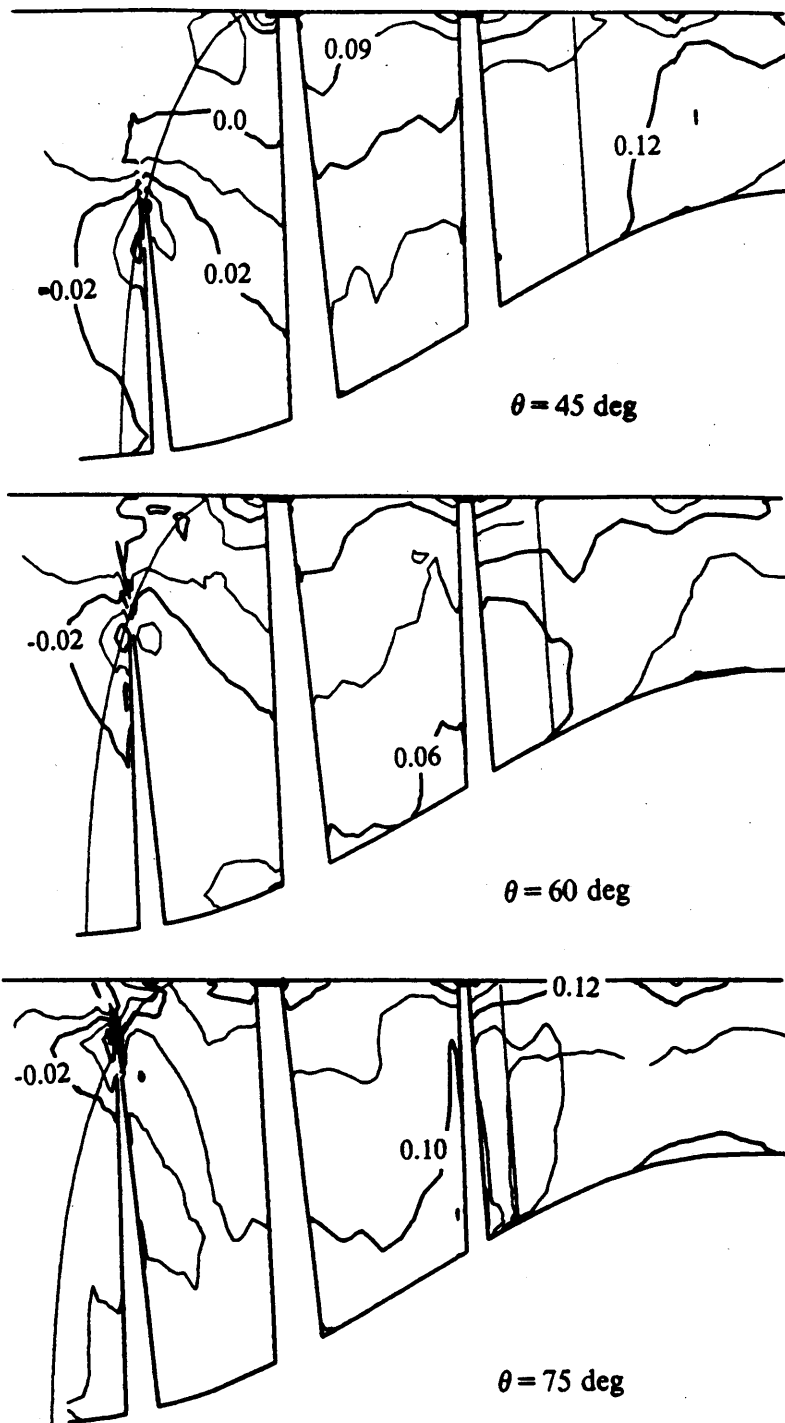


Figure 49. Static pressure distribution in iso- θ planes (b): ψ , from -0.1, by 0.01.

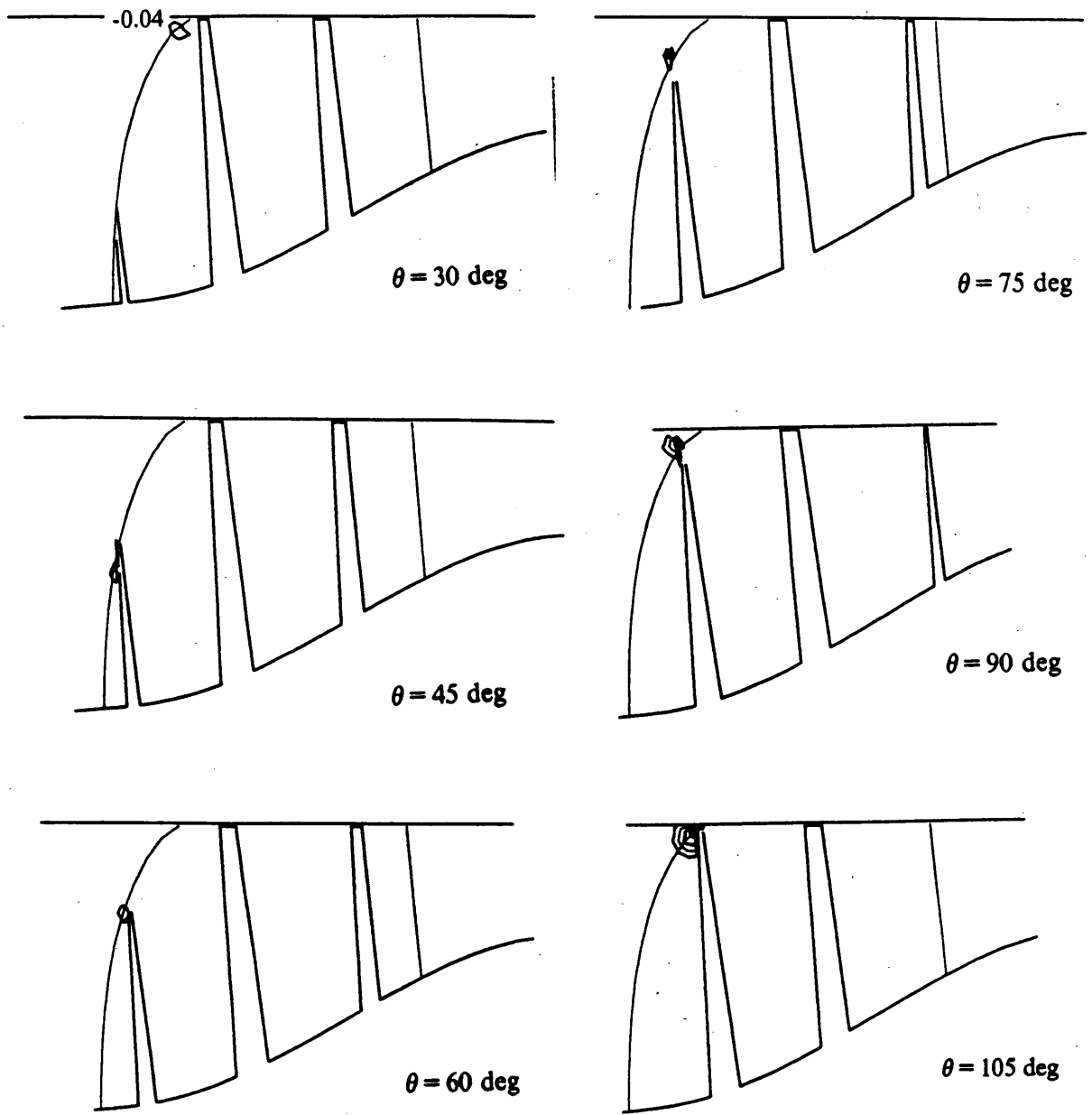


Figure 50. Cavitation occurrence along the leading edge in iso- θ planes: contours of ψ , between -0.1 and -0.04, by 0.01.

5.4.3 Secondary velocity and rotary stagnation pressure loss distributions.

The plots reproduced in Figures 51 through 57, also associated with those of the next section, are probably the most interesting and original representations of the flow phenomena in the first blade row of the axial flow inducer. They emphasize the significant influence of the viscous effects (boundary layers) and the development of strong secondary motions inside the blade passages.

In the following discussion, the insight gained from Lakshminarayana's work (Figure 7 and references in Section 2.) and from Moore's discussion of 3-D flows (reference 39) was very helpful in identifying some of the general features observed in the flow calculation results. The quantitative characterisation of these and some new details resolved in the calculation contribute to the originality of the work reported in this thesis. It will be seen that the development of the secondary flows and the loss distributions are closely linked.

5.4.3.1 *Upstream of the leading edge.*

In all the iso- θ pictures displaying secondary velocities (Figures 52 to 55), the velocity vectors shown upstream of the leading edge have a negative axial component, increasing from hub to shroud. This negative axial component is created by the fact that the grid upstream the leading edge (as well as downstream of the trailing edge) is inclined at the blade angle (pressure side) and that the inlet flow has an incidence angle of 3 deg relative to the blade angle (Figure 51). The magnitude of this component depends only on the inlet velocity profile, including the boundary layer effects at the walls.

5.4.3.2 *Tip leakage flow.*

Figures 54 and 55 show the tip leakage flow details. The second one describes the evolution of the secondary velocities as the swept back leading edge develops, and the first shows the stabilized tip gap flow.

In Figure 54, the tip leakage flow produces large secondary relative velocities of the same order as the tip speed, emphasizing the crucial importance of this phenomenon. Two regions marked A and B correspond to the primary tip leakage flow, and to the interesting secondary influence of the previous blade's tip leakage, respectively. This secondary effect is convected across the blade passage and affects the current blade because of the high stagger angle, in a manner similar to that discussed in the case of the circumferential vortex (Section 5.3). Although this contribution is affected by the primary flow transport as well as by the various other 3-D secondary flows which develop near the shroud, the length of the vectors in region B compared to those in region A show the important effect of this secondary component on the overall tip leakage flow. The strength and the development from blade to blade of this secondary flow is also characterized in terms of total pressure losses in Figures 56 and 57. We find higher losses due to large friction (high relative velocities), boundary layer accumulation and mixing. The extension of the high loss contours across the blade passage, with decreasing magnitude from suction side to pressure side, corresponds well to the secondary tip leakage flow contribution convected near the shroud from blade to blade.

In Figure 55, the tip leakage around the leading edge is described. The typical regions of interest are marked A, B, C, D, and E. In region A, the influence of the secondary tip leakage flow is shown to be very large, especially because no attenuation has been yet provoked by other secondary flow (we are only at the beginning of the blade passage). Region B represents the development of the streamwise component of the leading edge vortex, with negative radial velocities after the suction side (recirculation is not noticeable on this picture). Region C characterizes the very large secondary relative velocities attained at the end of the swept leading edge, immediately upstream the tip gap region, because of blockage. Again, in Figures 56 and 57, this region coincides with the higher losses experienced by the flow, with a relatively important extension upstream. In Figure 55c, the established tip leakage regime is reached, and regions D and E correspond then to A and B in Figure 54.

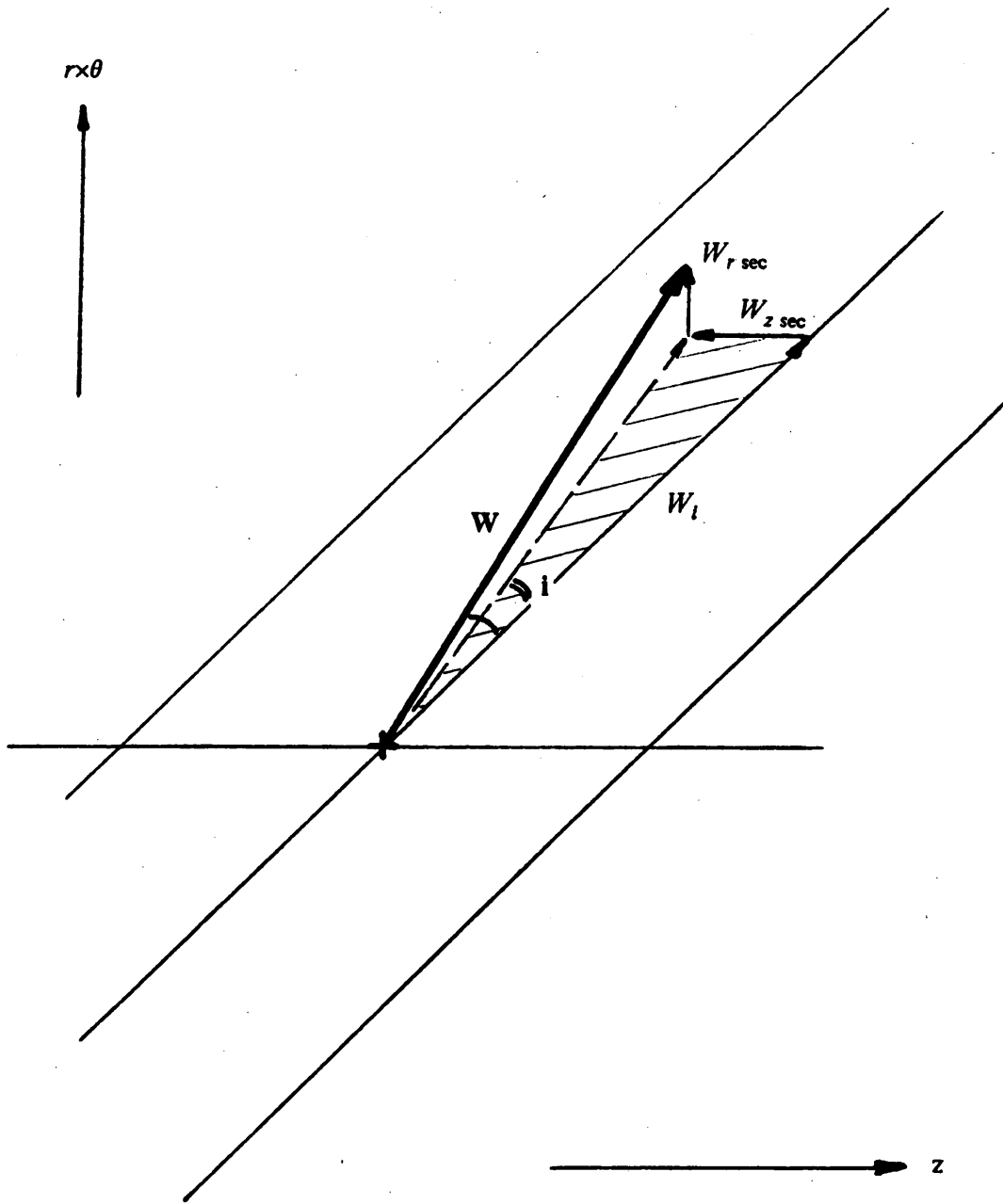


Figure 51. Secondary velocity vectors upstream of the leading edge: explanation of the negative axial component.

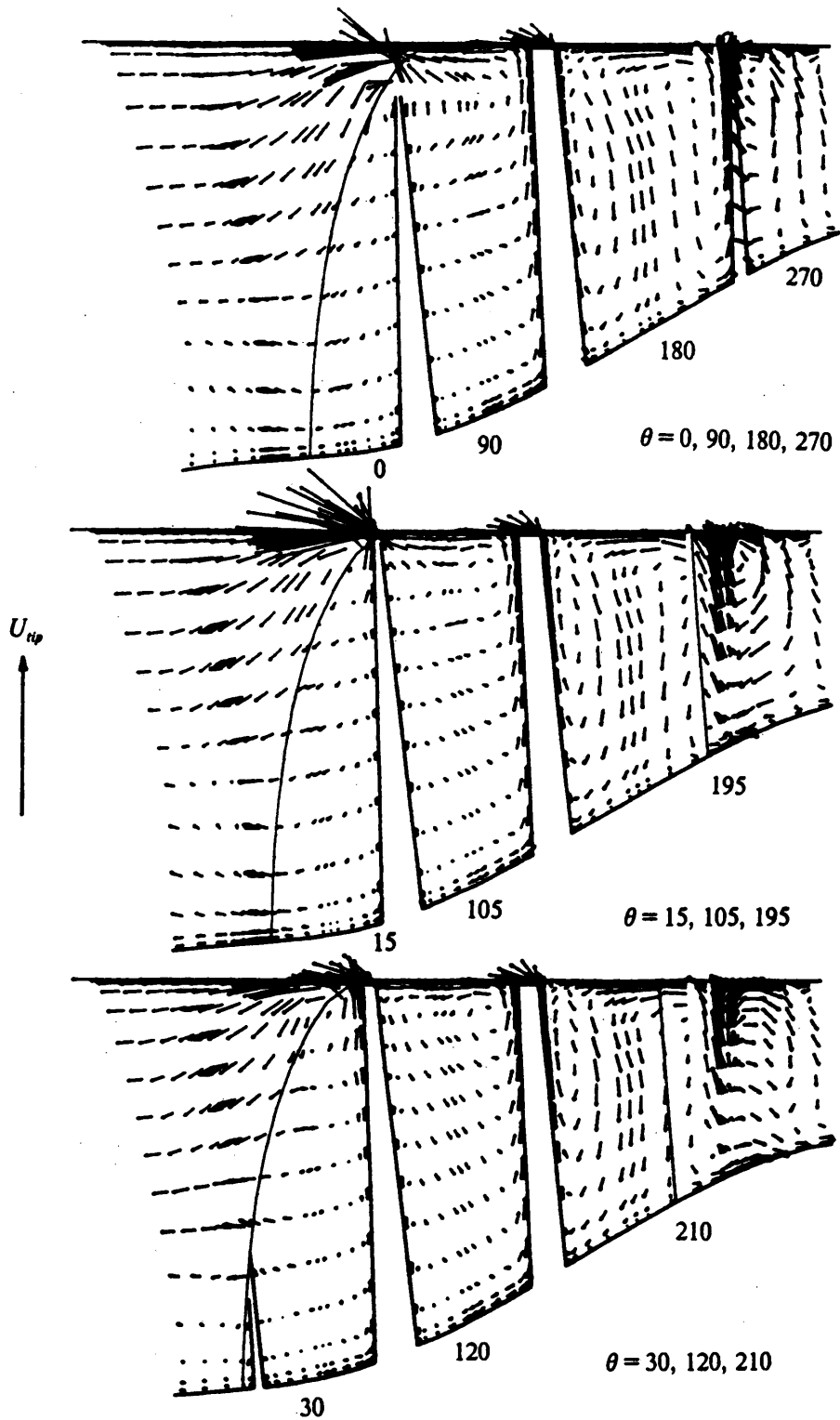


Figure 52. Velocity vectors in iso- θ planes (a).

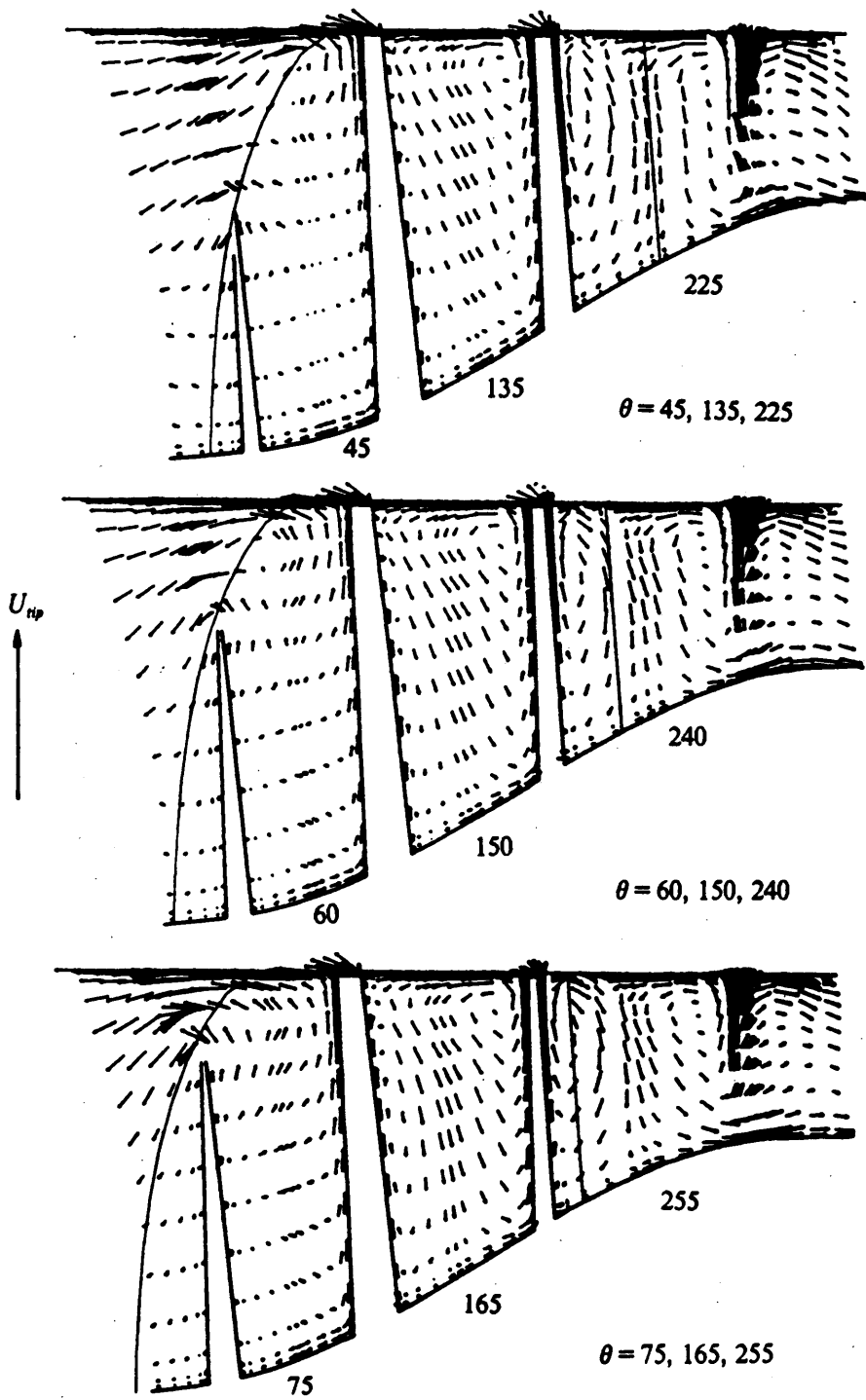


Figure 53. Velocity vectors in iso- θ planes (b).

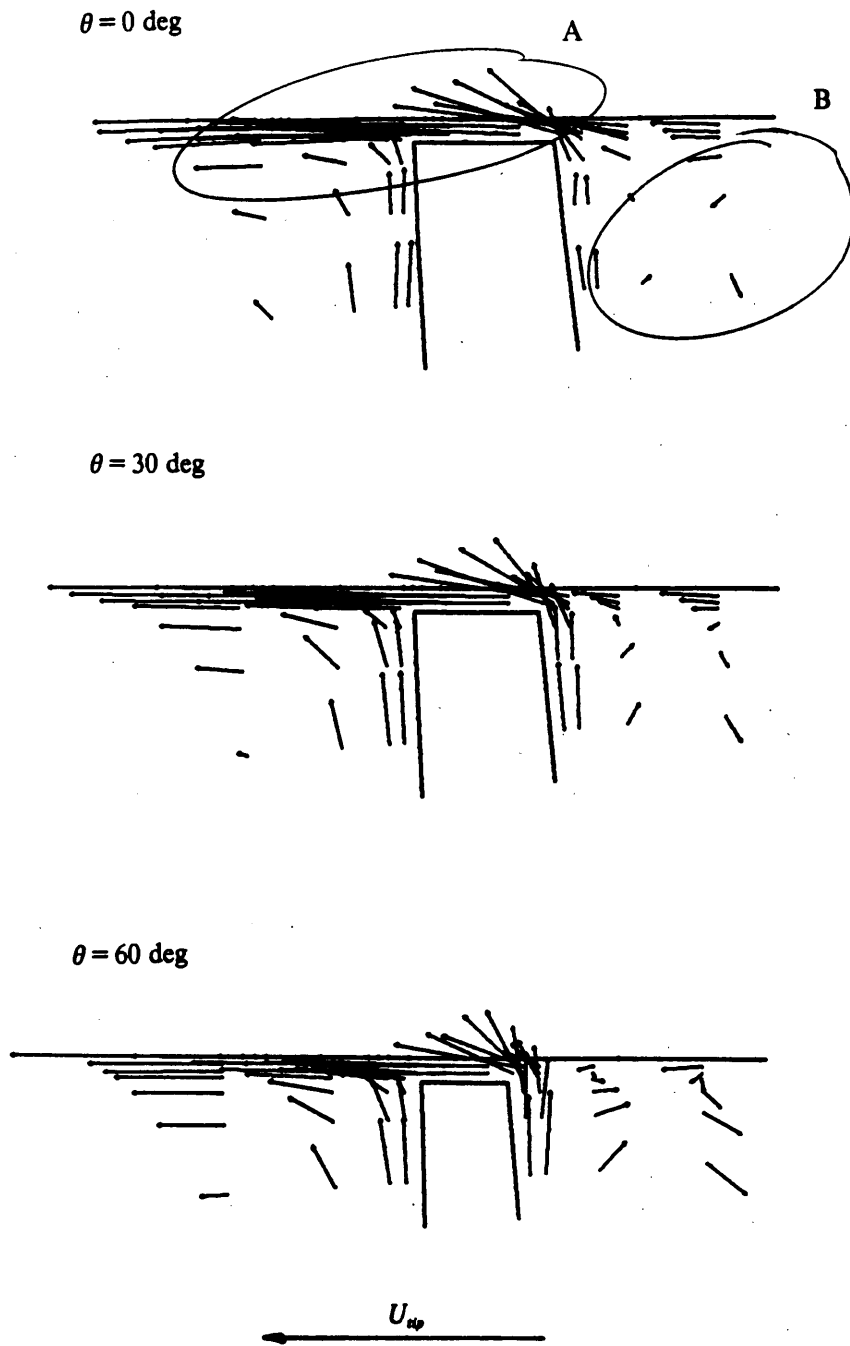


Figure 54. Tip leakage flow analysis in iso- θ planes: phenomena in the tip gap.

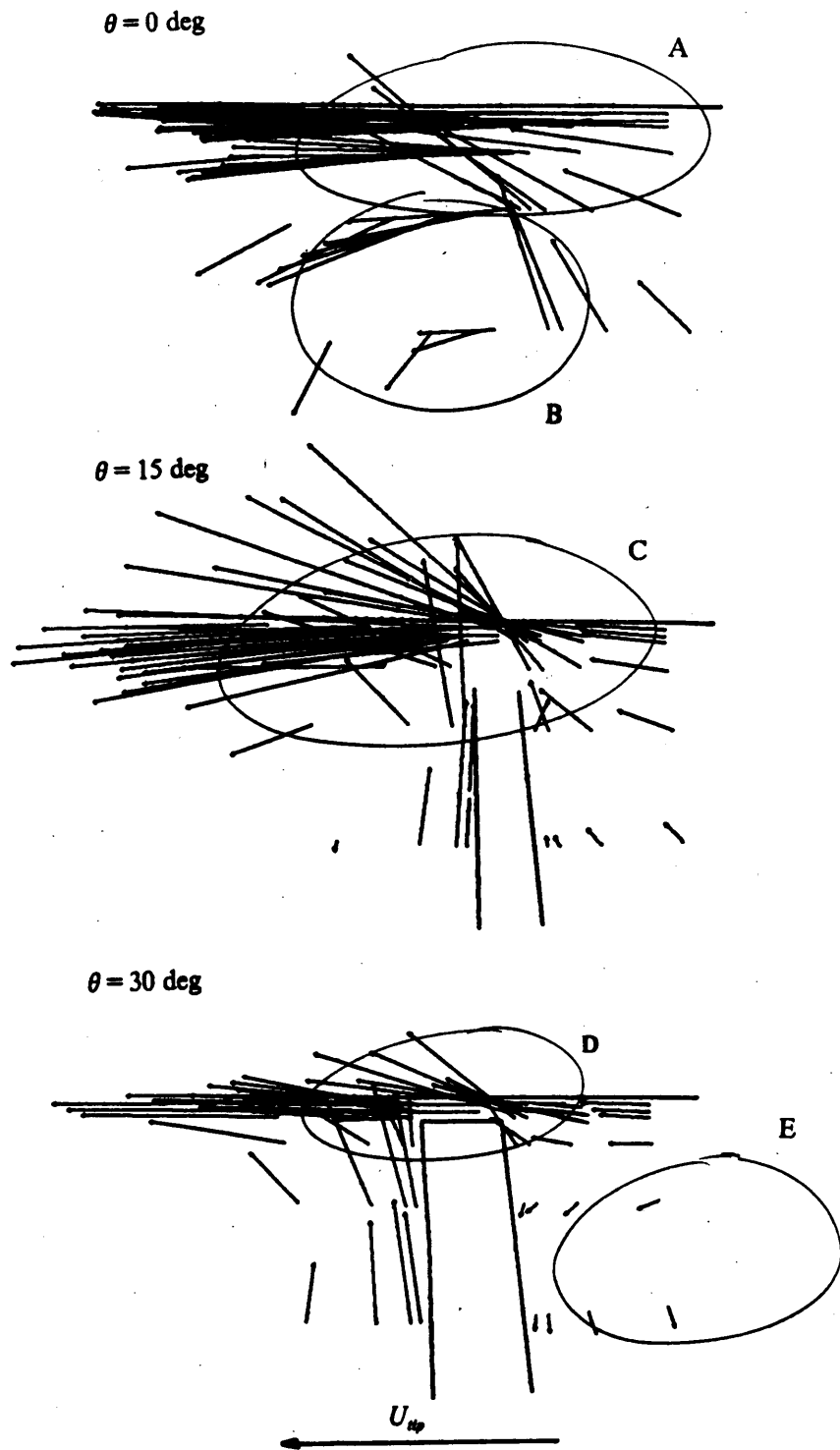


Figure 55. Tip leakage flow analysis in iso- θ planes: phenomena around the leading edge.

5.4.3.3 *Secondary flow in the boundary layers.*

In the inducer passages, the development of the boundary layer is a fully three dimensional process that affects the entire flow. The streamwise growth of this viscous phenomenon on the blade sides is described in the next Section. Here, we present the axial and radial components of the blade, hub, and shroud boundary layers.

At the hub

Near the hub, the radial (and axial) component of the secondary velocities is very small, when not equal to zero. These velocities generally increase from pressure side to suction side, corresponding to a domination of the pressure influence in this region of low velocities. The friction losses associated with this hub boundary layer are shown in Figures 56 and 57.

From hub to tip

From hub to tip, the general secondary flow pattern seen in Figures 52 and 53 corresponds well with that in Figure 7. Near the blade sides, radial outflows develop in the boundary layer region, generated by a streamwise component of vorticity created by the rotary stagnation pressure gradient across the blade passage (reference 39, p. 1-30). This centrifuging of the blade boundary layer fluid is observable on both sides of the blade, but its intensity varies significantly along the passage. In order to perceive this, start with the plot corresponding to $\theta = 30$ deg, on the left side, where the leading edge starts to appear and creates the beginning of a passage. Then, follow the evolution of the flow inside this same blade passage, from $\theta = 30$ deg to $\theta = 75$ deg, then again from $\theta = 90$ deg to $\theta = 165$ deg in the middle of the iso- θ plots, and finally at $\theta = 180$ deg, where the trailing edge of the other of the two blades defining the passage is located. (Note: if we follow one single blade outline in the iso- θ planes, from the leading edge appearance at $\theta = 30$ deg to the trailing edge location at $\theta = 270$ deg, we find that the angular wrap at the hub is between 240 and 255 deg; this is consistent with the value of 242 deg given by SEP).

From $\theta = 30$ deg to $\theta = 90$ deg, the radial outflow velocities increase from hub to tip for both sides of the passage, being however much larger on the suction side than on the pressure side, by a factor of almost 5! By $\theta = 105$ deg, two interesting developments have occurred. First, a certain stabilization of the secondary radial velocities can be noticed

on the suction side, from mid-height to tip, attaining orders of 10% of the tip speed. However, on the pressure side, the secondary leakage flow convected from the previous blade tip provokes severe disturbance of the radial boundary layer outflow at outer radii, balancing or even dominating it from $\theta = 120$ deg to $\theta = 150$ deg where radial inward motions occur (Figures 52 and 53). For higher angles, this tendency is again reversed, the centrifuging effect on the blade pressure side having become stronger.

The boundary layer development at the blade walls is also represented in Figures 56 and 57 (rotary stagnation pressure loss contours).

5.4.3.4 Other 3-D secondary flow effects.

In the core region of the blade passages, a large radial inward motion builds up progressively with increasing secondary velocity amplitudes. From $\theta = 75$ deg to 105 deg, this motion develops only from mid-height to hub. After 120 deg, it grows strongly until the passage exit, dominating largely the axial velocity components. The velocities found are of the same order of magnitude as those in the blade boundary layers. We have already mentioned that the shroud region is largely dominated by the tip leakage flow phenomena, creating negative axial and radial secondary velocity components. The accumulation of boundary layer flows from the blade sides increases also radial inward motions at mid-passage because of blockage and radial equilibrium in the momentum equation (region of low velocities, thus the centrifugal accelerations do not balance the pressure gradient anymore). These two effects combined explain the radial inward flow in the core region of the passage.

5.4.3.5 Evolution of rotary stagnation pressure losses.

As explained in section 5.2.2, the term $(P_0 - P^*)$ represents the total pressure loss. Figures 56 and 57 present the distributions of the rotary stagnation pressure "loss" coefficient, ψ .

They show the influence of secondary flows on the loss accumulation. As mentioned above, we see a high loss production in the blade boundary layers (near the blade

surfaces, and increasing towards outer radii), at the shroud (where tip leakage mixing is very large, with convection from suction side to pressure side in the blade passage, and also because of the boundary layer accumulation), and in the thin hub boundary layer.

These figures also show the evolution of the wake downstream of the blade trailing edge. From $\theta = 0$ deg to $\theta = 75$ deg, the wake spreads out and moves progressively towards outer radii. This tendency is explained by the radial flow downstream of the trailing edge shown earlier in Figures 52 and 53. The presence of the wake is important for the designer because it influences the flow distribution at the inlet of the next blade row.

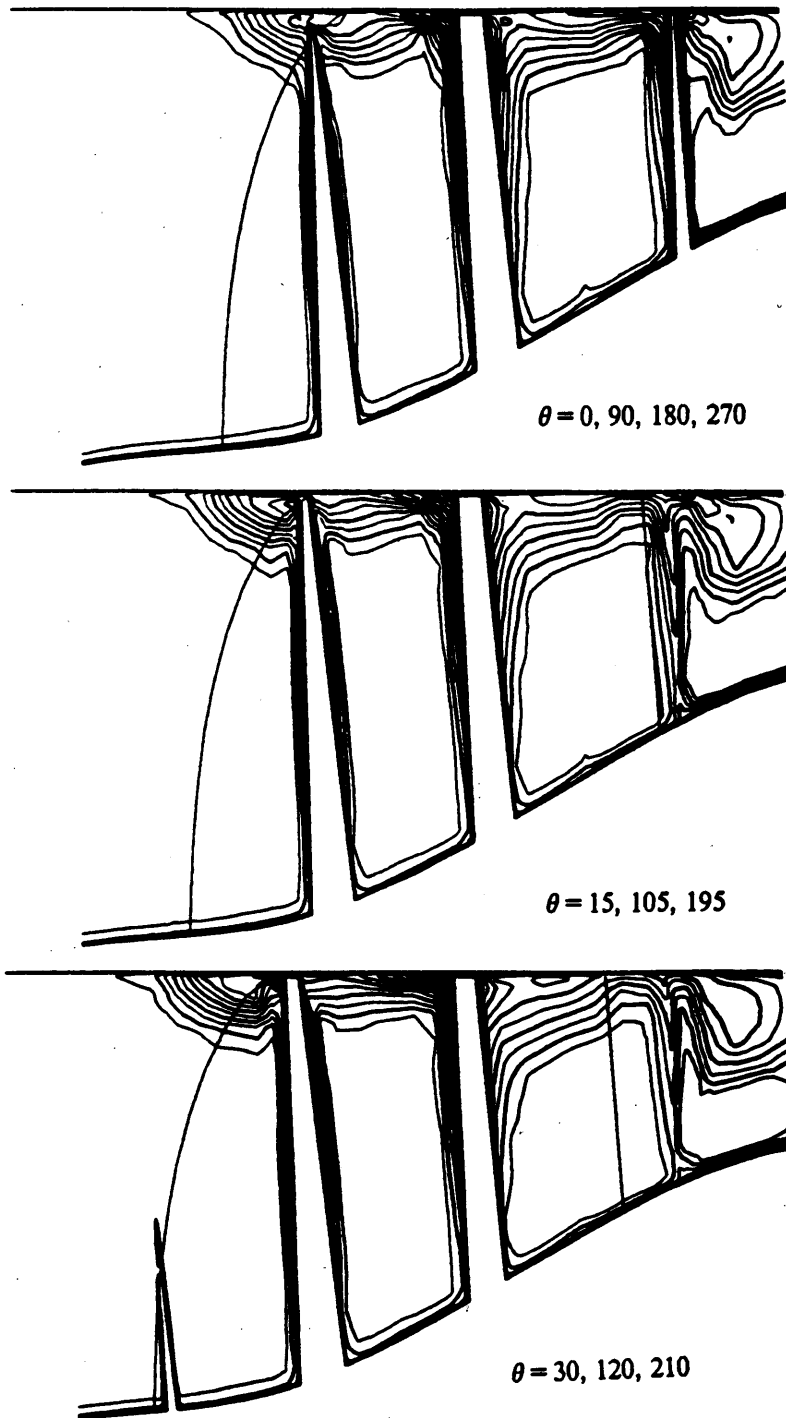


Figure 56. Rotary stagnation pressure loss distribution in iso- θ planes (a): ψ , from 0.05, by 0.05.

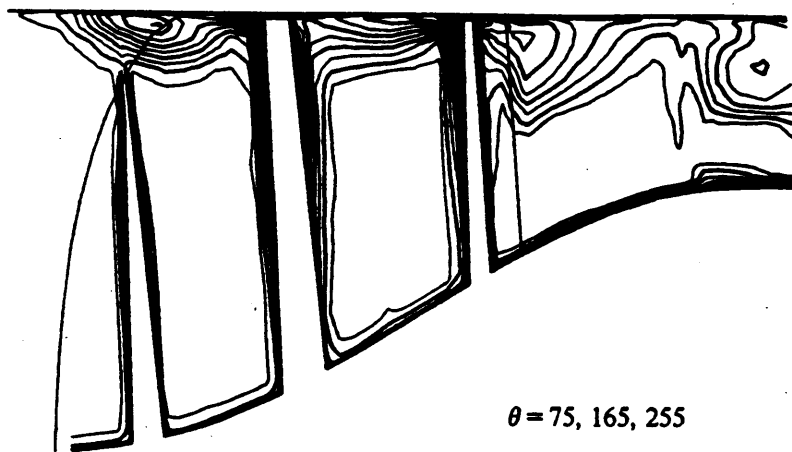
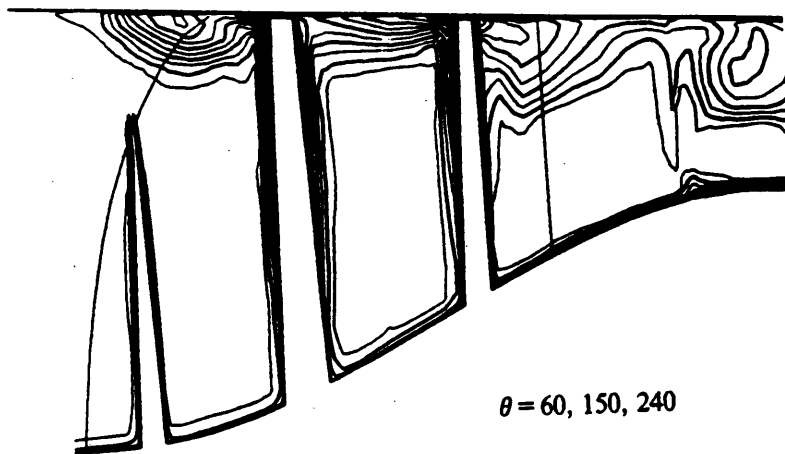
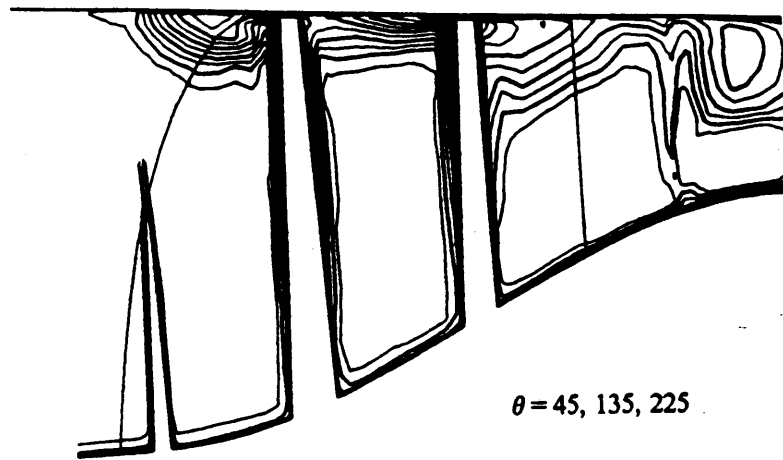


Figure 57. Rotary stagnation pressure loss distribution in iso- θ planes (b): ψ_r from 0.05, by 0.05.

5.4.4 Streamwise evolution of the radial secondary velocity at mid-height.

Figure 58 shows the evolution of the profile of the secondary radial velocity component along the blade passage, at mid-height (the flow grid points are taken at $k=9$). This picture completes the previous discussion of the results in iso- θ planes, since we can either clearly study the boundary layer growth on both sides over one complete blade chord (using the repeating boundaries of the domain shown), or focus on the radial secondary motions in the core region of the inducer passages.

The analysis of the velocity profiles near the blade shows that radial motions start immediately at the blade leading edge ($\theta=45$ deg), with inward flow on the suction side and outward flow on the pressure side. This corresponds to the tip leakage over the swept-back leading edge. At $\theta=75$ deg, the boundary layer starts to develop distinctly on the pressure side. It starts at $\theta=90$ deg on the suction side. From $\theta=135$ deg, the tendency is reversed and the radial velocities centrifuged in the blade boundary layer are larger on the suction side, inside the passage (that started at $\theta=135$ deg, approximately).

From $\theta=180$ deg, which marks the end of the passage for the pressure side, the radial velocity amplitude increases again significantly on the pressure side, which is now an uncovered section at the inducer exit, before decaying again at the trailing edge. On the suction side, a quasi-fully-developed profile is reached towards $\theta=165$ deg and until almost the blade trailing edge. The changes in amplitude on the suction side are very small, whereas they are much larger on the pressure side. At $\theta=165$ deg, the maximum radial velocity ratio is about 1.4 in favor of the suction side; it is about 1 at $\theta=195$ deg; and grows rapidly to 1.7 in favor of the pressure side at $\theta=240$ deg, before decreasing back to almost 1 at the trailing edge.

This quantitative picture shows how complex these viscous phenomena are inside the inducer passages, and their primary importance in the flow analysis. A partial explanation of these strong variations can be advanced from the insight gained in earlier analysis of the flow calculation results in other representation systems. We have effectively noticed that the apparent boundary layer growth on the pressure side became more rapid as the blade was not covered anymore, that is, no more under influence from any other blade. This suggests that the smaller radial components observed before may be caused by contrary negative radial flows from tip leakage over the previous blade tip. We have already seen the importance of this phenomenon and how it was extending across the whole passage (Figures 54 and 55).

The boundary layer thickness is difficult to appreciate precisely on these plots, but it seems to be of same order on both sides of the blade, in the inducer passages.

Concerning the radial motions in the core region of the passages, we can notice that they start to increase continuously at $\theta = 105$ deg, being generally of the same order as the boundary layer outward radial flows near both sides of the passage. Starting at $\theta = 90$ deg, we can remark a peak of negative radial velocities always present near the pressure side. Again, this can be interpreted as a result of the secondary tip leakage convected from the previous blade; this effect has already been shown in Figures 52 to 55.

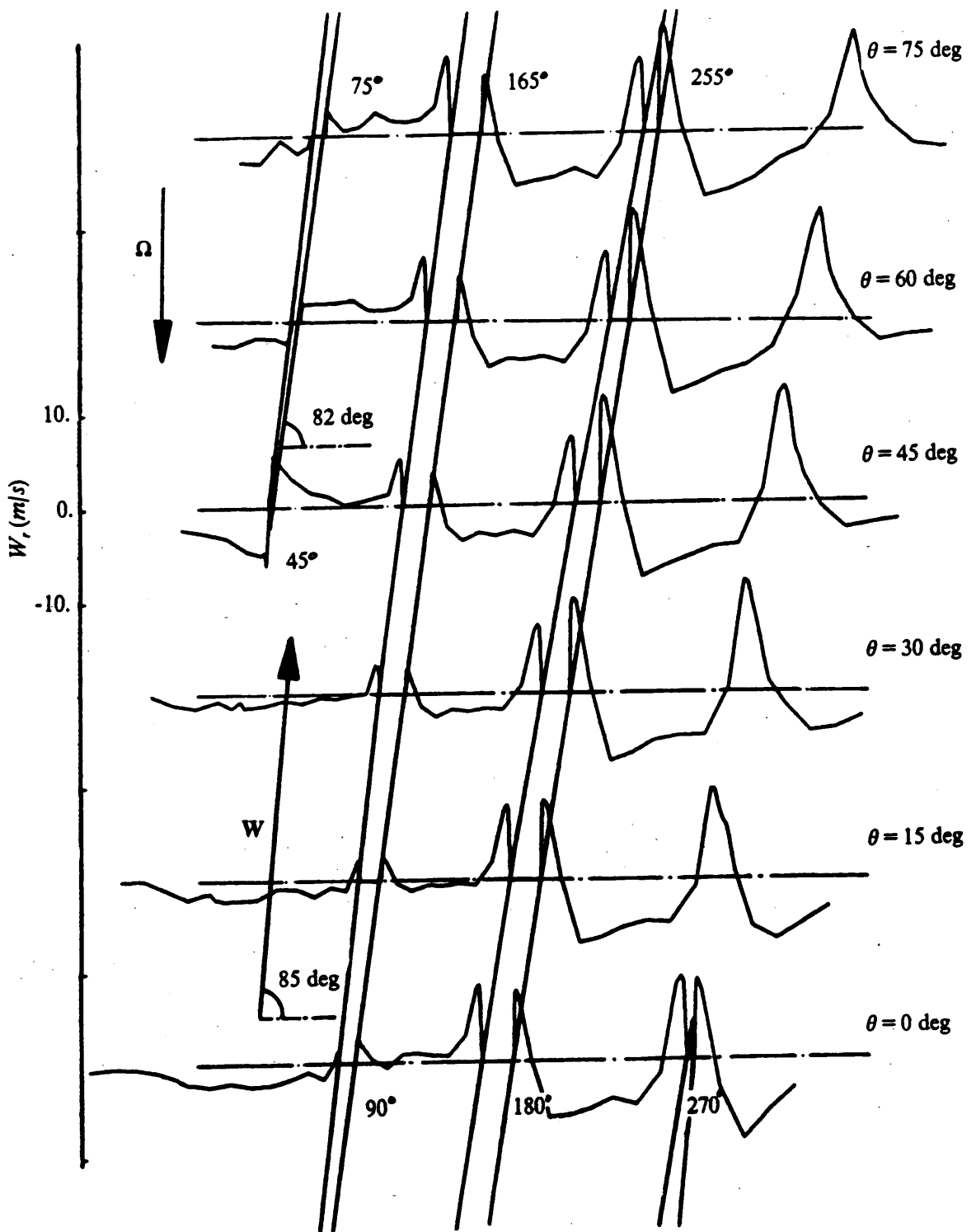


Figure 58. Evolution of the radial secondary velocity profile along the blade passage: showing blade boundary layer growth at mid-height ($k=9$)

5.5 Comparison of the 3-D flow calculation with available air test data.

The air tests described in reference 25 permitted measurements to be made at two stations, at inducer inlet and at inducer exit, corresponding respectively to the planes P10 and P11 sketched in Figure 15. In the calculation grid, two surfaces of constant i -index number have been chosen, one shortly upstream of the blade leading edge ($i=7$), and one shortly downstream of the trailing edge ($i=28$) - the blade ends are located at $i=12$ and $i=25$ - in order to correspond as closely and simply as possible to the actual measurement plane locations. These two surfaces in the calculation grid are shown in Figure 59.

On each of these surfaces, the radial distribution of the principal area-averaged flow properties has been evaluated. The area-average represents approximately the stationary probe measurements and is mathematically defined by:

$$\bar{A} = \frac{\iint A \cdot dS}{S}$$

where S is the surface area over which the property is averaged. Here, because of the axisymmetry, this area average reduces to a pitch average between the two tangential repeating boundaries.

$$\bar{A}(r) = \frac{\int A(r) \cdot d\theta}{\Delta\theta}$$

Figures 60 to 69 show the comparison of radial distributions for \bar{P} , \bar{p} , \bar{P}^* , \bar{V}_θ , and \bar{V}_m .

5.5.1 Inlet station.

The calculation agrees very well with the data, where measurements are available (i.e. up to 90% of the passage height), and for all parameters.

The calculated distributions of P , and p , are very close to the values measured, as shown in Figures 60 and 61. In Figure 62, we see that the agreement for P^* is generally better than 10% of the maximum variation for the entire passage height.

At the outer radii, p , varies little; but P^* varies a lot. In Figure 63, in this region, V_θ has increased by approximately 5 m/s. W_θ has correspondingly decreased by about 5 m/s (from the inlet velocity triangle), and this explains the variation of W in Figure 65. From the definition of P^* , we can write:

$$P^* = p_s + \frac{1}{2} \rho W^2 - \frac{1}{2} \rho r^2 \omega^2$$

$$P^* = p_s + \frac{1}{2} \rho (W_r^2 + W_\theta^2 + W_z^2) - \frac{1}{2} \rho r^2 \omega^2$$

But since W_r and W_z are negligible compared to W_θ (velocity triangle, with high flow angle), the equation can be reduced to:

$$P^* \cong p_s + \frac{1}{2} \rho (W_\theta^2 - r^2 \omega^2)$$

And since:

$$W_\theta^2 = (r\omega - V_\theta)^2$$

we have:

$$P^* \cong p_s + \frac{1}{2} \rho (V_\theta^2 - 2r\omega V_\theta)$$

Neglecting V_θ^2 , we finally find:

$$P^* \cong p_s - r\omega V_\theta$$

Thus,

$$\delta P^* \cong \delta p_s - r\omega \delta V_\theta$$

p_s is approximately uniform, and thus, from the results in Figure 63:

$$\delta P^* \cong 0 - 1.225 \times 95.2 \times 5 = -570 \text{ Pa}$$

This result agrees with the calculated δP^* as shown in Figure 62 at the outer radii. The above analysis gives a simple model of loss production for fluid in the circumferential vortex near the blade leading edge.

We can also see the development of the inlet boundary layer from the nearly fully developed flow in the pipe upstream, in Figure 64.

The agreement observed justifies the choice of fully developed flow for the inlet boundary condition, and the method of establishing the inlet condition for the 3-D flow calculation using the preliminary meridional flow calculation.

5.5.2 Exit station.

At the exit station, the calculation still agrees generally well with the data for most of the parameters. However, a detailed quantitative analysis shows that, for the measured values compared to the flow calculation results:

- P_s is high by approximately 200 to 300 Pa near the tip;
- p_s is high by a similar amount;
- P^* shows very good agreement;
- V_θ is low by approximately 2 m/s out of 10 to 20 m/s (mean value) where measurements are available;
- V_m agrees well;
- W is high by approximately 2 to 3 m/s out of 70 m/s (mean value).

The relative difference is about 25% for p_s and 15% for P_s , but the absolute pressure difference is similar for both parameters, indicating that the correspondence comes from the definition of the stagnation pressure which involves the static pressure. The lower value found in the calculation of the static pressure can be explained by application of radial equilibrium for the whole passage height.

$$\frac{\delta p_s}{\delta r} \cong \rho \frac{V_\theta^2}{r}$$

And then, from hub to tip,

$$\delta p_{s \text{ hub-tip}} \cong \rho \frac{V_{\theta}^2}{r} (\delta r)_{\text{hub-tip}}$$

For a mean value of V_{θ} , we find:

$$\delta p_{s \text{ hub-tip}} \cong 150 \text{ Pa}$$

And this is what the calculation gives. So it seems to satisfy radial equilibrium. However, the data gives:

$$\delta p_{s \text{ hub-tip}} \cong 500 \text{ Pa}$$

This much larger value is possibly due to the next blade row which was present in the air test measurements, creating blade blockage and radial redistribution of the flow across the passage height.

The difference observed for the other parameters (velocities) is explained in the next section.

5.6 *Influence of exit static pressure on work done.*

5.6.1 **Velocities investigated.**

We have already discussed the origin of the pressure difference noticed at the exit station. We now want to study its influence on the other flow parameters investigated.

As shown in Figure 67, p_s calculated is low by approximately 250 Pa near the tip, compared to SEP measurements. We see also in Figure 68 that P^* agrees well at the tip, within 100 Pa. Referring again to the definition of P^* , we have:

$$P^* = p_s + \frac{1}{2} \rho W^2 - \frac{1}{2} \rho r^2 \omega^2$$

P^* and $r^2\omega^2$ being the same for the flow calculation and the measurements, a lower ρ , explains then a higher W .

By differentiation:

$$W\delta W = \frac{\delta p_s}{\rho}$$

$$\delta W = \frac{\delta p_s}{\rho W}$$

From the results shown in Figures 67 and 71, this gives:

$$\delta W = \frac{250}{1.225 \times 70} = 3 \text{ m/s}$$

And this value corresponds to what we find in Figure 71.

From the exit velocity triangle with large flow angle, we can deduce that this difference should give $(W_{\theta \text{ calculated}} - W_{\theta \text{ measured}})$ close to 2 or 3 m/s, that is also $(V_{\theta \text{ measured}} - V_{\theta \text{ calculated}})$ close to 2 or 3 m/s. And that is what appears in Figure 69.

5.6.2 Loss and work analysis.

As seen in Figure 68, the high losses (low P^*) are mainly found in the tip half of the passage at the blade exit plane, with low loss fluid in the hub half and a thin hub boundary layer.

From Figure 69, we see also that more work ($r\omega V_{\theta}$) is done on the high-loss fluid in the outer half of the passage. Figure 69 also shows that the measured work done is higher than that calculated, and quantitatively we find:

$$(U_2 V_{\theta 2})_{\text{measured}} \cong 95 \times 20$$

whereas:

$$(U_2 V_{\theta 2})_{\text{calculated}} \cong 95 \times (20 - 3)$$

Thus, the work done is less by approximately 15% in the calculation in the outer half of the blade passage, giving a difference of about 10% overall. This explains the results for the overall work done which was calculated to be $\overline{(r_2 V_{\theta 2})}_{\text{calculated}} = 1.18 \text{ m}^2/\text{s}$, compared with a value estimated from the measurements of $\overline{(r_2 V_{\theta 2})}_{\text{measured}} = 1.35 \text{ m}^2/\text{s}$.

Because of the smaller work done in the calculation, but with similar losses, the total pressure rise is also less. In the measurements, at mid-height:

$$\overline{P}_{t(\text{measured, mid-height})} - P_0 = 870 \text{ Pa}$$

and at blade tip:

$$\overline{P}_{t(\text{measured, blade tip})} - P_0 = 1450 \text{ Pa}$$

while in the calculation, at mid-height:

$$\overline{P}_{t(\text{calculated, mid-height})} - P_0 = 870 \text{ Pa}$$

and at blade tip:

$$\overline{P}_{t(\text{calculated, blade tip})} - P_0 = 1220 \text{ Pa}$$

and overall:

$$\overline{\overline{P}}_{t(\text{calculated, overall})} - P_0 = 960 \text{ Pa}$$

5.6.3 Summary.

The analysis and results in this section have shown the significance of the exit static pressure distributions on the work done by the inducer. A possible explanation for the difference in static pressures has been suggested, based on the proximity of the next blade row. It would be useful to try a calculation with both blade rows to verify this argument for δp , or alternatively to compare with measurements for the first blade row alone.

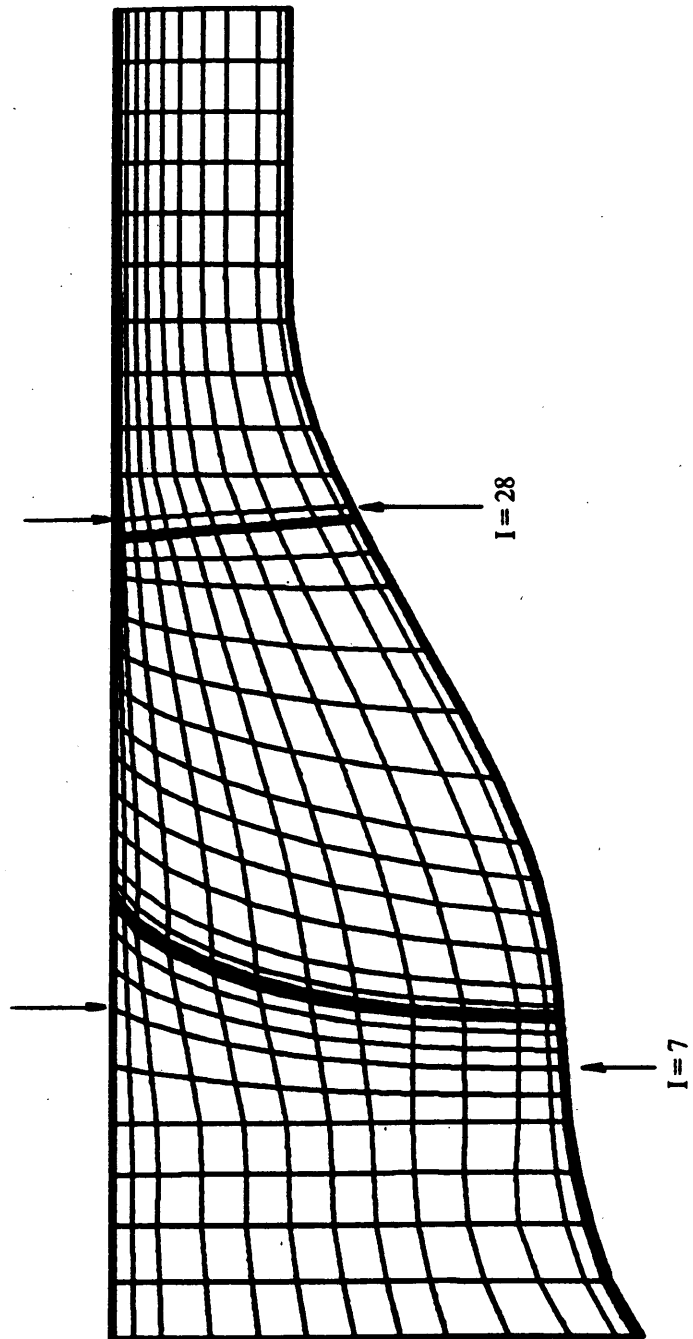


Figure 59. Numerical-experimental comparison: location of the inlet and exit surfaces chosen in the calculation grid.

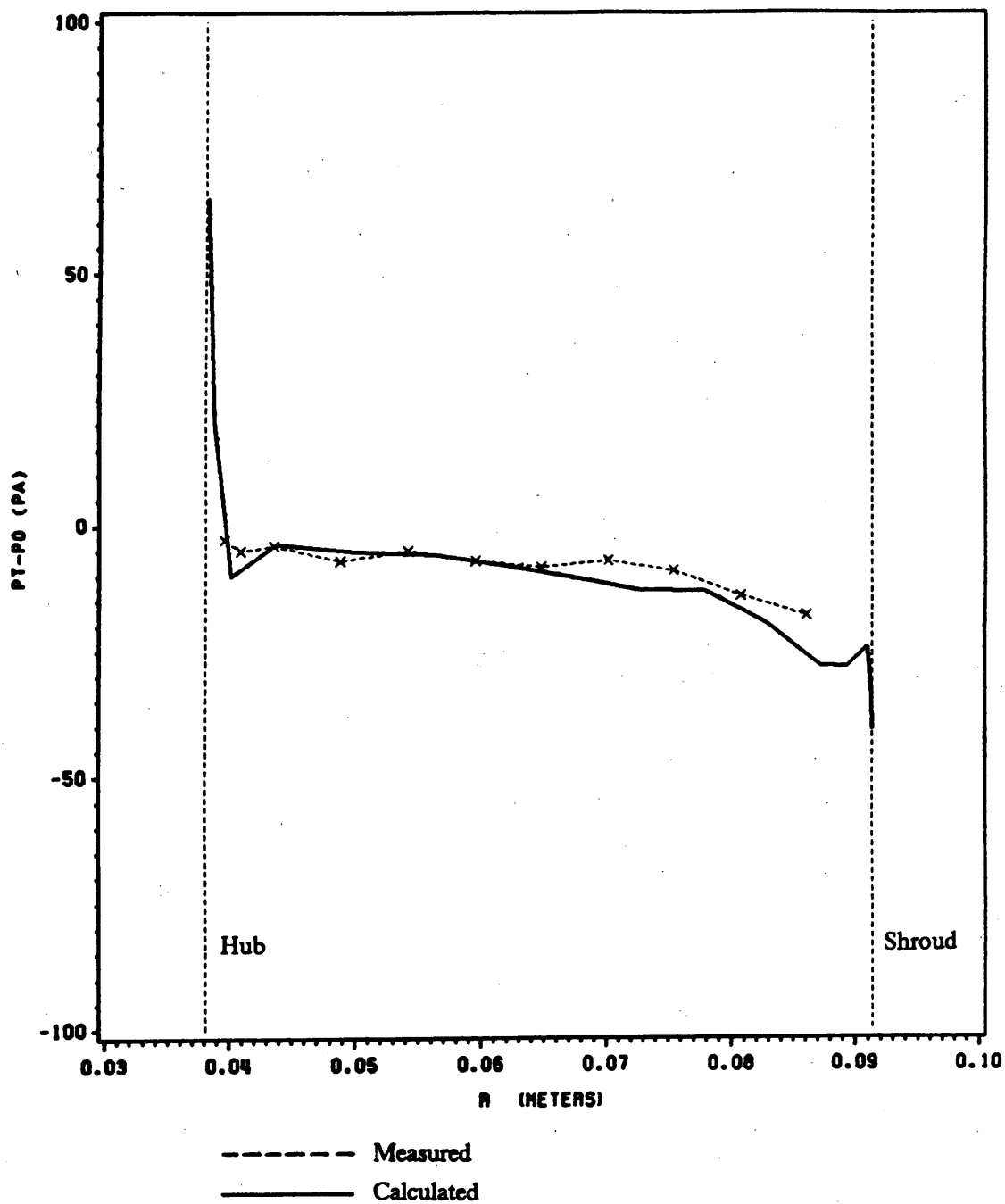


Figure 60. Numerical-experimental comparison; inlet station: P_t

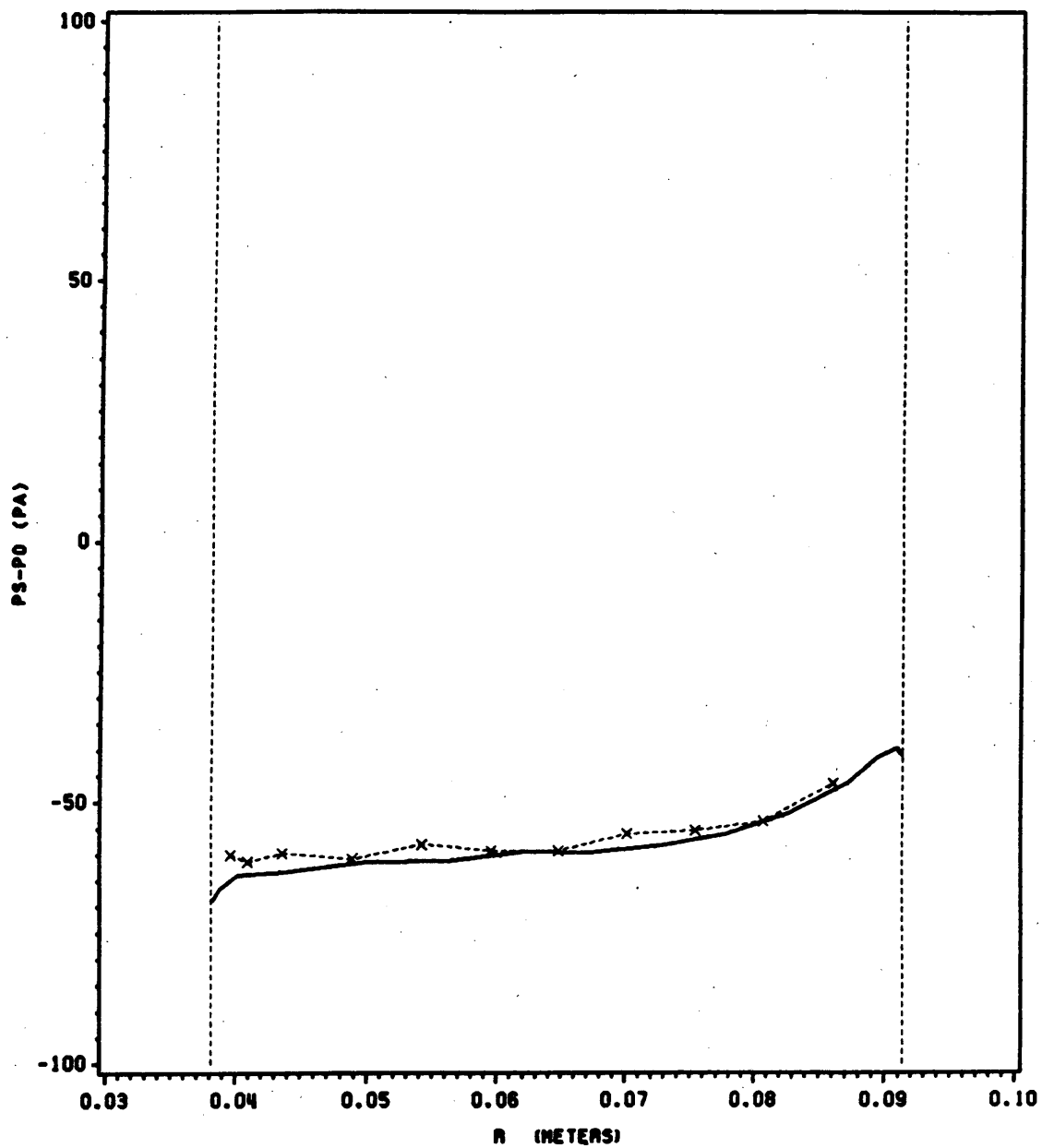


Figure 61. Numerical-experimental comparison; inlet station: p_1

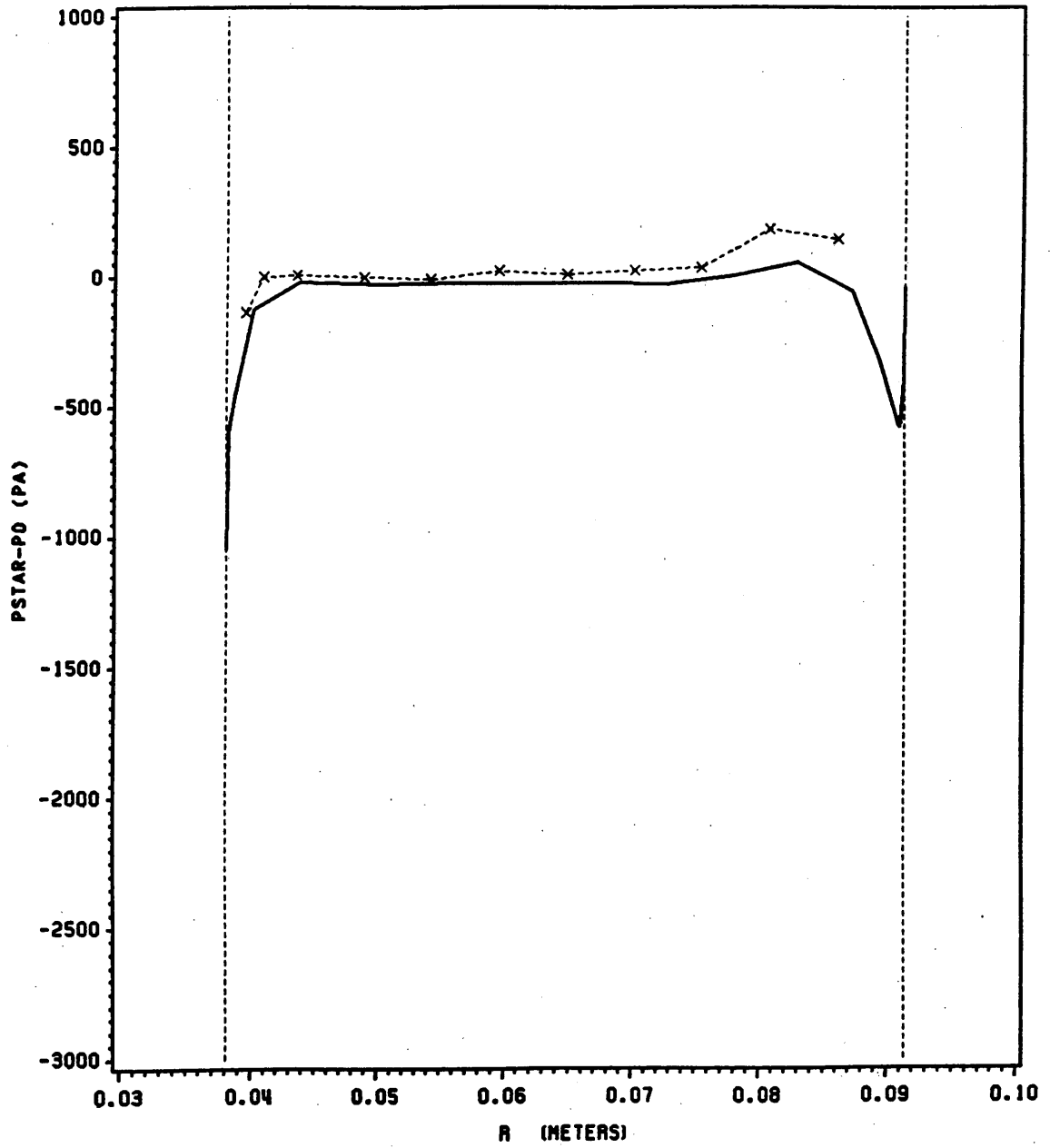


Figure 62. Numerical-experimental comparison; inlet station: P^*

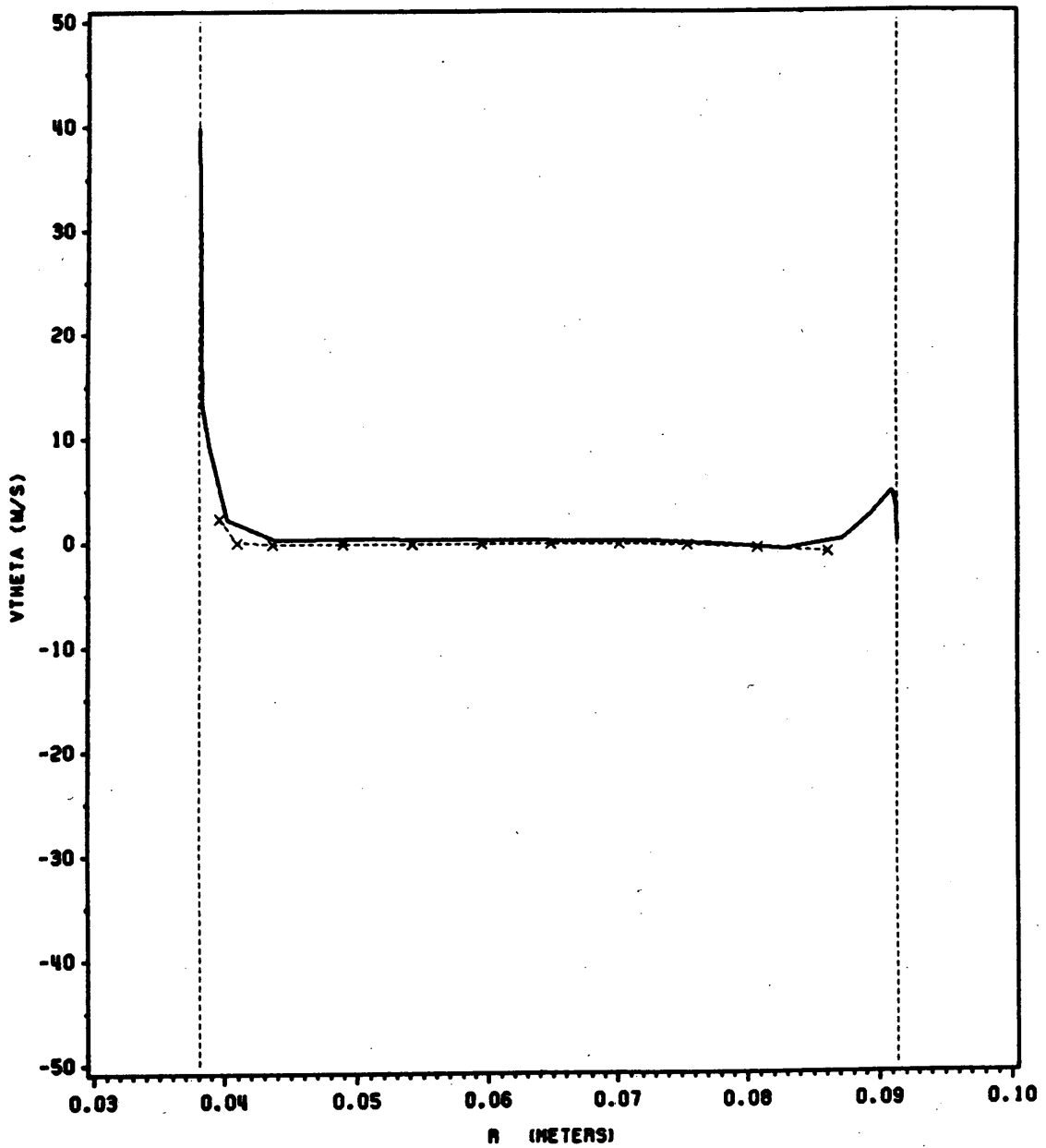


Figure 63. Numerical-experimental comparison; inlet station: V_0

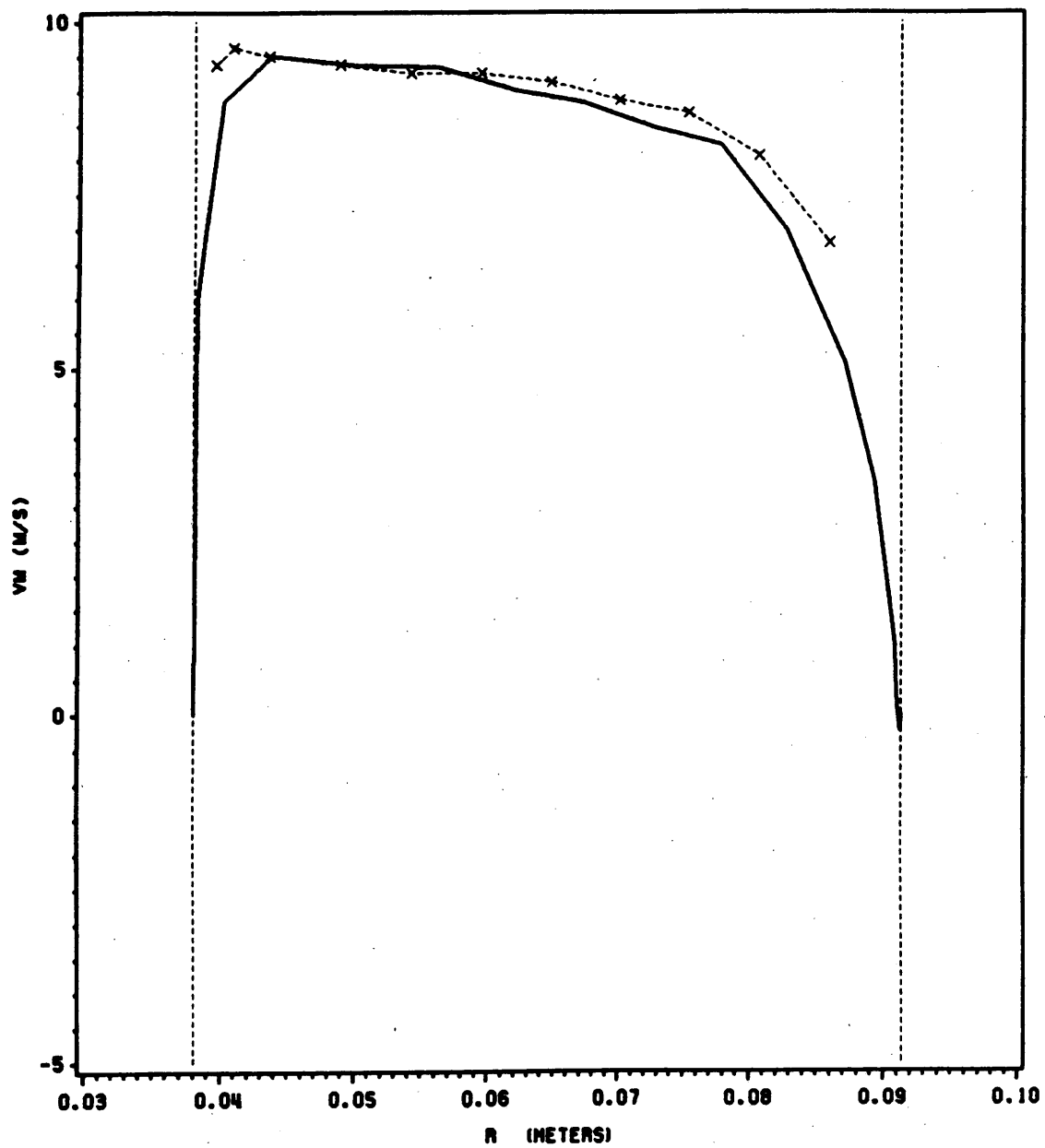


Figure 64. Numerical-experimental comparison; inlet station: V_m

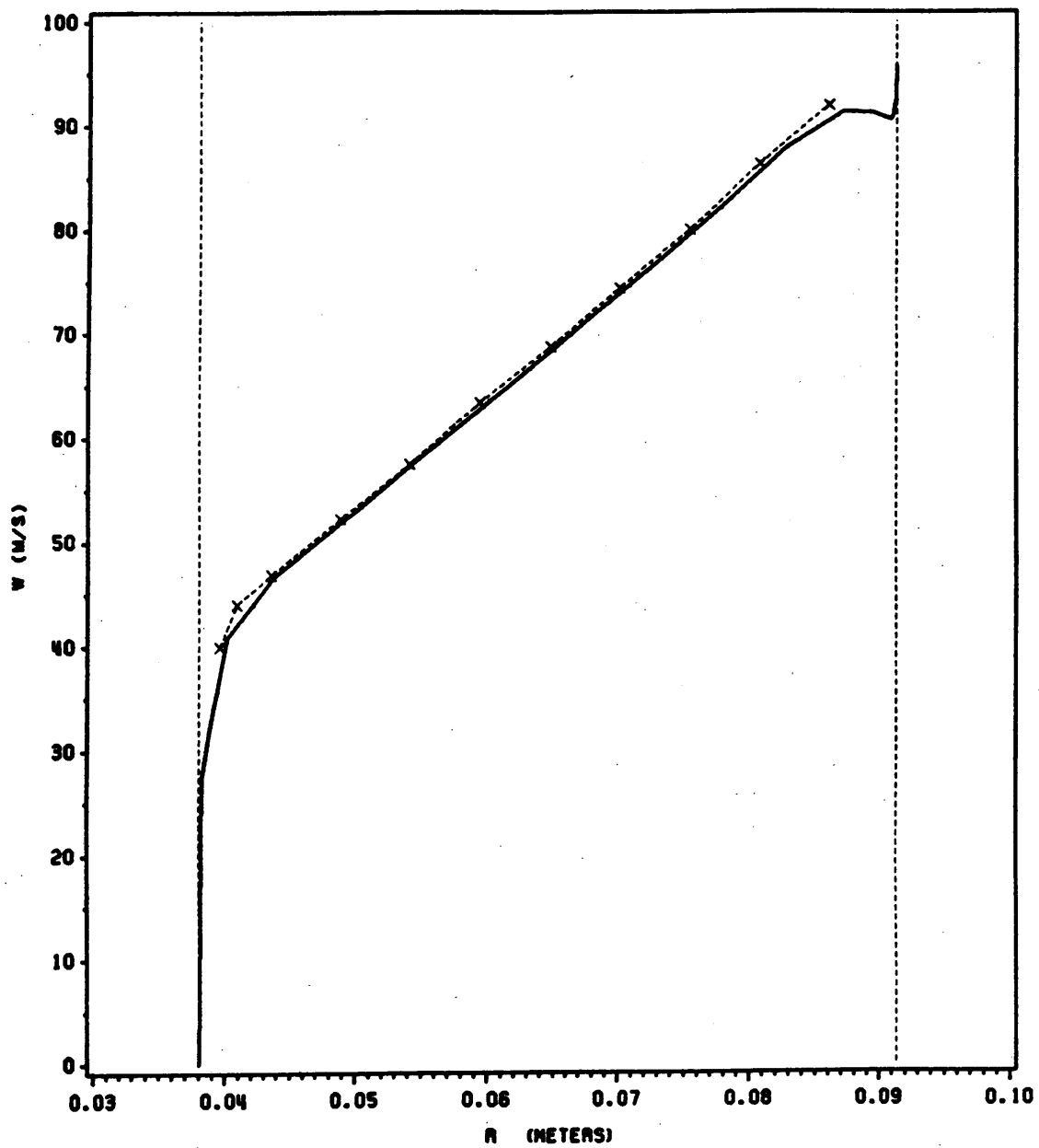


Figure 65. Numerical-experimental comparison; inlet station: W

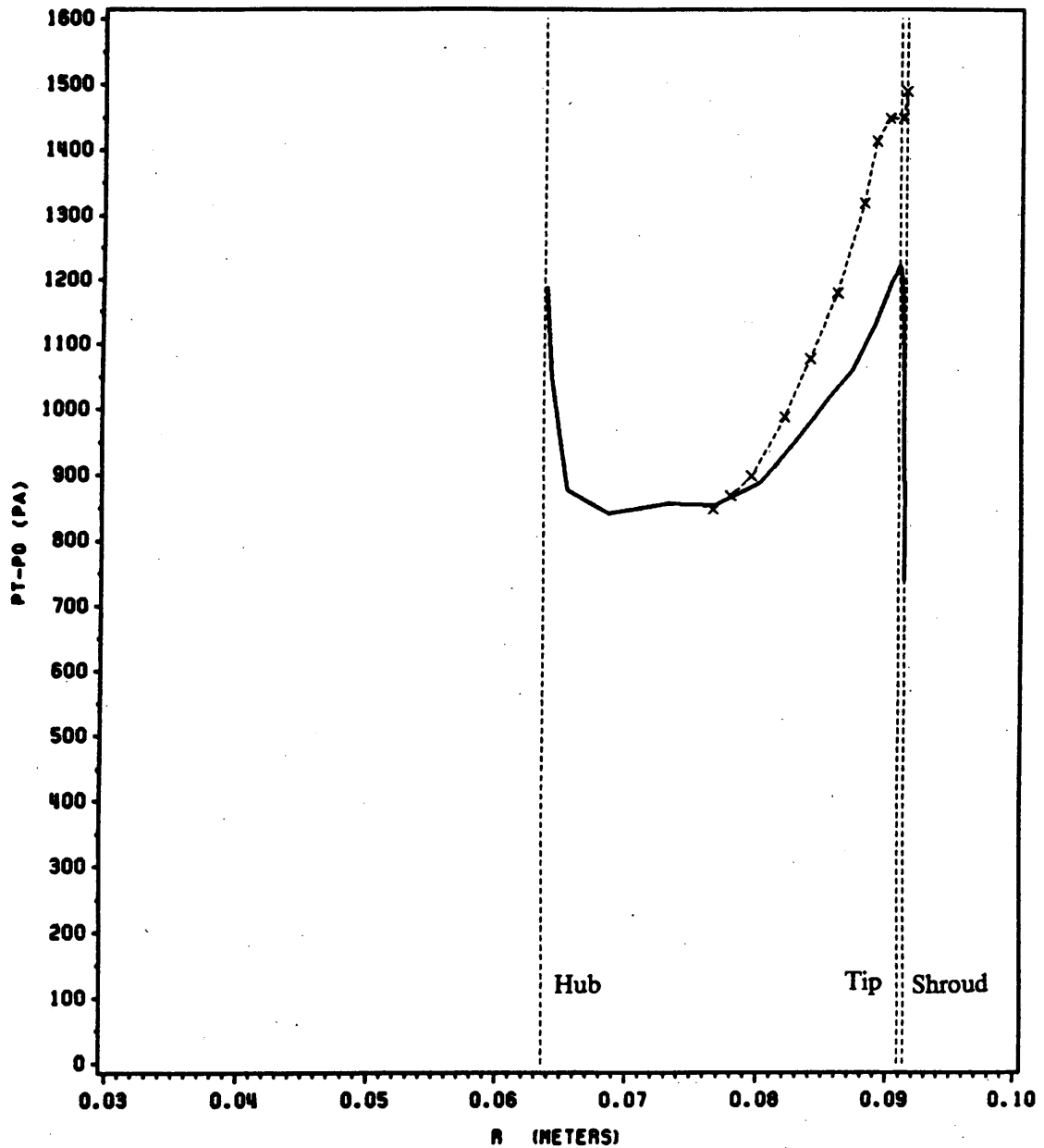


Figure 66. Numerical-experimental comparison; exit station: P_1

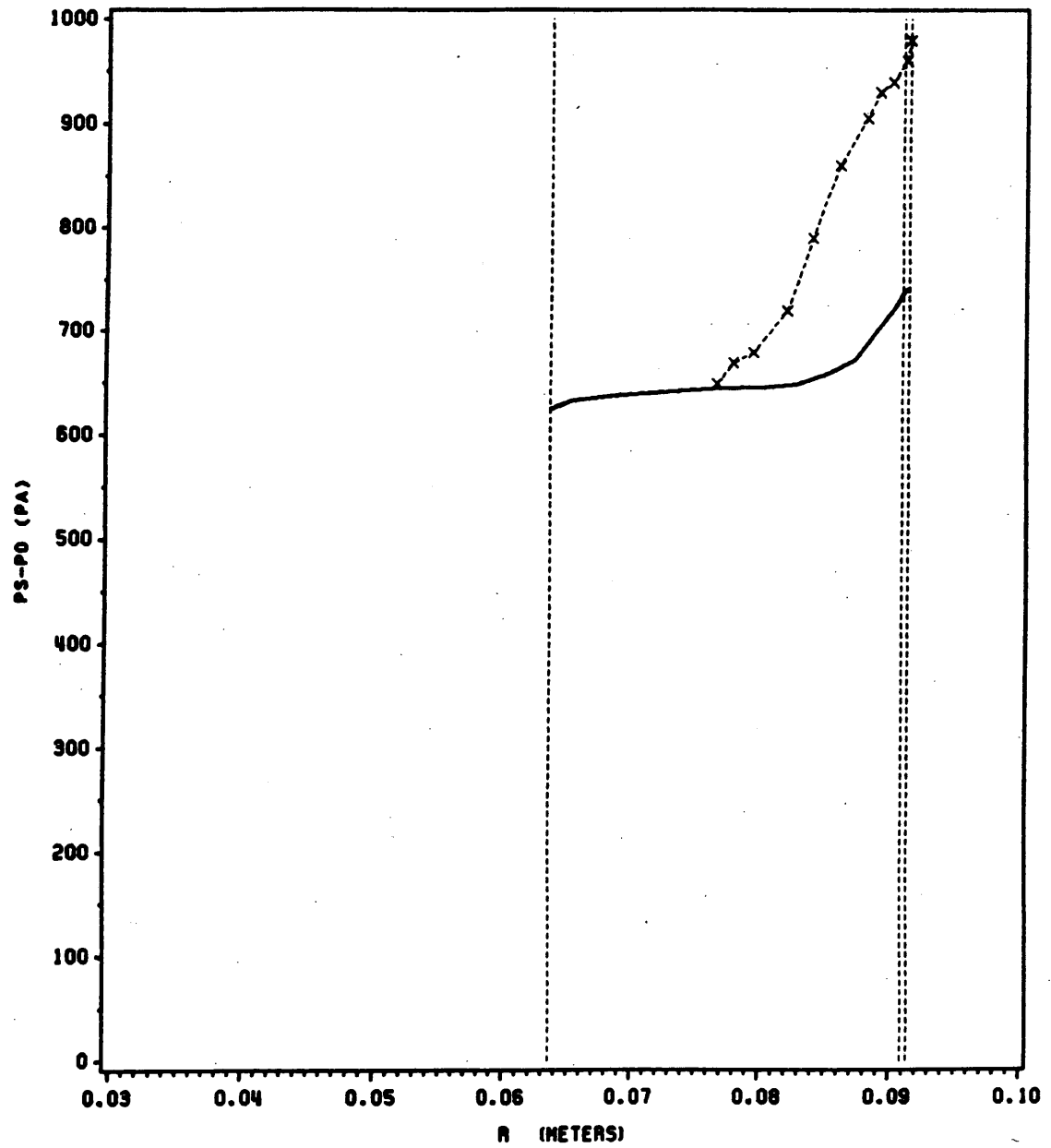


Figure 67. Numerical-experimental comparison; exit station: p_e

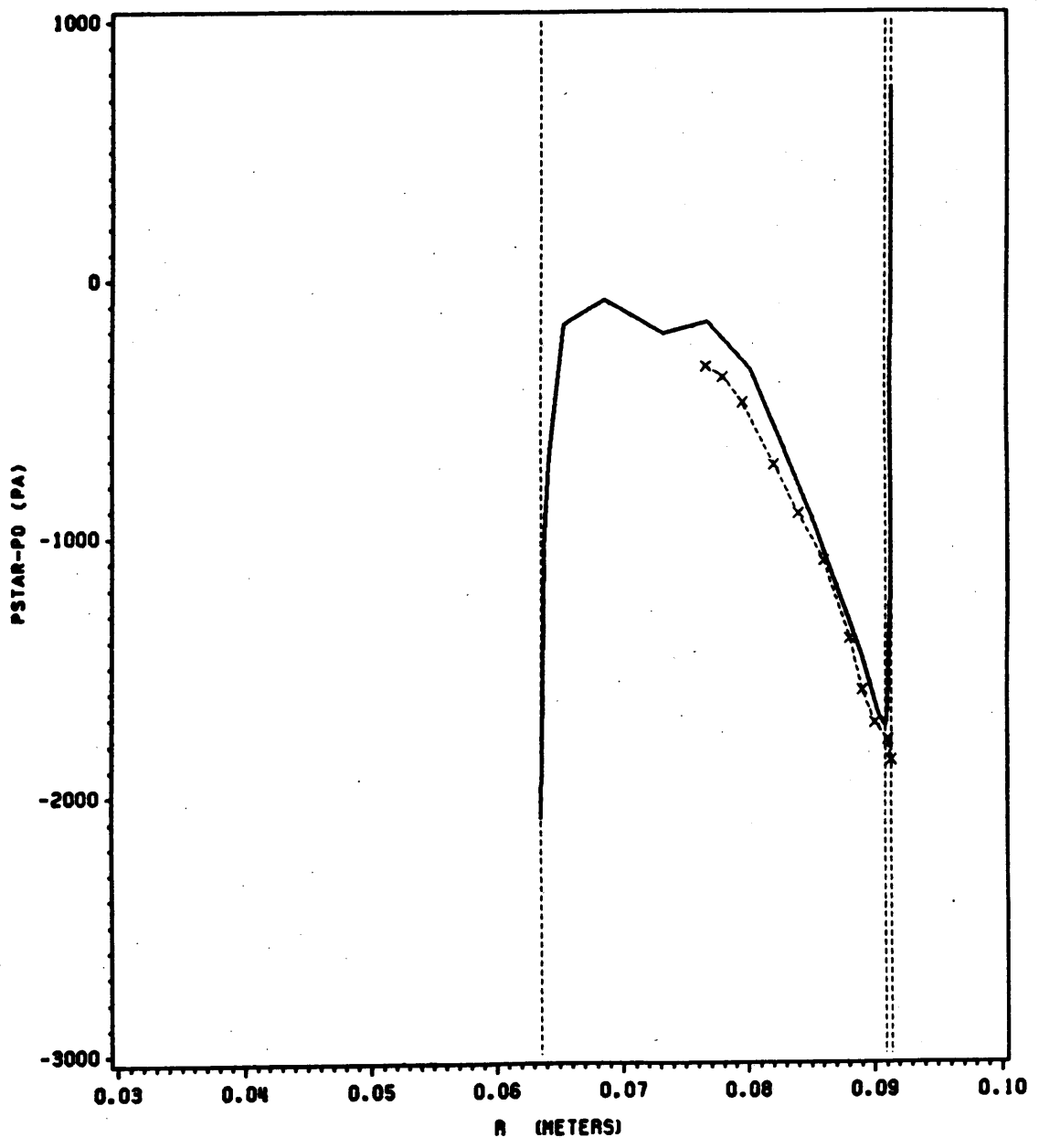


Figure 68. Numerical-experimental comparison; exit station: P^*

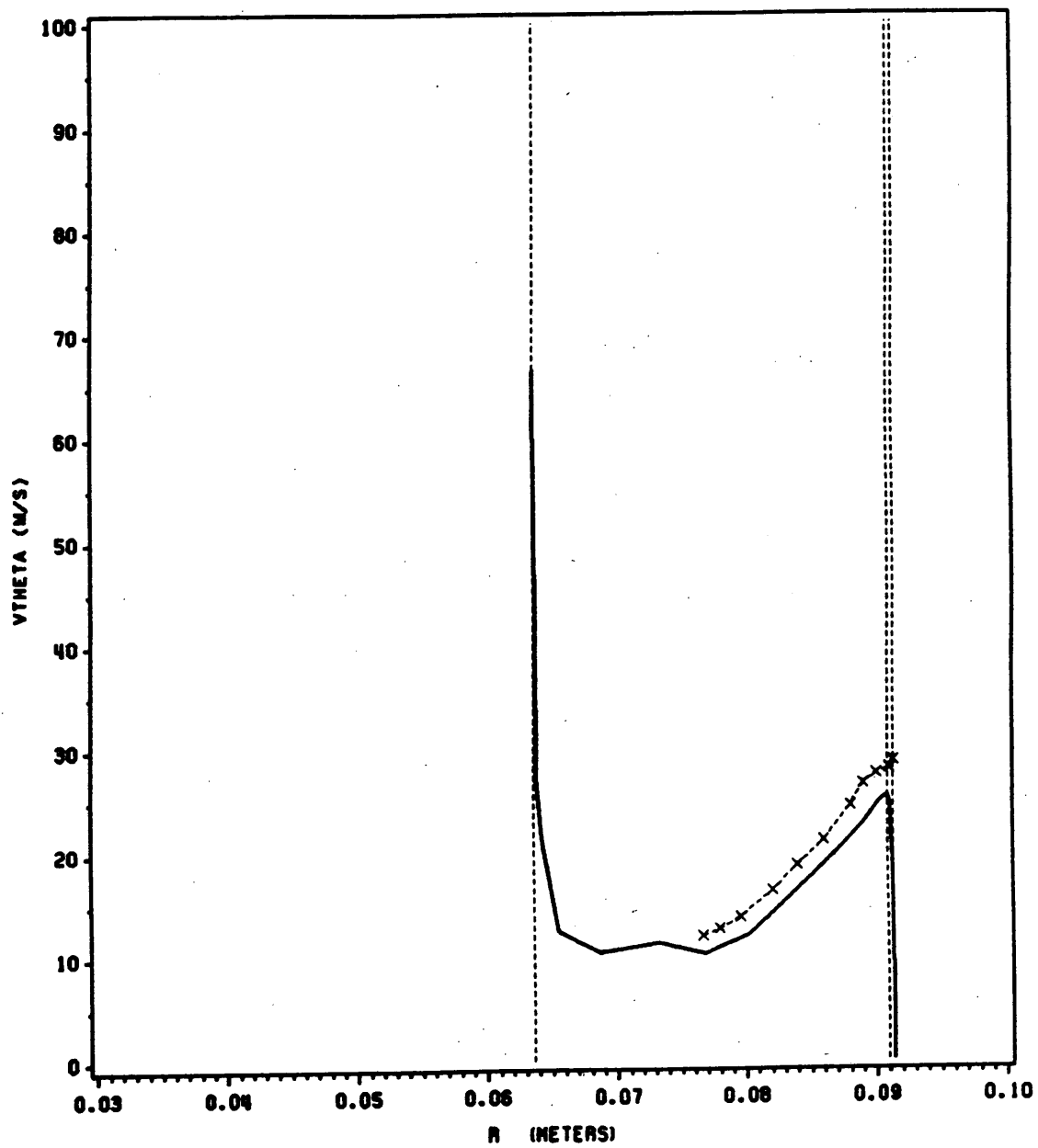


Figure 69. Numerical-experimental comparison; exit station: V_0

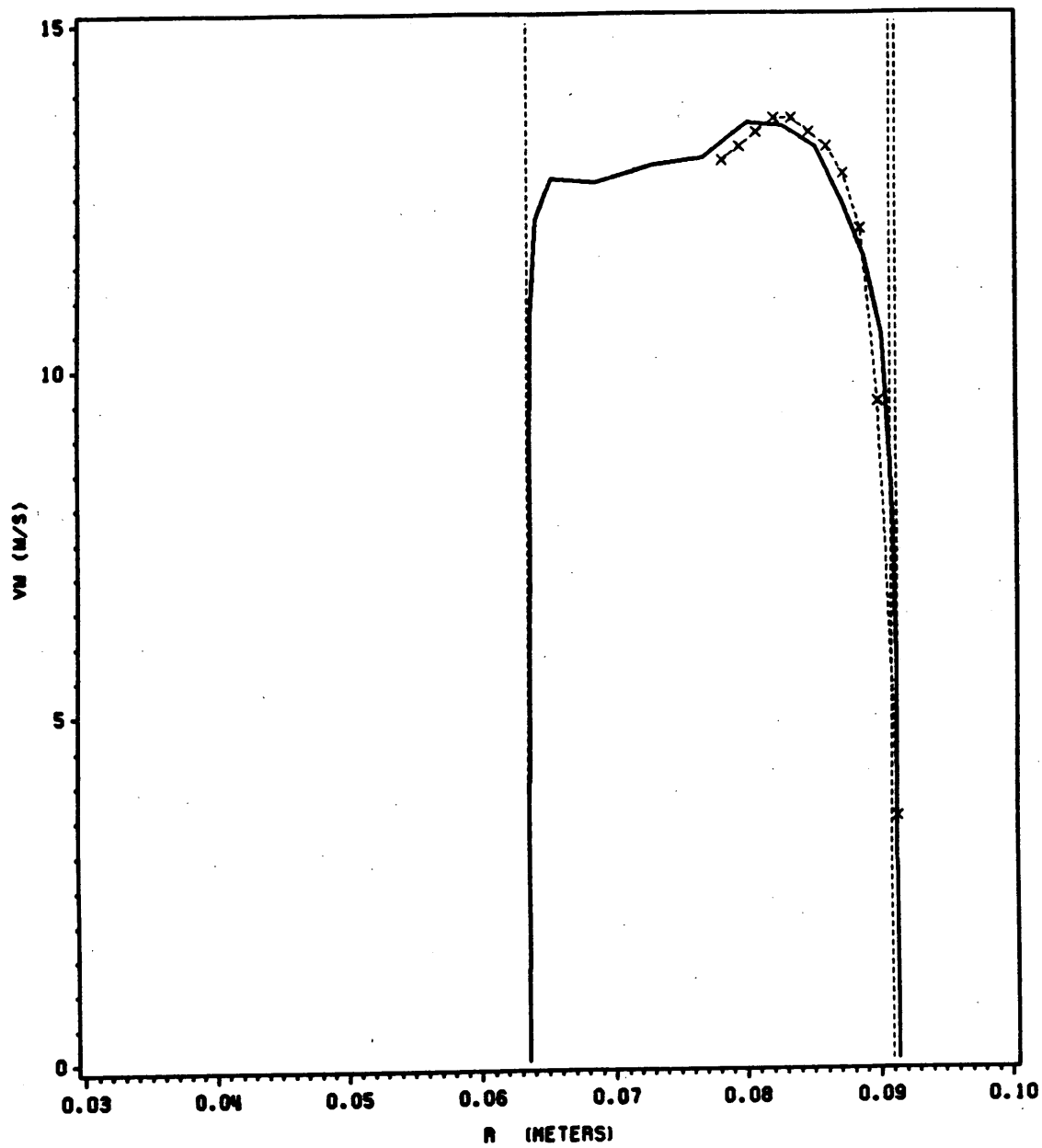


Figure 70. Numerical-experimental comparison; exit station: V_m

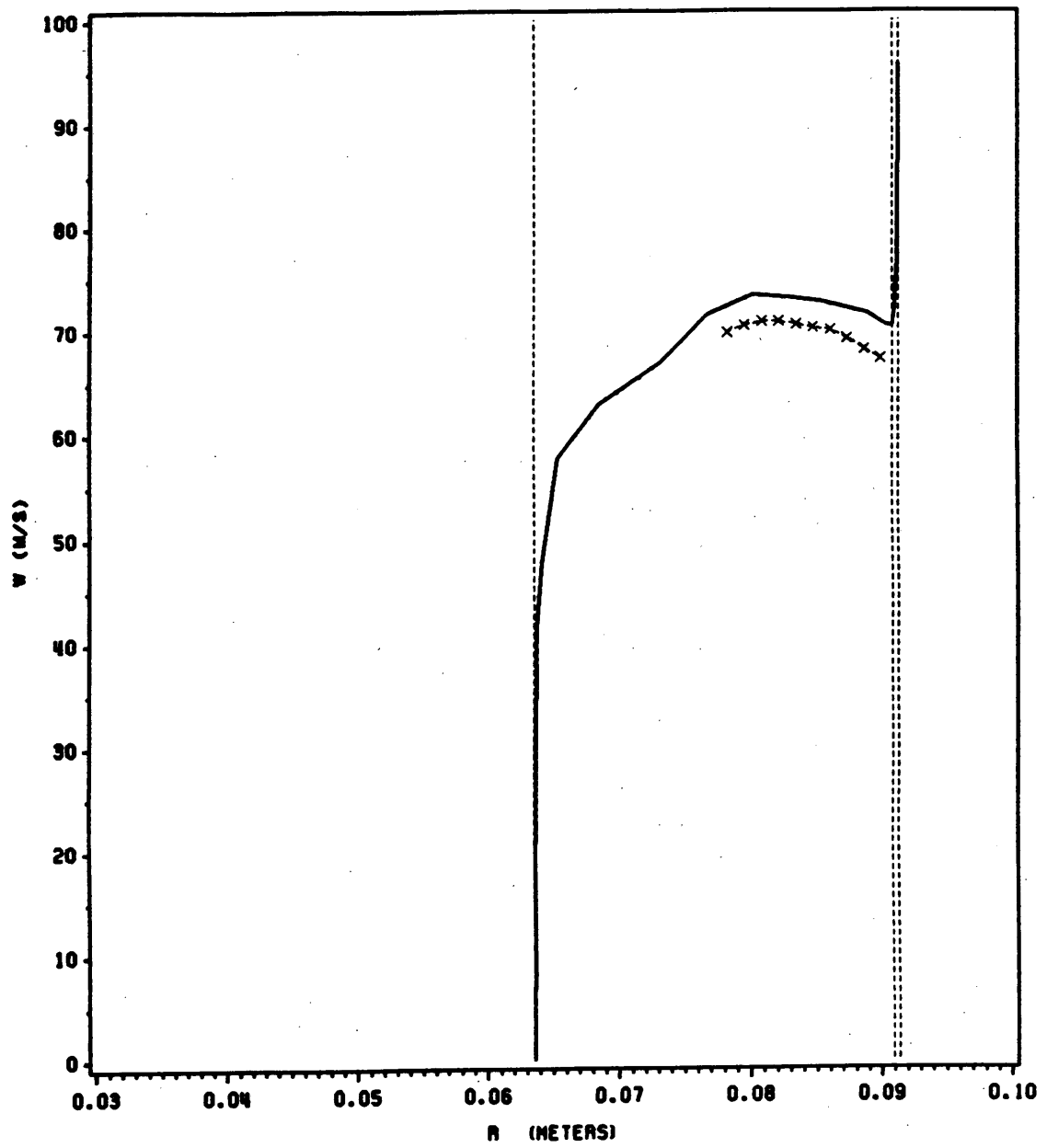


Figure 71. Numerical-experimental comparison; exit station: W

5.7 Loss analysis and comparison with other studies.

In reference 23, Lakshminarayana presents an analytical method to predict inducer performance, based on a modified friction loss coefficient, λ_R (see Section 2.2). We are going to use here the data he used in his article to compare them with our configuration (experimental and numerical results).

The Blasius friction coefficient, λ , is defined by (reference 23):

$$\psi_{loss} = \frac{\lambda}{R_e^{1/4}} \cdot \frac{L}{d_h} \cdot \left(\frac{\overline{W}}{U_{tip}} \right)^2 \quad (5.5)$$

where,

$$R_e = \text{Reynolds number} = \frac{\rho W d_h}{\mu}$$

L = channel length

$$d_h = \text{hydraulic diameter} = \pi r \cos \beta$$

In Figure 72, the radial evolution of this coefficient is plotted for various inducers. The shape of the distribution reflects the increase in losses at the walls, and especially towards the tip (see earlier sections to explain this). The measured and calculated values for the SEP prototype fit well in the range of cases represented.

In Figure 73, a more detailed comparison is proposed between Lakshminarayana (NASA) and SEP (experimental and numerical) inducers. The measured and calculated values of ψ_{loss} agree very well for SEP's prototype, corresponding to the earlier agreement observed for P^* . From 10 to 80% of the passage height, NASA and SEP performances are very close. The boundary layer and tip leakage mixing losses are well modelled with the present Prandtl mixing length model.

The minor discrepancy in the efficiency is mostly a result of the slightly lower calculated work rV_o (discussed in section 5.6, see V_o in Figure 69).

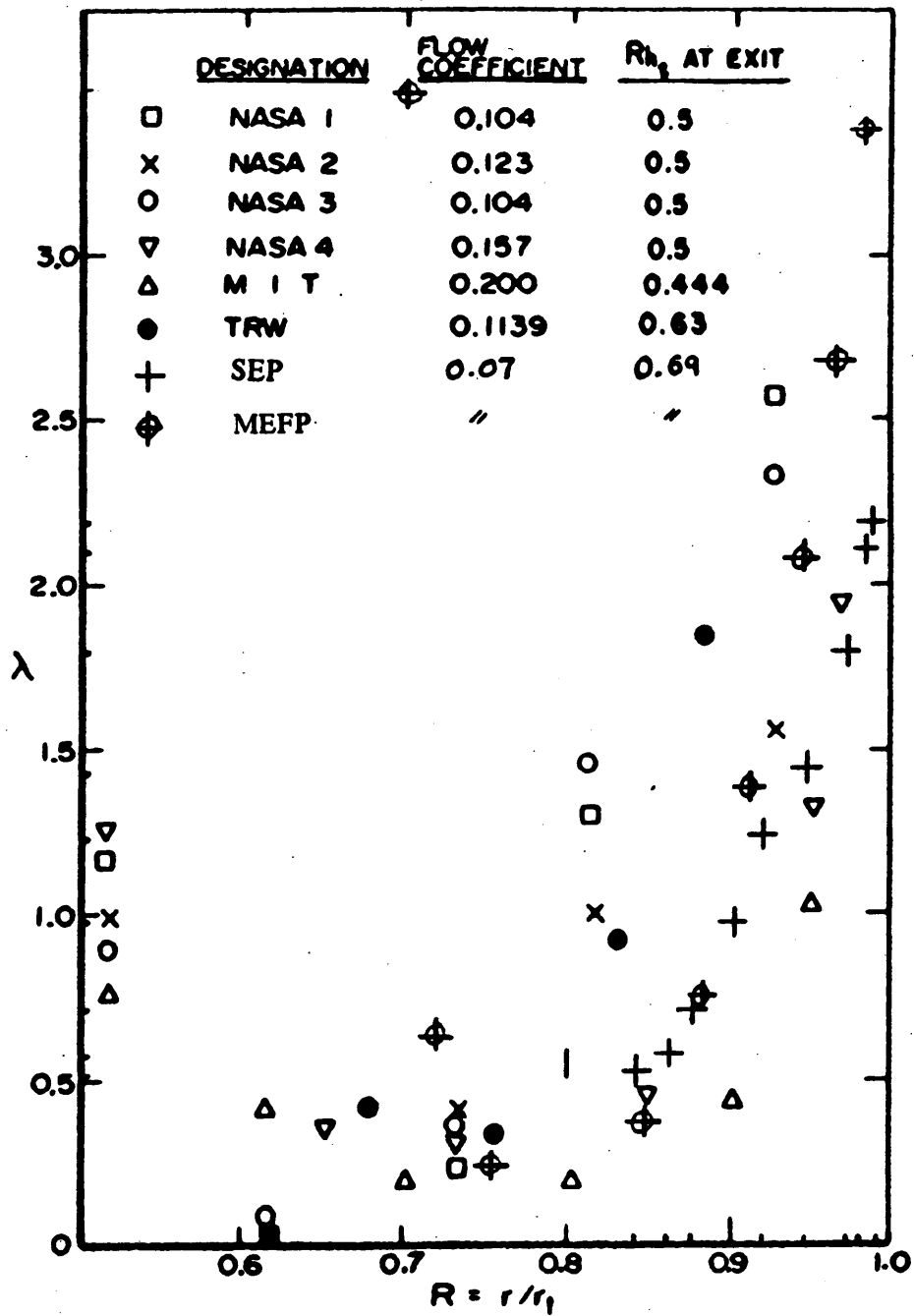
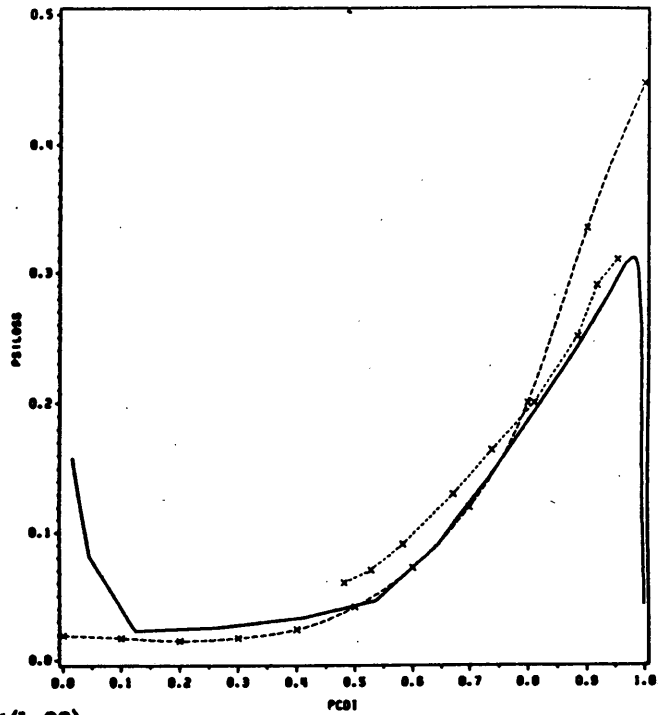


Figure 72. Loss analysis: Blasius friction coefficient λ (Equation 5.5) for various inducer configurations.

RADIAL EVOLUTION LOSS COEFFICIENT, PLANE P11(I=28)

- ×·····× SEP Prototype (Measured).
- SEP Prototype (Calculated).
- ×---× NASA Inducer (Lakshminarayana).

$$PCDI = \frac{r - r_{hub}}{r_{shroud} - r_{hub}}$$



RADIAL EVOLUTION ETA, PLANE P11(I=28)

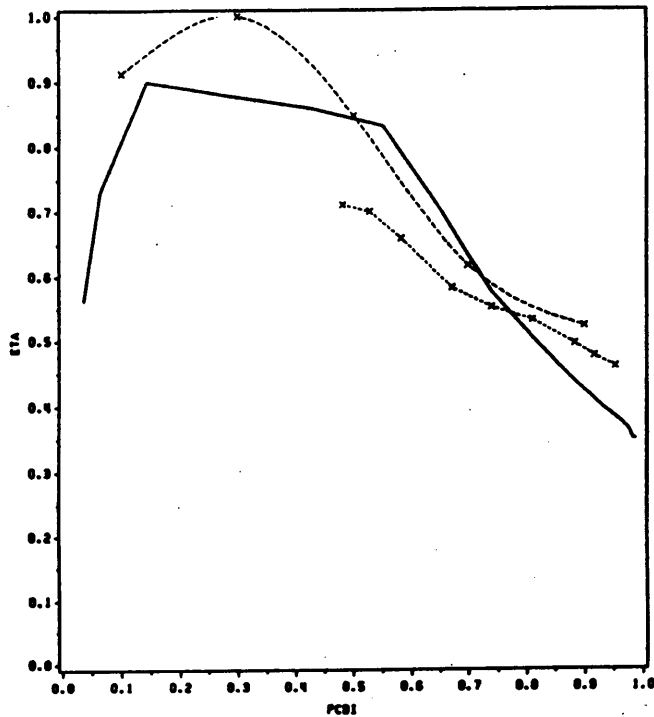


Figure 73. Loss analysis: overall performance; rotary stagnation pressure loss coefficient ψ_{loss} and efficiency η .

6.0 Conclusions.

The flow calculation carried out at VPI&SU and reported here represents one of the most advanced numerical investigations of the flow field in rocket pump inducers. The very high stagger angle and low flow coefficient could be handled by the MEFP code with the use of a carefully chosen calculation grid.

The main expected features of the flow inside the blade passages were resolved, and the most interesting characteristics observed are:

- 1- The tip leakage flow has significant velocities of the order of the blade tip speed.
- 2- The boundary layers that develop on both sides of the blade create centrifuging effects that have been quantitatively studied along the blade chord at mid height (Figure 58). The maximum radial velocities were of the order of 10-20 percent of the blade tip speed.
The tip leakage and boundary layer accumulation combine to create a high-loss region near the shroud.
- 3- The radial inward motions in the core region of the inducer passages are of the same order of magnitude as the boundary layer flows, and extend from shroud to hub.
- 4- A circumferential vortex is found at the inducer inlet near the junction of the swept leading edge and the stationary shroud wall. It is explained by the high flow stagger angle (with 3 deg incidence at the tip) and the low flow coefficient, and is fed by leakage flow with a strong reverse flow component in the axial direction.

5- Cavitation inception in the LH₂ pump is also qualitatively predicted from the air flow calculation, using a simplified analogy. Critical static pressure contours were calculated along the leading edge, from mid-height to tip, on the suction side; they were also found in the tip corner region of the leading edge. These two regions correspond to the results observed in cavitation visualizations.

The low pressure regions are of primary interest to the inducer designer, since the function of this element is to control cavitation upstream of the rest of the pump.

The comparison of the 3-D flow calculation results shows very good agreement with available experimental data. The radial distributions of total pressure loss compare very well, justifying the use of a Prandtl mixing length model for this turbulent flow calculation. The static pressure at the inducer exit is the only parameter showing significant discrepancy. Since the calculated static pressures are in agreement with radial equilibrium, this discrepancy can be explained by the presence of the inducer second blade row in the air tests. A quantitative appreciation of this effect could be gained by including the second row in a future flow calculation, or also by conducting air tests with only the first blade row.

These encouraging results represent a major step forward in the understanding of the inducer flow field. They also constitute an important reference source for future calculations of this type.

Bibliography

1. Thornycroft, Sir John, and Barnaby, S. W., "Torpedo Boat Destroyers," *Minutes of Proc. Inst. of Civil Engineers*, 122, 51-103, 1895.
2. Rayleigh, Lord (Strutt, John William), "On the Pressure Developed in a Liquid During the Collapse of a Spherical Cavity," *Phil. Mag.*, 34, 94-98, August 1917.
3. Knapp, Robert T.; Daily, James W.; and Hammit, Frederick G., "Cavitation," *Mc Graw-Hill Book Company*, 1970.
4. Stripling, L. B., and Acosta, A. J., "Cavitation in Turbopumps, Part 1 and Part 2," *Transactions of the ASME, Ser.D, Journal of Basic Engineering*, Vol.84, No.3, pp.326-350, Sept.1962.
5. Meng, Phillip R., and Moore, Royce D., "Cavitation Performance of an 80.6 deg. Helical Inducer in Liquid, Hydrogen" *NASA TMX-1808, NASA STAR Index N69-27841*, June 1969.
6. Meng, Phillip R., and Moore, Royce D., "Cavitation Performance of Line Mounted 80.6 deg. Helical Inducer in Hydrogen," *NASA TMX-1854, NASA STAR Index N69-33261*, August 1969.
7. Meng, Phillip R., and Moore, Royce D., "Hydrogen Cavitation Performance of 80.6 deg. Helical Inducer Mounted in Line with Stationary Centerbody," *NASA TMX-1935, NASA STAR Index N70-16723*, January 1970.

8. Meng, Phillip R., and Moore, Royce D., "Thermodynamic Effects of Cavitation of an 80.6 deg. Helical Inducer Operated in Hydrogen," *NASA TN D-5614, NASA STAR Index N70-17604*, January 1970.
9. Ruggieri, Robert S., and Moore, Royce D., "Method for Prediction of Pump Cavitation Performance for Various Liquids, Liquid Temperatures, and Rotative Speeds," *NASA TN D-5292*, 1969.
10. Moore, Royce D., and Meng, Phillip R., "Comparison of Noncavitation and Cavitation Performance for 78, 80.6 and 84 deg. Helical Inducers Operated in Hydrogen," *NASA TN D-6361, NASA STAR Index N71-25940*, May 1971.
11. Shuba, B. H., "An Investigation of Tip-Wall Vortex Cavitation in an Axial-Flow Pump," *Pennsylvania State Univ., Applied Research Lab., AD-A134357 (Contract N00024-79-C-6043), NASA STAR Index N84-16496*, May 1983.
12. Acosta, A. J., "Cavitation Inception, Final Report (1 Oct. 1974 - 30 Sept. 1984)," *California Institute of Technology, AD-A159297 (Contract N00014-75-C-0378), NASA STAR Index N86-14537*, March 1985.
13. Oliveri, S., "Etude Bibliographique sur: les Effets Thermodynamiques en Cavitation," *Institut National Polytechnique de Grenoble, France*, May 1986.
14. Rowe, A., "Etude Synthetique du Probleme de la Modelisation des Ecoulements Partiellement Cavitants," *Centre de Recherche et d'Essais de Mahines Hydrauliques de Grenoble, France*, 1988.
15. Cooper, P., "Analysis of Single- and Two-Phase Flows in Turbopump Inducers," *Trans. of the ASME, Journal of Engineering for Power*, pp.577-588, October 1967.
16. Brophy, Michael C.; Stinebring, David R.; and Billet Michael L., "A Study of Pump Cavitation Damage," *NASA CR No. NAS8-34535, NASA STAR Index N84-20783*, November 1983.
17. Schultz, J. L., "Modelisation de la Cavitation Partielle Dans les Pompes," *These de Docteur de l'Institut National Polytechnique de Grenoble, France*, 1988.
18. Acosta, A. J., "An Experimental Study of Cavitating Inducers," *Proceedings of Second Symposium on Naval Hydrodynamics, Washington, D.C.*, pp.533-557, August 1958.

19. Soltis, R. F.; Anderson, D. A.; and Sandercock, D. M., "Investigation of the Performance of a 78 deg. Flat Plate Helical Inducer," *NASA TN D-1170*, March 1962.
20. King, J. A., "Testing Pumps in Air," *Transactions of the ASME, Journal of Engineering for Power, Vol.90, pp.97-105*, April 1968.
21. Lakshminarayana, B., "Visualization of Flow in Axial-Flow Inducers," *Transactions of the ASME, Journal of Basic Engineering, Vol.94*, December 1972.
22. Lakshminarayana, B., "Three Dimensional Flow Field in Rocket Pump Inducers, Part 1: Measured Flow Field Inside the Rotating Blade Passage and at the Exit," *Transactions of the ASME, Journal of Fluids Engineering, pp.567-578*, December 1973.
23. Lakshminarayana, B., "Experimental and Analytical Investigation of Flow Through a Rocket Pump Inducer," *Fluid Mechanics Design, and Acoustics of Turbomachinery, NASA SP 304, Part 2*, 1974.
24. Lakshminarayana, B., "Analytical and Experimental Study of Flow Phenomena in Noncavitating Rocket Pump Inducers," *NASA Contractor Report 3471*, October 1981.
25. Lakshminarayana, B., "Fluid Dynamics of Inducers - A Review," *Transactions of the ASME, Journal of Fluids Engineering, Vol.104, pp.411-427*, December 1982.
26. Bario, F.; Barral, L.; and Bois, G., "Air Test Flow Analysis of the Hydrogen Pump of VULCAIN Rocket Engine," *Pumping Machinery-1989, FED, Vol.81*, July 9-12 1989.
27. Katsanis, T., "Use of Arbitrary Quasi-Orthogonals for Calculating Flow Distribution in the Meridional Plane of a Turbomachine," *NASA TN D-2546, NASA STAR Index N65-12306*, September 1964.
28. Katsanis, T., "Use of Arbitrary Quasi-Orthogonals for Calculating Flow Distribution on a Blade-to-Blade Surface in a Turbomachine," *NASA TN D-2809, NASA STAR Index N65-23168*, March 1965.

29. Cooper, P.; and Bosch, H. B., "Three-Dimensional Analysis of Inducer Fluid Flow," *NASA CR No. 54836, NASA STAR Index N66-22266*, February 1966.
30. Lakshminarayana, B.; and Gorton, C. A., "Three Dimensional Flow Field in Rocket Pump Inducers, Part 2: Three Dimensional Viscid Flow Analysis and Hot Wire Data on Three Dimensional Mean Flow and Turbulence Inside the Rotor Passage," *Transactions of the ASME, Journal of Fluids Engineering, Vol.99, Ser.I, No.1, pp.176-186*, March 1977.
31. Poncet, A.; and Lakshminarayana, B., "Investigation of Three Dimensional Flow Characteristics in a Three Bladed Rocket Pump Inducer," *NASA Contractor Report 2290*, 1973.
32. Moore, J.G., et al., "Numerical Methods for Flows in Turbomachine Bladings," *Von Karman Institute For Fluid Dynamics, AGARD Lecture Series 1982-05*, April 26-30, 1982.
33. Moore, J.G., "An Elliptic Calculation Procedure for 3-D Viscous Flow," *AGARD Lecture Series No.140 on 3-D Techniques Applied to Internal Flows in Propulsion Systems, Rome, Italy, Cologne, West Germany, Paris, France*, June 1985.
34. Moore, J., "Performance Evaluation of Flow in Turbomachinery Blade Rows," *AGARD Lecture Series No.140, (loc. cit.)*.
35. Moore, J.; and Moore, J.G., "Secondary Flow, Separation and Losses in the NACA 48-Inch Centrifugal Impeller at Design and Off-Design Conditions," *ASME Gas Turbine and Aeroengine Congress, Amsterdam, The Netherlands*, June 6-9, 1985.
36. Bejan, A., "Convection Heat Transfer," *John Wiley & Sons*, 1984.
37. Moses, H.L., "Lecture Notes on Turbomachinery," *Mechanical Engineering Department, Virginia Polytechnic Institute and State University, Blacksburg, Virginia, 24061*.
38. Schlichting, "Boundary Layer Theory," *Mc Graw - Hill Book Company, Inc.*, 1960.
39. Moore, J., "Lecture Notes on 3-D Flows in Turbomachinery Blade Rows," *Prepared for Presentation at the ASME Gas Turbine Division Short Course on:*

3-D Flows in Turbomachinery Blade Rows - Physics, Numerical Methods, and Application, 30th International Gas Turbine Conference, January 1985.

40. Desclaux, J., "Personal Communication," July 1989.

Appendix A. MEFP Format Specifications.

B. GEOMETRY - SETTING UP THE MASTER GEOMETRY GRID

Input Format

The format for the master geometry grid input data is as follows.

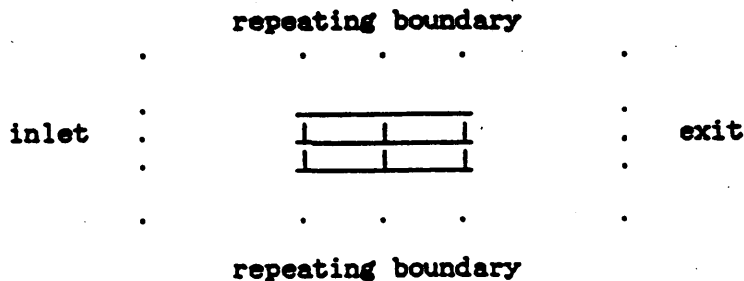
Input Variables	Format
(COMENT(I), I=1, 20)	20a4
IG, JG, KG, LCOOR	*
(B(J), J=1, JG), (C(K), K=1, KG)	*
read next line I=1, IG or til end of data set	
A(I), ((LT(I, J, K), (XYZ(L, I, J, K), L=1, 3), J=1, JG), K=1, KG)	*

where:

COMENT - 1 line comment to identify data set
IG = number of grid points in i direction
JG = number of grid points in j direction
KG = number of grid points in k direction
LCOOR = 1 for x, y, z coordinates
 = 2 for r, θ , z coordinates
B (j) = reference locations for the grid points in the j direction
C (k) = reference locations for the grid points in the k direction
A (i) = reference locations for the grid points in the i direction
LT (i, j, k) - grid point type
 = 1 flow point
 = 2 flow point
 = 3 wall rotating with coordinate system
 = 4 stationary wall
 = 5 solid point - no flow
XYZ (L, i, j, k) - grid point coordinates. L=1, r or x; L=2,
 y or θ ; L=3, z.

Simple Example

Consider a cascade of rectangular objects.



The master geometry grid input data is:

CASCADE OF RECTANGULAR OBJECTS FOR 3-D FLOW
 5 5 3 1
 -1 0. .5 1. 2. 0. .5 1.
 -1. 3 0. 0. 0. 3 0. .5 0. 3 0. .75 0. 3 0. 1. 0. 3 0. 1.5 0.
 1 0. 0. .3 1 0. .5 .3 1 0. .75 .3 1 0. 1. .3 1 0. 1.5 .3
 3 0. 0. .6 3 0. .5 .6 3 0. .75 .6 3 0. 1. .6 3 0. 1.5 .6
 0. 3 1.0 0. 0. 3 1.0 .5 0. 3 1.0 .75 0. 3 1.0 1. 0. 3 1.0 1.5 0.
 1 1.0 0. .3 3 1.0 .5 .3 3 1.0 .75 .3 3 1.0 1. .3 1 1.0 1.5 .3
 3 1.0 0. .6 3 1.0 .5 .6 3 1.0 .75 .6 3 1.0 1. .6 3 1.0 1.5 .6
 .5 3 1.5 0. 0. 3 1.5 .5 0. 5 1.5 .75 0. 3 1.5 1. 0. 3 1.5 1.5 0.
 1 1.5 0. .3 3 1.5 .5 .3 5 1.5 .75 .3 3 1.5 1. .3 1 1.5 1.5 .3
 3 1.5 0. .6 3 1.5 .5 .6 5 1.5 .75 .6 3 1.5 1. .6 3 1.5 1.5 .6
 1. 3 2.0 0. 0. 3 2.0 .5 0. 3 2.0 .75 0. 3 2.0 1. 0. 3 2.0 1.5 0.
 1 2.0 0. .3 3 2.0 .5 .3 3 2.0 .75 .3 3 2.0 1. .3 1 2.0 1.5 .3
 3 2.0 0. .6 3 2.0 .5 .6 3 2.0 .75 .6 3 2.0 1. .6 3 2.0 1.5 .6
 2. 3 3.0 0. 0. 3 3.0 .5 0. 3 3.0 .75 0. 3 3.0 1. 0. 3 3.0 1.5 0.
 1 3.0 0. .3 1 3.0 .5 .3 1 3.0 .75 .3 1 3.0 1. .3 1 3.0 1.5 .3
 3 3.0 0. .6 3 3.0 .5 .6 3 3.0 .75 .6 3 3.0 1. .6 3 3.0 1.5 .6

Right-Hand System

The i, j and k grid directions do not need to be orthogonal or even smooth. However, they must form a right handed grid system with i cross j having a positive component in the k direction.

Coordinates

The master geometry grid may be specified in either x,y,z coordinates or r,θ,s coordinates. When a rotating reference frame is desired (rotors) r,θ,s coordinates must be used; rotation is about the z axis. When a repeating boundary is used, the repeat must occur in the y or θ direction.

A, B and C

The reference parameters A, B and C are used for interpolation. The calculation grid is chosen by specifying values for A, B and C. If these do not fall on master geometry grid points, MEFP uses A, B and C to linearly interpolate x, y and z or r, θ and s to locate the points. A, B and C are also used to linearly interpolate the velocity, etc. onto a new grid when the grid is changed. It is helpful if A, B and C are roughly proportional to distance in the i, j and k directions.

Appendix B. 2-D Calculation Conditions.

1. General conditions of study.
2. Blade-to-blade calculation.
3. Meridional calculation.
4. 3-D calculation grid.

B.1 General conditions of study.

The medium is air, considered as incompressible.

$$\rho = 1.225 \text{ kg/m}^3$$

$$P_0 = 1 \text{ atm} = 101,325 \text{ Pa}$$

$$T_0 = 288.15 \text{ K}$$

The dynamic viscosity μ_0 is evaluated by the expression (function in the MEFP program):

$$\mu_0 = 4 \times 10^{-7} (T)^{0.68}$$

At $T = 288.15 \text{ K}$, we find:

$$\mu_0 = 1.882 \cdot 10^{-5} \text{ kg/ms}$$

The mass flow rate is:

$$Q_{\text{air}} = 0.2109 \text{ kg/s}$$

The rotation speed is:

$$N = 10,000 \text{ RPM}$$

The flow coefficient is:

$$\phi = 0.07$$

The Reynolds number based on the tip speed is:

$$Re = \frac{\rho U_{\text{tip}} D}{\mu} = 1.1 \times 10^6$$

B.2 Blade-to-blade calculation (in the tip section).

B.2.1 Final grid spacing.

The grid size retained for this calculation is:

$$I \times J \times K = 37 \times 15 \times 2$$

(Note: the MEFP procedure requires each index number to be greater than or equal to 2 (it is a 3-D procedure)).

The grid spacing, in terms of A's, B's and C's (see figure 22), is reproduced below, and Figure 27 shows the resulting representation.

INDUCER TIP SECTION GRID									
A 37									
-1.00000	-0.90000	-0.80000	-0.70000	-0.60000	-0.50000	-0.40000	-0.30000	-0.20000	-0.10000
-0.03300	-0.01100	0.00000	0.02564	0.07692	0.17949	0.28205	0.38462	0.48718	0.58974
0.69231	0.79487	0.89744	0.94872	1.00000	1.01100	1.03300	1.10000	1.20000	1.30000
1.40000	1.50000	1.60000	1.70000	1.80000	1.90000	2.00000			
B 15									
-3.50000	-2.62500	-1.73000	-0.87500	-0.29200	-0.14600	0.00000	0.50000	1.00000	1.14600
1.29200	1.87500	2.73000	3.62500	4.50000					
C 2									
0.00000	1.00000								

B-indices

In the j-direction, the blade suction side corresponds to B=0., and the pressure side to B=1.. The blade-to-blade spacing near the walls was chosen to have points sufficiently close to the blade surface to resolve the low static pressures corresponding to the expected cavitation inception (see section B.2.2). The values B=-0.146 and B=1.146 were added in a second series of calculations to resolve these low static pressures on the suction side. The lines B=-0.073 and B=1.073 were also added to match the tip gap spacing for the future 3-D calculation and to satisfy the criterion of approximate equal distances around the blade corners.

A-indices

In the *i*-direction, the blade leading edge corresponds to $A = 0.$, and the trailing edge to $A = 1.$. The flow field boundaries were chosen approximately one chord length upstream of the leading edge and one chord length downstream of the trailing edge, at $A = -1.$ and $A = 2.$ respectively. The *A*-values upstream and downstream the blade represent physical relative lengths (for example, a value of $A = -0.2$ corresponds to a location 20% of the chord length upstream of the leading edge). On the blade, the *A*-values do not have a physical meaning any more; they are only initially chosen to match with the 40 data points given by SEP, going from 0. to 1. by increments of 1/39; at the end, only few of them were kept, keeping more lines near the blade ends and relaxing the core region where less rapid flow changes are expected.

Similarly to the approach followed for the *B*-indices, the grid spacing near the walls (leading edge and trailing edge) was chosen to contract by a factor 3 (see the sequence -0.1, -0.033, -0.011, 0. at the leading edge, and symmetrically at the trailing edge).

Finally, we checked that the normal spacing defined by the *A*- and *B*-indices was giving approximate equal distances around the grid corners (within a factor 2).

B.2.2 Simplified air-LH₂ analogy for cavitation inception.

In liquid hydrogen, we define a cavitation parameter (from reference 3):

$$K = \frac{P_{total\ relative\ upstream} - P_{sat}}{\frac{1}{2} \rho W^2}$$

Using the definition of the rotary stagnation pressure, and for an axial inlet flow:

$$P^* = p_{static} + \frac{1}{2} \rho W^2 - \frac{1}{2} \rho r^2 \omega^2 = p_{static} + \frac{1}{2} \rho V^2$$

$$K = \frac{(p_s + \frac{1}{2} \rho W^2) - p_{sat}}{\frac{1}{2} \rho W^2}$$

$$K = \frac{(P^* + \frac{1}{2} \rho r^2 \omega^2) - p_{sat}}{\frac{1}{2} \rho W^2}$$

Upstream, we can consider that $P^* = P_0$ is uniform. Thus, at $T_0 = 21$ K, $P_0 = 300,000$ Pa, $p_{sat} = 115,000$ Pa, and the velocity triangles communicated by SEP (reference 40), we find:

$$K = 1.04$$

A critical static pressure coefficient for analogous "cavitation inception location" in air is defined as:

$$\psi_{s0} = \frac{p_{sc} - P_0}{\frac{1}{2} \rho V^2}$$

where p_{sc} is the value of p , in air which corresponds to p_{sat} in LH_2 .

By analogy, in the air medium, we have:

$$K = \frac{(P_0 + \frac{1}{2} \rho r^2 \omega^2) - p_{sc}}{\frac{1}{2} \rho W^2}$$

$$K = \frac{P_0 - p_{sc}}{\frac{1}{2} \rho W^2} + \frac{\frac{1}{2} \rho r^2 \omega^2}{\frac{1}{2} \rho W^2}$$

$$K = \frac{P_0 - p_{sc}}{\frac{1}{2} \rho U^2} \frac{U^2}{W^2} + \frac{U^2}{W^2}$$

$$K = (1 - \psi_{s0}) \left(\frac{U^2}{W^2} \right)$$

Finally, for $K = 1.04$, we find:

$$\psi_{s0} = -0.048$$

Conclusion

A non-dimensional cavitation parameter for LH₂ has been used to obtain a corresponding static pressure coefficient for an air test. It has been found that a value of the static pressure coefficient in air $\psi_{s0} = -0.048$ corresponds to $p_t = p_{sat}$ in a liquid hydrogen pump. This extremely simplified criterion for cavitation inception is used here to gain a quantitative understanding of the minimum static pressure levels in the air flow calculation.

B.2.3 Inlet and other specific boundary conditions.

For the air test conditions specified by SEP and corresponding to the inlet velocity triangle sketched below (no inlet swirl: $\alpha = 0$; flow incidence angle of 3 degree relative to the blade: $\beta_{flow(at tip)} = 85^\circ$), we find:

$$V_{axial} = Q_{air}/(\rho \cdot \text{Passage Area}) = 8.09 \text{ m/s} = U,$$

with Passage Area = $\pi (r_{tip}^2 - r_{hub}^2)$.

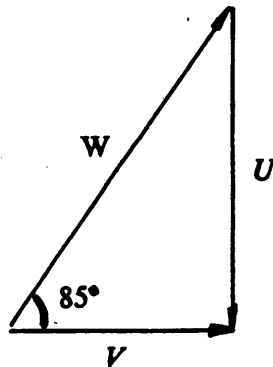
Thus, we have:

$$W = V_{axial}/\cos 85 = 91.64 \text{ m/s}$$

$$U = (W^2 - V^2)^{1/2} = 92.52 \text{ m/s} = -U,$$

$$P_{(static relative at inlet)} = P_{s, rel} - P_0 = -\frac{1}{2} \rho W^2 = -5282.71 \text{ Pa}$$

The other flow properties are taken uniform at inlet.



B.3 The meridional calculation.

B.3.1 Grid spacing and exit pressure condition.

Two series of meridional flow calculations were performed before choosing a final optimized grid pattern for the 3-D calculation. The first one was conducted over a grid size:

$$I \times J \times K = 42 \times 2 \times 19$$

The inlet plane was arbitrarily chosen about two spinner diameters upstream the spinner, whereas the exit plane was placed approximately one passage height downstream the blade trailing edge. The static pressure distribution calculated in this case is represented in Figure 32a.

In order to obtain a uniform static pressure distribution at the downstream end of the calculated flow-field, it was decided to add an arbitrarily long (about two passage heights) straight pipe downstream the previous grid. The grid size for this new configuration was:

$$I \times J \times K = 47 \times 2 \times 19$$

Figure 32b represents the static pressure distribution obtained, showing well the region in the middle of the downstream pipe where the flow has uniform properties. This plane of quasi-radial static pressure contour was chosen as the exit plane for the 3-D grid. The grid spacing for these calculations is reproduced below, and Figure 31 shows the resulting representations.

2D-MERIDIONAL GEOMETRY, CYLINDRICAL COORDINATES

GRID POINTS AT

A		47							
-2.20000	-2.10000	-2.00000	-1.90000	-1.80000	-1.70000	-1.60000	-1.50000	-1.40000	-1.30000
-1.20000	-1.10000	-1.00000	-0.90000	-0.80000	-0.75000	-0.70000	-0.65000	-0.60000	-0.50000
-0.40000	-0.30000	-0.20000	-0.15000	-0.10000	-0.05000	0.00000	0.10260	0.20510	0.30770
0.41030	0.51280	0.58970	0.69230	0.79490	0.89740	1.00000	1.10000	1.20000	1.30000
1.40000	1.50000	1.70000	1.90000	2.10000	2.30000	2.50000			
B		2							
-3.50000	4.50000								
C		19							
0.00000	0.00450	0.01215	0.03645	0.07290	0.10000	0.20000	0.30000	0.40000	0.50000
0.60000	0.70000	0.80000	0.90000	0.96000	1.00000	1.01000	1.01700	1.02000	

C-indices

In the k-direction, the grid spacing was defined to account for the boundary layer growth at the hub and shroud walls, as well as for the tip gap in the 3-D flow calculation. $C=0$. at the hub or on the rotation axis upstream the spinner, $C=1$. at the blade tip radius, and $C=1.02$ at the stationary shroud.

In the meridional calculation, only two points were taken in the tip gap region, at $C=1.01$ and $C=1.017$, to describe the boundary layer growth at the shroud. In the 3-D calculation, the value $C=1.005$ was added to account for the blade which is not present in this meridional simulation. At the rotating hub also, an adequate grid resolution was adopted, capable of reproducing any significant boundary layer phenomena (see the six points from $C=0$. to 0.1).

A-indices

Only few points were kept in the region corresponding to the blade location. A very coarse grid was sufficient between the two meridional boundaries, since the critical physical phenomenon was the boundary layer growth.

B.3.2 Inlet velocity profile.

For this meridional calculation series, we consider all inlet velocity components equal to 0, except the axial component V_z . Thus,

$$V_{radial} = 0$$

$$V_{\theta} = 0$$

We need to account for the boundary layer growth at the walls. The MEFP procedure can handle an approximate evaluation of the B.L. displacement thickness and refine it through an iterative procedure based on the continuity equation applied to the flow field.

Assuming a duct flow upstream of the inducer inlet plane, we can evaluate the Reynolds number:

$$Re_D = \frac{(\rho V D)}{\mu}$$

Here, we have:

$$\rho = 1.225 \text{ kg/m}^3$$

$$\mu (T = 288.15 \text{ K}) = 17.85 \text{ E-6 kg/m}^3 \cdot \text{s (from reference 36, p.465)}$$

$$D = 2 \text{ inlet radii}$$

$$V = \frac{Q}{(\rho Area)} = \frac{(4Q)}{(\rho \pi D^2)}$$

Thus,

$$Re_D = 85,000$$

This high value shows that we are in a turbulent flow regime (from Moses, in reference 36, p.4-4, transition in duct flows occurs at Reynolds numbers between 2000 and 4000).

Moreover, assuming that the pipe upstream of the inlet plane of the inducer is long enough, we consider also a fully developed flow regime.

From Schlichting (reference 37, pp.504 to 507), for a turbulent, fully developed duct flow, at a Reynolds number of 85,000, we find that a good approximation of the inlet velocity profile is given by the classical 1/7th power law:

$$\left(\frac{u}{U_{\max}} \right) = \left(\frac{y}{R} \right)^{(1/7)}$$

We can find the value of U_{\max} either by an integral method using the power law, or directly from Schlichting:

$$\left(\frac{u_{\text{mean}}}{U_{\max}} \right) = 0.817$$

and,

$$Q = \rho u_{\text{mean}} Area$$

This last equation gives u_{mean} , and then we can calculate U_{\max} . Finally, for each radial location of the inlet grid points we can calculate a value for the axial component of the velocity. The velocities are finally checked in the code for consistency with the specified mass flow rate (from the continuity equation).

B.4 3-D calculation grid.

The final MASTER GEOMETRY GRID used in the 3-D flow calculation was derived from the previous preliminary calculations. The size retained is:

$$I \times J \times K = 38 \times 17 \times 19$$

and the corresponding grid spacing is given below (see also Figures 35 and 36).

INDUCER 3-D GEOMETRY, CYLINDRICAL COORDINATES

GRID POINTS AT

A		38							
-0.60000	-0.50000	-0.40000	-0.30000	-0.20000	-0.15000	-0.10000	-0.06600	-0.03300	-0.01100
-0.00550	0.00000	0.00700	0.02564	0.07692	0.17949	0.29205	0.38462	0.48718	0.58974
0.69231	0.79487	0.89744	0.94872	1.00000	1.00550	1.01100	1.03300	1.10000	1.20000
1.30000	1.40000	1.50000	1.60000	1.70000	1.80000	1.90000	2.00000		
B		17							
-3.50000	-2.62500	-1.73000	-0.87500	-0.29200	-0.14600	-0.07300	0.00000	0.50000	1.00000
1.07300	1.14600	1.29200	1.87500	2.73000	3.62500	4.50000			
C		19							
0.00000	0.00450	0.01215	0.03645	0.10000	0.20000	0.30000	0.40000	0.50000	0.60000
0.70000	0.80000	0.90000	0.96000	1.00000	1.00500	1.01000	1.01700	1.02000	

A-indices

From the meridional flow solution shown in Figure 32, it appears that the plane $A = -0.6$ experiences a fairly uniform static pressure distribution. This plane was chosen as inlet plane for the 3-D grid. Similarly, the exit plane was chosen at $A = 2$.

An extra point was added upstream of the leading edge at $A = -0.0055$ (and symmetrically downstream of the trailing edge at $A = 1.0055$) to keep approximately equal spacing for the corner grid control volumes and match with the value $C = 1.005$ added in the tip gap. Two points were finally added, one at $A = -0.15$, to have a more uniform grid, and one at $A = 0.007$, for better resolution of possible cavitation inception.

B-indices

Two points were added to the blade-to-blade grid pattern, at $B = -0.073$ and $B = 1.073$, corresponding to the line $C = 1.005$ added in the tip gap.

C-indices

Compared to the meridional calculation grid, the value $C = 0.0729$ was removed to

obtain a smoother grid. The line $C = 1.005$ was added to solve for the flow near the blade tip.

Appendix C. Secondary Velocity Analysis.

C.1 Definition of the grid for the iso- θ sections.

The general representation of the inducer blade row studied is shown in Figure 2. By axisymmetry in a cylindrical coordinate system, an angular variation of $2\pi/4 = \pi/2$ gives a description of the complete inducer flow field, the other angular positions being deduced from the first quarter by rotation and repeating boundary arguments.

In a blade-to-blade representation, considering an angular domain of study between 0 and $\pi/2$ radians, we can draw the portions of the four blade passages as sketched in Figure 74 (actual angles in the tip section). In order to define the complete grid around the four blades, we must copy the Master Geometry Grid around the three other blades. This is simply realized by addition of $\pi/2$, π , and $3\pi/2$ to the angular definition of each grid point of the Master Geometry Grid.

The $\pi/2$ angular domain studied is shown in the blade-to-blade view, 0 and $\pi/2$ being repeating boundaries. A new (i' , j') grid is created over this domain for better display of the calculation results. The radial k -indexation is not changed. The new j' -indexation goes in the axial direction, from blade to blade. For each iso- θ plane (i' index), we consider each j -index of the Master Geometry Grid (from 1 to 17). Then, we scan through the i -indices, starting with $i=1$, and look for the two values $\theta_A(i,j,k)$ and $\theta_B(i+1,j,k)$ which surround the current iso- θ value. A linear interpolation between the grid points A and B is then used to obtain the flow properties and grid point type (stationary wall, rotating wall, or flow point) at the new point $C(i', j', k)$, see Figure 74. This process is performed four times, giving finally $4 \times 17 = 68$ points in the j' -direction.

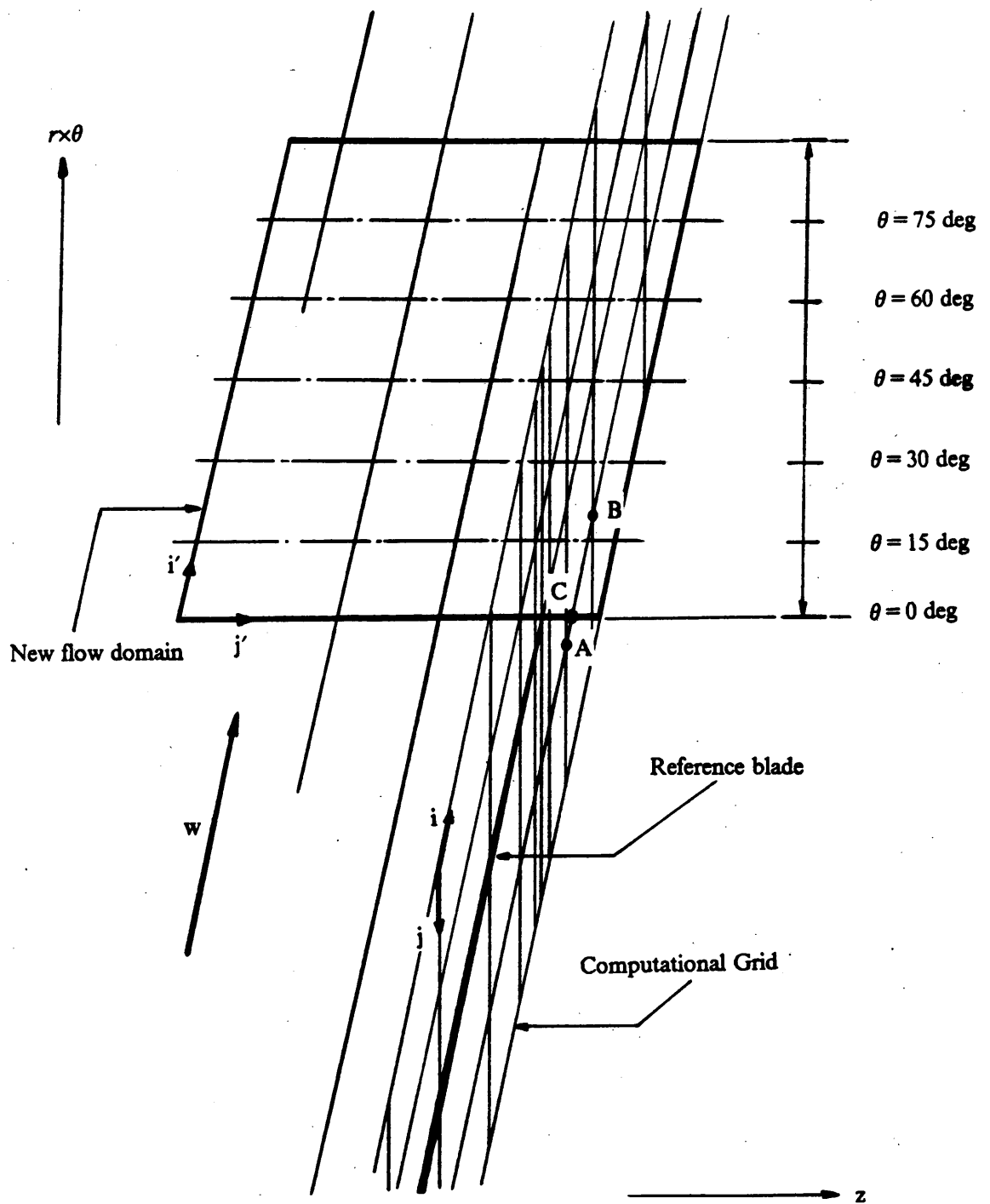


Figure 74. Definition of iso- θ planes: new grid definition, for four blades, from $\theta = 0$ to $\pi/2$.

C.2 Definition of the Secondary Velocities.

In cylindrical coordinates, the relative velocity vector can be written as:

$$\mathbf{W} = W_r \cdot \mathbf{u}_r + W_\theta \cdot \mathbf{u}_\theta + W_z \cdot \mathbf{u}_z \quad (\text{C.1})$$

At each grid point of the Master Geometry Grid, the unit vector \mathbf{i} in the streamwise primary direction (i-line) is calculated by:

$$RNORME = \sqrt{((r(i+1) - r(i))^2 + (r(i) \cdot (\theta(i+1) - \theta(i)))^2 + (z(i+1) - z(i))^2)}$$

$$\mathbf{i} = \frac{(r(i+1) - r(i))}{RNORME} \cdot \mathbf{u}_r + \frac{r(i) \cdot (\theta(i+1) - \theta(i))}{RNORME} \cdot \mathbf{u}_\theta + \frac{(z(i+1) - z(i))}{RNORME} \cdot \mathbf{u}_z$$

We will use the simplified notation:

$$\mathbf{i} = i_r \cdot \mathbf{u}_r + i_\theta \cdot \mathbf{u}_\theta + i_z \cdot \mathbf{u}_z$$

In order to separate the primary streamwise component of \mathbf{W} and its secondary residual, we can write in the cross-sectional planes:

$$\mathbf{W} = W_i \cdot \mathbf{i} + W_{r \text{ sec}} \cdot \mathbf{u}_r + W_{z \text{ sec}} \cdot \mathbf{u}_z \quad (\text{C.2})$$

We have also:

$$\mathbf{W} = (W_i \cdot i_r + W_{r \text{ sec}}) \cdot \mathbf{u}_r + (W_i \cdot i_\theta) \cdot \mathbf{u}_\theta + (W_i \cdot i_z + W_{z \text{ sec}}) \cdot \mathbf{u}_z$$

A comparison between equations (C.1) and (C.2) gives then:

$$W_i \cdot i_\theta = W_\theta$$

or,

$$W_i = \frac{W_\theta}{i_\theta}$$

At each grid point, W_θ is a flow calculation output value and i_θ is calculated from:

$$i_\theta = \frac{r(i) \cdot (\theta(i+1) - \theta(i))}{RNORME}$$

Thus W_i is known, and we can evaluate:

$$W_{r \text{ sec}} = W_r - W_i \cdot i_r$$

$$W_{z \text{ sec}} = W_z - W_i \cdot i_z$$

**The vita has been removed from
the scanned document**